Long, Q. (1999). The study of blood flow in human arterial bifurcations by the combination of CFD and MRI. (Unpublished Doctoral thesis, City University London)

CITY UNIVERSITY LONDON

EST 1894

Original citation: Long, Q. (1999). The study of blood flow in human arterial bifurcations by the combination of CFD and MRI. (Unpublished Doctoral thesis, City University London)

Permanent City Research Online URL: http://openaccess.city.ac.uk/7712/

THE STUDY OF BLOOD FLOW IN HUMAN ARTERIAL BIFURCATIONS BY THE COMBINATION OF CFD AND MRI

by

QUAN LONG

A dissertation submitted to

The City University

in fulfilment of the requirement

for the degree of

Doctor of Philosophy

MARCH 1999

Department of Mechanical Engineering & Aeronautics

The City University

London

Abstract

Atherosclerosis represents a major health problem in the western world. The local haemodynamics is believed to be an initiating and localizing factor in this multifactorial disease process. To fully understand this interaction it is important to obtain detailed information about the local haemodynamics in accurate models of the human vascular system. Because of the complexity of arterial geometry, *in vivo* velocity measurements are subject to large errors by currently available techniques. It is also difficult to construct the highly irregular arterial bifurcation model for *in vitro* investigations. By using a combination of two new methodologies, namely magnetic resonance angiography (MRA) and computational fluid dynamics CFD), the precise patterns of flow anticipating the onset of disease at arterial bifurcations can now, in principle, be determined. However, flow simulations based on *in vivo* data directly acquired from clinical measurements have rarely been performed, due to difficulties involved in converting medical images into a data set that CFD software packages can accept.

In this study, a computer modelling technique, which integrates clinically acquired MR angiograms, image processing and CFD, for the reconstruction of 3D blood flow patterns in realistic arterial geometry, was developed. In the procedure, human arteries are scanned non-invasively by MR angiography. With the MR angiograms, image processing and 3D reconstruction are performed and structured numerical grid is generated for the arteries scanned. Together with MR *in vivo* measured velocity profiles at the boundary planes of the model, CFD simulations are undertaken. To test the capability and reliability of the whole procedure, two examples are given, of the human abdominal and right carotid bifurcations. The complete haemodynamic patterns obtained allow a full clinical understanding to be gained of individual patient behaviour. Aspects such as wall shear stress variation, secondary flow and flow separations are demonstrated. The problem of quantitative reliability of the predictions is discussed in some depth.

ACKNOWLEDGEMENTS

It is a pleasure to recall my two and half years of tutelage under Professor M.W. Collins at City University. His enthusiasm and zest for research have been infectious, and his encouragement in various matters technical or otherwise is greatly appreciated. I also wish to thank my current supervisor Dr. R. Neve for his kindly help in the final stage of the PhD. course.

My special thanks are due to Dr. X.Y. Xu for all her help especially during the final year of the project.

I wish to thank Professor C.G Caro in Imperial College, who initiated me into the MRI research during my one year visiting him before I started this PhD project.

I have also received help from my clinical collaborator: Drs. S. Thom, A. Hughes, A. Stanton and B. Ariff in St. Mary's hospital, London, Professor T. Griffth and Dr. M. Bourne in University of Wales, College of Medicine, Cardiff, in understanding physiological problems in the project and acquiring MRI data.

Mention must be made of my fellow research students (some of whom have now finished their doctoral studies) Hamid Eslimy-Isfahany, Osvaldo Comineli, and Andrew Cowley. Without them, the student life would not be so colourful and enjoyable.

Finally, I would like to express my special thanks to my wife for her patience and various support, and my parents for their understanding and persistent support throughout the years of my study.

Contents

List of Figures

Chapter 1

Introduction

Atherosclerosis, a disease of large- and medium-size arteries, is the chief cause of death in most of the western world. Severe atherosclerosis interferes with blood flow; this is particularly important for the heart and brain, with the result being myocardial or cerebral ischemia or even a myocardial infarction or stroke. Years of research on the mechanisms of atherosclerosis have made a great improvement in our understanding of the development of the disease. However, because of the complex nature of the problem, many details remain unknown and existing hypotheses need to be proved.

1.1 Atherosclerosis and Related Haemodynamic Factors

Atherogenesis, i.e. the initiation of atherosclerosis, starts virtually at birth, and the total disease process is characterized by a time constant on the order of decades. There have been many excellent reviews of what we know about this disease and its evolution [1]. There is no longer any doubt that atherosclerosis begins with focal accumulations of plasma lipids, mainly cholesterol, in the form of plasma low density lipoprotein (LDL) in the intima of arteries, which differ in their susceptibility to this process. Elucidation of the atherogenic effect of LDL and of its control by a specific cellular receptor, for which the Nobel Prize was awarded to J.L. Goldstein and M.S. Brown, was a major advance in understanding the mechanisms at

work in the disease. Because of the fact that arterial vessels are in permanent contact with the flowing blood, haemodynamic factors associated with the on-set of atherosclerosis have been widely studied.

Interestingly, the potential for fluid dynamics to influence the understanding of atherogenesis was realized relatively early. Virtually every fluid dynamics factor imaginable has been considered: turbulence, high wall shear stress, low wall shear stress, oscillating wall shear stress, high pressure and low pressure were each proposed as atherogenic. After years of research and the improvement of understanding, most tend to support the role of wall shear stress in the formation of atherosclerosis.

Whether atheroma is favoured by low or high wall shear stress has, however, been controversial. If the high shear stress hypothesis [2] is correct, it should be the apex of bifurcations, the proximal inner aspects of the branches and outer walls beyond regions of boundary layer separation that are maximally affected. However, there is now evidence to suggest that in humans atheroma occurs predominantly where wall shear stress has been predicted to be low and or where flow has been disturbed at regions of separation and reattachment such as the outer wall of bifurcations. Histologically, intimal thickening does not arise abruptly, but is nevertheless maximal at points of flow separation where these exist [3]. In the left anterior descending coronary artery, for example, there is skewing of the forward flow velocity profile away from the wall where the greatest atherosclerotic change occurs suggesting that, in this case, low fluid velocity or low wall shear stress is an important contributory factor.

Although evidence shows that development of early atherosclerotic lesion is associated with locations where the mean wall shear is relatively low, the role of wall shear oscillations in both direction and magnitude is not established. A shear stress-related mechanism implies that mechanical forces acting on the artery wall are involved, while a shear rate-related mechanism [4] implies that mass transport between the blood and wall is a key factor.

Friedman et al [5, 6] in a series of studies have also examined wall shear in cases of individual coronary arteries and aortic bifurcations, and they have correlated various measured parameters with intimal thickness in the arteries from which the casts were developed. It was found that high shear locations were involved in the earliest intimal thickness observed, but low wall shear was associated with later or more advanced intimal thickening. All vessels examined had only slight intimal thickening.

There is evidence to support the concept that both shear stress and mass transport are involved. The tendency for intimal thickening to occur in low shear regions is likely stress-induced through an endothelial cell response. However, intimal thickening is not necessarily atherosclerosis, the latter having in addition the incorporation of low-density lipoproteins and other substances. This undoubtedly is a mass transport phenomenon. An explanation of this phenomenon is that there is shear-dependent transport of lipid and lipid metabolites both into and out of the walls of arteries. Lesions develop more rapidly where shear is high and there is transient hypercholesterolemia, whereas cholesterol will eventually accumulate preferentially where shear is low once an equilibrium state is attained. Indeed, there is experimental evidence to suggest that this is the case [7].

The research in the effect of shear stress on the endothelium has given some insight into the mechanism by which local haemodynamics could influence the development of atheroma in the adjacent arterial wall. At sites where the velocity field and thus shear stress is disorganised and fluctuating, it has been shown experimentally that endothelial cell mitosis rates are elevated, which is suggestive of cell injury [8]. Shear is also known to affect endothelial morphology [9], permeability [10], to influence the orientation of endothelial stress fibres [11], and to enhance pinocytosis [12] and the receptor-mediated component of low-density lipoprotein(LDL) binding, internalisation and degradation [13]. Shear stress could thus influence the transport of lipids and other molecules into the arterial wall. Shear stress also modulates synthesis of endogenous vasoactive substances by the endothelium such as EDRF (nitric oxide) and prostaglandins, particularly when flow is pulsatile. EDRF dilates arteries, and vasodi-

latation enhances wall porosity, which would favour mass transport of water and molecules through the arterial wall [14].

Most of the hypotheses discussed above are based on the relationship of the biological discoveries of arterial disease and haemodynamical parameters, especially the wall shear stress distribution in arteries. Therefore the investigations of blood flow patterns in various models under different dynamic conditions form a main part of the research. Knowledge of flow patterns in human arteries is prerequisite to establishing a correct relationship between haemodynamic factors and arterial diseases. However, because of the complexities of the geometry of arteries, most of the haemodynamic studies are based upon simplified geometry to some extent. The aim of this study was to develop a computational procedure that is able to simulate blood flow in anatomically realistic arterial model and 'real' flow conditions.

1.2   Haemodynamic Research

To have a clearer understanding of haemodynamic factors in the formation of atherosclerosis, studies have been going on for more than several decades with an aim to quantify the flow parameters in specific arterial regions where the diseases occur most frequently. These studies involve physicists, engineers, physiologists and physicians.

1.2.1   General description of blood flow in large arteries

Two dimensionless parameters have been consistently used to characterize the blood flow in large arteries, they are defined as follows:

$$\text{Reynolds number} = \frac{\text{inertial force}}{\text{viscous force}} = \frac{\rho DU}{\mu} \tag{1.1}$$

$$\text{Womersley number} = \sqrt{\frac{\text{transient inertial force}}{\text{viscous force}}} = \frac{D}{2}\sqrt{\frac{\rho\omega}{\mu}} \tag{1.2}$$

D being the parent vessel diameter, U the time-averaged velocity in the parent vessel, ρ the fluid density, μ the dynamic viscosity, and ω the angular frequency of the oscillating flow. In steady tube flow, U refers to the average cross-sectional velocity. In certain applications, particularly in oscillating flows, the peak Reynolds number, defined as the Reynolds number at peak velocity, is often used. Transition from laminar to turbulent flow during steady flow in a tube typically occurs at a Reynolds number of about 2300. This is defined as the critical Reynolds number.

Clearly, the cardiovascular system differs in several ways from the conditions described above for the application of the Reynolds number to steady flow in straight tubes. In the cardiovascular system, flow is pulsatile (as described by Womersley number), blood is non-Newtonian and vessels are compliant. The vessels taper, curve and branch. Frequently there are intimal irregularities as with atherosclerosis. It is unrealistic, therefore, to expect the critical Reynolds number at which turbulence would occur in the cardiovascular system to be the same as the critical Reynolds number for steady flow in a smooth, straight tube. A number of studies have been done to investigate the blood flow disturbances [15, 16, 17]. However, the evaluation of turbulence or blood flow disturbances in the cardiovascular system is complex. The auther does not intend to involve this complexity in this study, blood flows are normally considered as laminar and pulsatile flow in the following CFD calculations.

Blood is a suspension of a variety of cells in an aqueous solution called plasma. In large blood vessels, it is reasonable to consider blood as a homogeneous incompressible fluid. Studies [18] show that differences between Newtonian and non-Newtonian flows occur mainly in regions of flow separation. With the non-Newtonian fluid, the duration of flow separation is shorter and the reverse flow is weaker. Nevertheless, it does not have significant effects on the basic features of the flow field.

When considering the geometrical complexity, it is found that the Dean number, which expresses the non-dimensional ratio of inertial and centrifugal forces to the viscous forces is a fundamental parameter. In theoretical studies, this is commonly given as

$$\text{Dean number} = (\frac{Ga^2}{\mu})(\frac{2a^3}{Rv^2})^{\frac{1}{2}} \tag{1.3}$$

Where a is the tube radius, R the radius of curvature for the tube bending, G the pressure gradient and μ, v the dynamic and kinematic viscosities, respectively. A more useful form for comparison with measurements (which eliminates G), given by Berger et al [19] is $D_2 = (\frac{a}{R})^{\frac{1}{2}} Re_D$, where Re_D is the Reynolds number based on mean velocity and tube diameter.

To describe a 'real' haemodynamic problem, normally, the three dimensionless parameters should be used together. Reynolds number gives the dynamic range of the flow, Womersley number is used to describe the flow variation with time while Dean number describes the geometry of the problem. These parameters may determine the qualitative behaviour of the flow. To obtain a clearer picture of the flow patterns in large arteries, more detailed descriptions of flow features are needed. Several main features of blood flow in large arteries especially in bifurcations can be summarised as:

Oscillatory flow

As a main power source in the vascular system, the heart pumps blood to arteries and creates a pulsatile motion of blood. In the arterial system, this pulsatile behaviour varies from artery to artery. For example, in the carotid artery, cross-sectional average mass flow is generally in one direction (towards the head) during a cardiac cycle while in the abdominal aorta the average flow may go backward (towards the heart) for a short period of the cardiac cycle. These variations in flow waveform will influence flow behaviour significantly which will be demonstrated in chapters 6 and 7. In numerical modelling studies, these waveforms are used

as flow boundary conditions.

Flow separation

In laminar flows, generally, there is a laminar boundary layer attached to the vessel wall. However, when a fluid flows over curved surfaces such as bends and bifurcations, under certain circumstances, the fluid is no longer able to follow the contour of the surface and breaks away from it. This breakaway is usually termed flow separation. It is caused by the reduction of velocity in the boundary layer, combined with a positive pressure gradient. Reverse flow forms after the separation point to fill the gap between the separated boundary layer and the surface contour. The line of zero velocity dividing the forward and reverse flow leaves the surface at the separation point, and is known as the separation streamline. As a result of the reverse flow, large irregular eddies are formed. The region formed by the separation streamline and the surface is called the separation zone. Flow separation is a main flow feature at arterial bifurcations especially at the carotid bifurcation because of the internal carotid bulb. Quantitative knowledge of the size and variation of the separation zone, fluid particle behaviour inside the zone such as particle residence time will certainly improve the understanding of arterial disease formation in the region. Because flow separation is highly dependent on the local geometry of the vessel, accurate representation of the arterial geometry is an essential to obtain a valid prediction. This forms a main part of this study.

Secondary flow

Another main flow feature in large arteries especially in the vicinity of bifurcation is the presence of secondary flow. In a straight tube with uniform cross-sectional area, fluid flow only has inertial and viscous forces which force the flow in one direction. However, if the vessel has curvature, secondary flows will be set up that cause a streamline of dye to follow a helical course. This can be most simply explained in terms of the centrifugal effects associated with motion in a curve. This effect is greatest in the central streams because they are moving fastest, and least in the fluid near the wall which is moving slowly. Therefore, the fluid in the middle of the stream creates a secondary flow towards the outer wall of the

20

curve; this forces the fluid nearer the wall to flow towards the inner wall. The secondary flow patterns are dependent on the Dean number and vessel geometry. For planar bending of circular vessel, a pair of counter-rotating vortices can be found which is also known as a Dean type vortex. However, if two or more bends occur closely and lie in different planes, complex secondary flow patterns are expected. An extreme case is one single vortex dominating the plane. Secondary flow increases the mixing of the fluid particles, and promotes the washout of particles inside the flow separation zone. In some cases, such as vascular graft design, this washing out force is significant.

1.2.2 Methodology description of haemodynamic research

From the methodology point of view, haemodynamic studies can be divided into three categories:

- In vitro (experimental) measurement.

- In vivo measurement.

- Computational simulation.

In vitro measurement methods such as Laser Doppler Anemometry (LDA) velocity measurement, has been used to study fluid dynamics in arterial models from the 1970's. Because it can offer quantitative velocities for complex time-dependent flows, the method has made a great contribution to the understanding of arterial flow behaviour and is still widely used in *in vitro* model studies. Apart from the Doppler methods which give point-to-point velocity measurement, flow visualization methods also play a very important role to determine the flow field qualitatively and quantitatively. However, they generally require transparent models which obviously cannot be used in *in vivo* measurement. Two major difficulties associated with *in vitro* measurements are: (a) obtaining anatomically realistic arterial models and (b) generating a suitable flow waveform representing the 'real' pulsatile flow.

The technical developments in Magnetic Resonance Imaging (MRI) and/or Doppler Ultrasound have made non-invasive *in vivo* velocity measurement possible. The *in vivo* measured flow parameters provide data for the individual subject or patient because the measurement is undertaken in a "real life" flow environment. As velocity measurement based methods, MRI and USD are also widely used in *in vitro* haemodynamic research. However, large measurement errors in flow disturbed regions are limiting the application of the methods. A more detailed discussion of MR measurement errors can be found in chapter 2.

Computational Fluid Dynamics (CFD), on the other hand, has gone through its development from the 1980's of 2D steady flow simulation to recently 3D complex transient flow. Most commercially available CFD codes are able to solve full Navier-Stokes equations and offer quantitative flow parameters including wall shear stress (WSS) for 3D complex geometry. Code validations have been made in different models from very low Reynolds number to turbulent flow. However, because of the difficulty in obtaining geometrically realistic arterial models, most of the *in vitro* experiments and numerical studies were based on simplified models to some extent.

As described above, because of the complex arterial geometry, flow patterns in real arteries are significantly different from those obtained in simplified models. Anatomically realistical arterial models can be constructed by making casts from autopsy. However, many complicated techniques were involved in making these casts and they can only be obtained from autopsy, limiting its application to individuals. On the other hand, flow conditions (ie. velocity and or pressure conditions) measured from other subjects were frequently used in these *in vitro* measurements which may not reflect the real dynamic conditions in the artery of interest.

Alternatively, an anatomically realistical arterial model can be constructed by combining modern non-invasive angiography techniques such as MRA with digital image processing. Together with measured *in vivo* time-dependent velocity profiles at model boundary planes, the state-of-the-art CFD techniques can be applied to produce 3D blood flow patterns and

other haemodynamic parameters related to the development of arterial diseases.

1.3   Objectives and Strategy Employed in the Research

With the rapid development in non-invasive human angiography techniques, 3D angiograms can be acquired from conventional practice. Clinicians wish to have more knowledge not only about arterial geometry but also on the blood flow inside the vessel. Scientists, on the other hand, are not satisfied with flow parameters obtained from simplified models. This research was aimed to combine the magnetic resonance angiography and the modern computational fluid dynamics techniques to obtain predictions of blood flow parameters in anatomically realistic arterial bifurcations under the specific flow condition corresponding to individuals. The main purposes of the research may then be stated as follows:

- Development of computational methods required to simulate the blood flow in *in vivo* measured anatomically realistic arterial bifurcations.

- Validation of the CFD predictions with *in vivo* velocity profiles acquired with MRI.

- Obtaining time-dependent flow parameters in bifurcation models quantitatively to help the understanding of the onset of atherosclerosis.

- Improving the robustness and efficiencies of the software package developed so that it could be considered for use in clinical practice in the near future.

Figure 1.1 is the flow chart of the complete modelling system. It comprises four parts, these are (a) geometry model generation, (b) dynamic boundary condition generation, (c) numerical simulation, and (d) flow visualization and CFD result analysis.

To achieve the final goal the research procedure involved the following steps:

```
                  ┌─────────┐              ┌──────────────────────┐
                  │   MRA   │              │ Velocity imaging by MRA │
                  └─────────┘              └──────────────────────┘
                       │                              │
                       ▼                              ▼
   ┌─┐      ┌──────────────────┐        ┌─┐
   │A│      │   3D Human Arterial │        │B│
   └─┘      │   bifurcation Model │        └─┘
            └──────────────────┘        ┌──────────────────────┐
                       │                │  Interpolation to Required │
                       ▼                │  Boundary Mesh Points and │
            ┌──────────────────┐        │       Time Steps          │
            │ Computational Mesh │        └──────────────────────┘
            └──────────────────┘
                       │                        │
                       ▼                        ▼
                  ┌──────────────────┐        ┌─┐
                  │ Numerical Simulation │        │C│
                  └──────────────────┘        └─┘
                           │
                           ▼
                  ┌──────────────────┐        ┌─┐
                  │ CFD Post-processing and │    │D│
                  │ Predictions Validation │    └─┘
                  └──────────────────┘
```
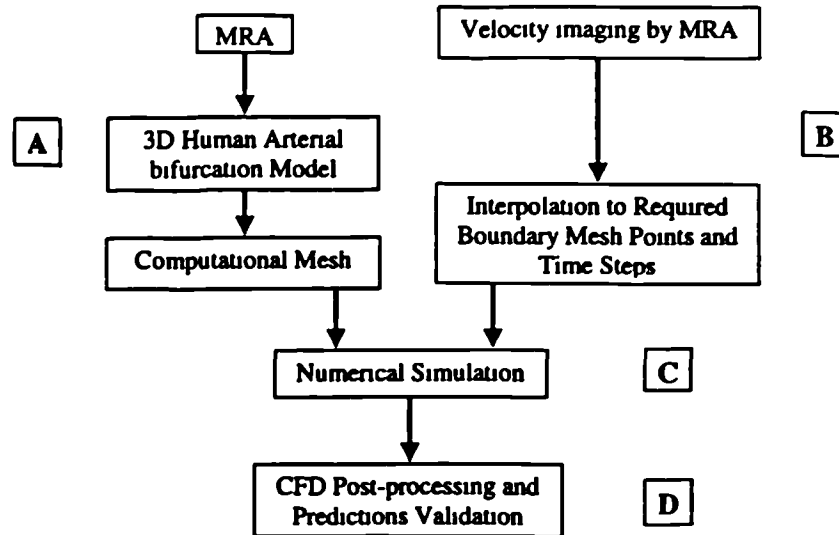
Figure 1.1: Flow chart of the procedure that CFD simulations are carried out by using the combination of anatomically realistic arterial models and MR measured velocities.

1. Optimize the conventional MR scan sequences to obtain high quality angiograms for the arterial bifurcations and velocity profiles at the bifurcation boundary planes.

2. Develop the MR image processing and 3D reconstruction algorithms to generate anatomically realistic arterial bifurcation models and time-dependent velocity boundary conditions.

3. Develop the interface between MR images and the CFD solver by generating structured numerical grids in the bifurcation model.

4. Perform the full 3D time-dependent fluid dynamics simulation and obtain complete fluid and wall shear stress data.

5. Visualize the CFD results with a state-of-the-art post-processor.

6. Assess the accuracy in various model generation processes and ensure a certain order of accuracy in the overall processing. Validate the CFD predictions against *in vivo* velocity data acquired by MRI.

The thesis is organized in a logical sequence. In Chapter 2, a comprehensive literature survey is given for the research which contains basic knowledge and the recent development in MRI, medical image processing and analysing, and some CFD techniques. In Chapter 3 and 4, algorithms of anatomically realistic model and velocity boundary condition generation for CFD simulation are described. In Chapter 5, a code description is given in which mathematical equations and numerical techniques employed in the simulation are discussed. Boundary conditions and possible code validation methods are also presented. Comprehensive CFD simulations and predictions for blood flow at a human abdominal-iliac bifurcation and a right carotid bifurcation are presented in Chapters 6 and 7 respectively. Finally, conclusions of the research are made in Chapter 8.

Chapter 2

Literature Survey

2.1 Introduction

Although it is now recognized that specific patterns of local blood flow predispose to the development of atheroma, the mechanisms underlying this important determinant of cardiovascular "risk" are incompletely understood. By using a combination of two new methodologies, namely magnetic resonance angiography and 3-dimensional computational modelling of the vessel wall and flow, the precise patterns of flow that predispose to disease at arterial bifurcations can now, in principle, be determined. Flow simulations based on *in vivo* data directly acquired from clinical measurements have rarely been performed, due to difficulties involved in "translating" medical images into a "language" that CFD codes can read. In practice, the procedures are composed of the following: (1) acquisition of high quality MR images (including angiograms which gives 3D geometry of the arteries, quantitative velocity images which will form dynamic boundary conditions for CFD calculation), (2) image processing and geometric reconstruction, and (3) grid generation, followed by flow simulation and visualization.

This chapter covers the principles and latest developments in all these three areas. While they are treated as individual topics, the relationships among them and practical methods to integrate the procedures are discussed and explored in detail.
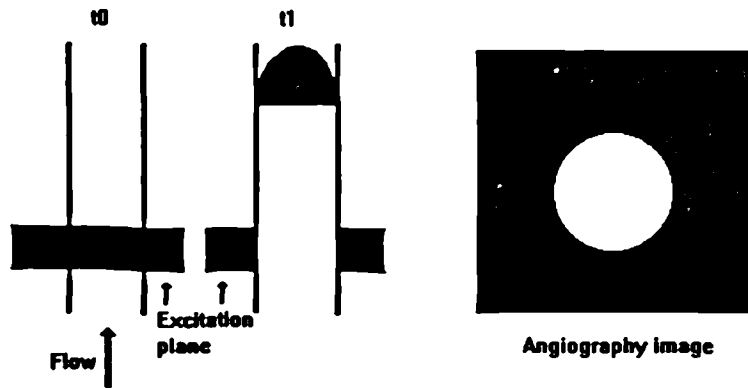
Figure 2.1: Schematic illustration of the Time-of-Flight method

2.2 Magnetic Resonance Angiography

For more than 30 years it has been known that magnetic resonance can be used *in vivo* to study blood flow. The flow of blood through magnetic field gradients and radio frequency fields produces signal changes that can be used to distinguish blood vessels from the surrounding stationary tissue. To measure these signal changes blood vessel images may be obtained. The application of MR angiography involves attempting to create high contrast images of flowing blood against a background of stationary material, but without the need for ionizing radiation or a contrast agent.

The MRA imaging techniques can be divided into two classes according to their scientific bases, namely, the Time-Of-Flight (TOF) and the Phase-Contrast (PC) methods.

2.2.1 Time-Of-Flight techniques

The TOF method refers to the motion of blood into and out of the plane of section as shown in Figure 2.1. Stationary tissues remain in the section and are repeatedly affected by the section-selective radio frequency (RF) pulse. If repetition time (TR) is short relative to the T1 of the tissues, then the longitudinal magnetization of those tissues is suppressed (satu-

rated) and they appear dark. This is because the stationary tissue does not have enough time to relax. On the other hand blood coming from outside the section is unaffected by the section-selective RF and is fully magnetized. As more unsaturated spins flow into the slice during each TR, overall signal strength rises, and is maximized when all the partially saturated flowing spins in the slice are replaced each TR. Thus, signal enhancement called 'flow-related enhancement' or 'paradoxical enhancement' is directly related to flow velocity and slice thickness.

In principle, TOF techniques are able to provide greater morphological details than phase sensitive methods. This is because TOF procedures can be designed to exploit only longitudinal magnetization and thus be insensitive to flow-related phase shifts in transverse magnetization. But in situations where complex flow patterns exist, flow disturbances may cause dephase which weakens the signal intensity. So in practice, serial gradient-echo pulse sequences are applied which compensate the dephase to obtain better image quality. Flow-compensation is routinely used in MR angiography. The first-order (velocity) compensation is commonly used but in some cases a higher order (either 'acceleration' or 'jerk') compensation is necessary.

Directional information can be derived from TOF MRA in a variety of ways, including selective presaturation [20] and bolus tracking [21]. Selective presaturation involves pre-exciting a slab to eliminate signals from specific vessels. Bolus tracking is a variant of this, involving the use of a thin in-plane saturation slab, followed by several gradient-echo acquisitions. Displacement of the intravascular component of the slab on serial images shows the direction of blood flow, and this can be displayed graphically in a cine loop.

To separate the signals from arterial and venous blood, additional saturated pulses (selective presaturation) are used which separate flows in different directions. The presaturation pulse, typically using a large flip angle (90°), is applied over a thick region (e.g. 30-100mm) [22] inferior to the imaged region (20mm away [23]) in the first acquisition and superior to the imaged region in the second acquisition. When the two data sets are analysed, blood flow

28

coming from the opposite direction will be highlighted with respect to the background and the two blood streams will be distinguished from each other.

Conventional TOF sequences can be classified into two groups: 2D and 3D TOF MRA. These are discussed in detail below.

2.2.1.1 2D Time-of-Flight MRA

Two-dimensional TOF MRA depicts vessel structures by acquiring the data as a stack of 2D images (thin slices). A single slice can be acquired in less than 7 sec. Modification of the acquisition loop structure enables acquisition of further slices to begin on completion of the first, such that the second slices are acquired in 14 sec, the third in 21 sec, and so on [24]). So by this technique, as many slices as desired may be scanned but the scan time will be proportionately longer. Typically a 2D slice is selected to be very thin to permit even slowly moving blood to penetrate the region of RF excitation. Thin slices are also useful to preserve image resolution if the stack of 2D images is to be analysed by projection. The optimum slice thickness is influenced by the size of the vessels of interest, and more importantly, by the estimated flow. The imaging time ranges from 7 minutes to 15 minutes.

The advantages of 2D TOF MRA may be summarised as follows:

- Sensitive to a wide range of velocities including slow flow, making it useful in both arteries and veins.

- Independent of the distance into the imaged volume.

- Short image acquisition time for large volumes.

- Less sensitive to subject movement.

The major disadvantages of 2D TOF MRA are:

- Significant signal loss in complex flows.

- Poorer Spatial resolution than its 3D counterpart.

2.2.1.2   3D Time-of-Flight MRA

In this procedure, 3D data are acquired from an imaging volume called a 'slab' rather than the thin (or thick) 'slice' used in 2D TOF methods. Having decided to use 3D scanning a 'partition number' is chosen to generate a series of thin slice images. However, the thickness of the slab is usually no more than 70mm, limiting the scan region to a small range. On the other hand, the small slice thickness (below 1mm) allows a very high spatial resolution to be achieved. A 3D TOF image normally has higher signal-to-noise ratio and a shorter scan time than the 2D techniques because only one slab needs to be scanned.

The advantages of 3D TOF MRA are:

- High spatial resolution, especially in the axial direction.

- Relatively short scan time. (less than 7 minutes)

- Very short echo time (TE) is possible.

- Less signal loss compared with 2D TOF and 3D PC.

- Good image quality even in fast flow regions.

- Higher signal-to-noise ratio than 2D methods.

Indicators of 3D TOF MRA use in protocols:

- Should be used to image structures where signal loss is a concern.

- Can be used to image aneurysms and stenosed vessels.

Major disadvantages of 3D TOF MRA are:

- Insensitive to slow flow, hence difficult to image veins without the aid of a contrast agent.

- Short T1 materials (stationary tissues) produce echoes.

- Sensitive to subject's movement.

- Effective only for small volumes. Signal intensities vary with distance into the imaged volume and with flow direction.

To overcome the disadvantages associated with 3D TOF, a third TOF technique, multiple overlapping thin-slab acquisition (MOTSA) time-of-flight was developed [25]. Blatter et al [26] used a series of overlapping 3D thin slabs (25-50mm) to span a large vascular region of interest. Overlapping slabs were required because the profiles of the 3D slabs were not perfectly rectangular. One drawback of this technique is that it is sensitive to the subject's motion. Kauczor et al [27] used a double slab technique (2 × 64 partitions with overlap) to prevent in-slab saturation in large aneurysms. Using the same techniques Edelman [22] obtained a very reliable set of results in studying the intracranial circulation and the extracranial carotid arteries.

However, the TOF approach has some limitations. Since the T1 and velocity of the flowing material restrict its detectable range, long vessels are difficult to visualize. Some tissues (most notably thrombi) have a short T1 and result in echo which may be indistinguishable from that of blood.

2.2.2 Phase-Contrast techniques

Phase-Contrast (PC) imaging refers to a family of MR imaging methods that exploit the fact that spins that move through magnetic field gradients obtain a different phase than static spins (moving related phase-shift), enabling the production of images with controlled sensitivity to flow.

Each MR raw data set produces an image that portrays the transverse magnetization in each voxel. This transverse magnetization is a vector which can be defined in both magnitude and direction (phase angle). Although it is the magnitude of the magnetization that contributes to the image intensity, the phase provides information about the motion. Quantitative analysis of the relationship between flow-related phase shift ϕ and the spins moving velocity v can be

expressed as [28]:

$$\phi(t) = \gamma \int x(t) \cdot G_X(t) dt \tag{2.1}$$

where $\phi(t)$ is the phase shift of the spin at time t, γ is the gyromagnetic ratio, x(t) is the location of the spin at time t and $G_X(t)$ is the strength of the magnetic field gradient as a function of time.

Normally, a gradient pulse (two equal pulses of opposite polarity) is used to encode proton velocity as a change of phase. The phase shift induced by the two pulse sequence is given by

$$\phi = \gamma \int_0^{T_G} x(t) \cdot G_X(t) dt + \gamma \int_T^{T+T_G} x(t) \cdot G_X(t) dt \tag{2.2}$$

where T_G is the duration of each pulse. Here $G_X(T+t) = -G_X(t)$, if $M1$ is the first moment of the gradient waveform $G_x(t)$ evaluated at the echo delay time (TE), and $M1 = \int_0^{T_G} G_X(t) dt$, yielding for a constant velocity

$$\phi = \gamma V_X T M 1 \tag{2.3}$$

Note that for spins with zero velocity (stationary material), there is no net change in phase, while moving spins can easily be detected. If the pulse sequence is repeated with inverted flow-encoding gradients, the signal intensity I obtained from complex subtraction of the two acquired data sets will be $I = 2k\sin\phi$, where k is a proportionality factor that includes spin populations and instrument sensitivity. The magnitude of this difference can be displayed as an angiogram, such that signal intensity is a function of blood flow in the flow-sensitive direction. The signals from stationary spin and other factors causing phase shift, disappear after the subtraction [28].

Early implementations of this phase difference approach used spin-echo sequences [29], which are not well suited for blood flow studies since they tend to exhibit low intraluminal signal. Gradient-echo phase contrast methods are preferred and are used almost exclusively for such

work. However, in any practical applications, many modifications of the scan sequence need to be done to acquire a good quality image.

As with TOF MRA techniques, phase-contrast MRA can also be classified into 2D PC and 3D PC MRA. The application of 2D PC seems to be rather limited, while 3D PC techniques have been widely used.

The advantages of 3D PC MRA are:

- Only flow has a bright image, as opposed to images with TOF MRA where tissues with short T1 also give bright images.

- Good spatial resolution.

- Uniform signal throughout.

- Sensitivity to a wide range of velocities and hence applicable to arteries and veins.

- Possibility of imaging a large volume.

- Quantitative information becomes available.

Indicators of 3D PC MRA use in protocols:

- Suitable for high resolution studies.

- Can be used to study regions suspected of disease.

Major disadvantages of 3D PC MRA are:

- Longer acquisition time (nearly 30 minutes).

- Sensitivity to motion of patient resulting in artifacts.

- Greater demand on the equipment system, in terms of (a) stability, (b) eddy currents, and (c) computation.

2.2.3 Contrast enhanced MRA

The quality of MR angiograms has been improved considerably in the last few years due to optimization of the pulse design and examination protocols as well as hardware advancement. Nevertheless, signal loss is still a big problem which creates uncertainties in diagnosis, especially in situations where slow flow and in-plane flow (secondary flow) are significant. Based on extracellular contrast agents, such as gadolinium-DTPA (GD-DTPA), contrast enhanced MRA is routinely used to acquire images in difficult cases and is able to provide information about the intracranial vasculature, aneurysms, or carotid bifurcation anomalies.

In these techniques, contrast between the blood and stationary tissues is achieved by injecting a T1-shortening contrast agent into the blood stream. When imaged by using a short TR, short TE gradient-echo sequence, the blood appears very bright and stationary tissues appear dark. Vascular images acquired by using the contrast-enhanced MRA techniques have inherently high signal-to-noise ratios (SNR), and thus are affected very little by many of the flow-related artifacts that reduce the sensitivity and specificity of current MRA techniques [30].

However, the use of gadolinium contrast enhancement in MRA is not without potential disadvantages. For example, diffusion of the agent from the vascular compartment can cause a rapid drop in its plasma concentration. Normal soft tissues enhanced as a result of this diffusion can be projected onto final images generated by a standard maximal intensity projection (MIP) [31]. The variation of contrast agent concentration in plasma with time was clearly demonstrated by the time-resolved angiography study with bolus injection of a contrast agent [32, 33]. The variation can be used to study blood flow in lungs and heart [32] and to provide temporal information of blood flow from lungs, heart to renal arteries and veins by the 3D time-resolved imaging of contrast kinetics (3D TRICKS) [33]. However, this variation is likely to alter the phase-shift ($\Delta\phi$) due to the addition of the contrast agent to a solution compartment [34], which may lead to errors in velocity measurement. A quantitative analysis

of contrast-agent phase effects can be found in Akbudak et al [35]. The other disadvantage of contrast-enhanced MRA is that signals in veins are equally enhanced which will create difficulties in distinguishing arteries from veins.

The ideal MRA contrast agent should be completely intravascular, nontoxic, able to present at high levels in the blood-pool for longer than 30 minutes, relatively inexpensive, and have an effective elimination route [36, 37, 38]. An example of such a blood-pool marker is the Magnevist derivative, gadolinium-DTPA-polylysine, its large size and high molecular weight confining it to the intravascular source. In Vogl [39], the effects of Gd-DTPA and Gd-DTPA-polylysine were compared.

2.2.4 Phase-Contrast velocity measurement

Measurement of blood velocity is of great interest but is difficult to perform and requires techniques different from those used to acquire angiograms. The phase contrast cine MR imaging technique, first described by Nayler et al [40], has the capability of providing quantitative velocity measurement.

2.2.4.1 Electrocardiogram (ECG) gating methods and cine PC MRI

Electrocardiogram (ECG) gating is a very important method of obtaining time-dependent information. The earliest gated phase contrast approaches [40] are best described as multi-phase cardiac triggered. With knowledge of the patient's heart rate and the sequence TR, an estimate is made of the number of sequences that fit in one cardiac period. A train of sequences is triggered upon detection of the beginning of a cardiac cycle, all with the same phase-encoding amplitude in subsequent cycles to produce complete data sets. This method has two disadvantages stemming from beat-to-beat variations in the length of the cardiac cycle. One is that the first sequence in the cycle is preceded by a longer (and variable) relax-ation period than the others. This disrupts the NMR equilibrium and causes flashing artifacts in the first few frames. The second disadvantage results from the fact that the number of sequences per cycle is typically selected to occupy less than the entire cardiac period and

thereby ensure that the next period is not missed. As a result, this method has difficulty in examining the entire cycle. This can be somewhat improved by purposely selecting a number of cycles that will exceed one period. Whereas the entire cycle is then covered, the scan time is greatly lengthened and variation in the cardiac rate will temporally blur the late frames.

An alternative gating strategy acquires data at a constant rate (TR) and retrospectively sorts and interpolates the data into the desired number of frames per cycle. The term cine MRI or cine will be used here to refer to such techniques. Retrospective gating can be implemented in two different ways, namely real-time and off-line. The real-time approach handles the interpolation of the desired cardiac phases as soon as a line in K-space has been collected for a complete cardiac cycle. This puts some limitations on the type of interpolation, which has to be fast enough to be performed during the data acquisition. As a consequence, a linear interpolation between two k-space samples is most often used. The other way to implement retrospective gating is to make sure that each line in k-space is sampled at each part of the cardiac cycle, but not necessarily synchronized to the heart beats [41, 42, 43]. If information about the sampling time for each k-space line is recorded, it is possible to retrospectively interpolate the values for all k-space lines at any desired time. A disadvantage with this off-line method is that the acquisition of each k-space line has to be repeated long enough to cover even the longest RR interval. Since the variation in heart rate is not known in advance, each line is usually sampled over 1.3-1.6 sec to cover very long RR intervals. This off-line method is, however, more flexible with respect to the choice of interpolation method, as the interpolation is performed after all data have been acquired.

A fully retrospective cine MRI method has been described by Spraggins [42]. Normally, there are 16 pairs of equal time interval images in one cardiac cycle. At each time point, there are two images - magnitude image and phase image. The angiogram can be found in the magnitude image and velocity values in the phase image.

2D cine PC MRI is commonly used to acquire time-dependent angiograms as well as blood

velocities. However, one major problem associated with the technique is that the slice thickness is too large (normally more than 5 mm) to guarantee a high SNR, and the velocity data are the average values within each voxel. In regions with complex flow patterns, such as flow separation and recirculation, this averaging may lead to a large error. Apart from this, signal loss could be significant when measuring complex flows (discussed in section 2.2.6.2). This will limit the application of the cine MR PC velocity measurement approach in complex flow studies.

To enhance the spatial resolution perpendicular to the imaging plane, a high-resolution 3D phase-contrast imaging technique combined with off-line retrospective gating were used by Wigstrom et al (1996) in both MR angiography and quantitative flow measurement [44].

An important parameter of phase-contrast images is the strength of the flow encoding controlled by the difference of first moment M1 (as in section 2.2.2) in the same direction - ΔM_1. This can be characterized by the phase change per unit velocity. An intuitive alternative is the velocity, v_{enc}, that produces a phase shift of π radians or 180°:

$$v_{enc} = \pi \ (\gamma \ \Delta \ M_1) \tag{2.4}$$

This parameter is essential because it also represents the maximum speed that can be measured unambiguously. A velocity of $(1.05)v_{enc}$ will produce a phase shift of $(1.05) \times 180 = 189°$. This phase shift will give the same signal as $(189° - 360°)$ - namely -171°. Therefore, the velocity of $1.05v_{enc}$ and $0.95v_{enc}$ cannot be distinguished from each other. This effect is known as velocity aliasing, which can be minimised by applying algorithms that involve spatial continuity to resolve the ambiguity [45]. Otherwise only velocities within the range of $-v_{enc}$ to v_{enc} can be imaged unambiguously, and the measured phase shift is converted to velocity by the relationship:

$$v = (v_{enc}/\pi) \ \Delta \ \phi \tag{2.5}$$

However, in practical applications, converting from the signal intensity of the phase image

pixel to phase shift $\Delta\phi$ is a difficult undertaking. The conversion from measured pixel intensity to velocity has been accomplished by some MR scanner manufacturers using their internal data processing software, but it is not available in old version machines.

A large amount of work has been done on the use of Cine PC MRI techniques in studies of cardiac movement and ventricular blood flow [46, 47, 48, 49, 50, 51]. Although this technique is considered to be inadequate for generating the geometry of an arterial bifurcation because of its long scan time and large slice thickness, it is very useful for providing quantitative velocity measurement at boundaries of the CFD model. In such cases, the measurement section should be chosen in a relatively straight vessel where the flow is not disturbed. The velocity data can also be used to validate the CFD predictions.

2.2.4.2 Measurement of flow rate through a vessel

A main application of MR flow imaging is the measurement of volumetric flow rate through vessels. The cine PC acquisition yields velocity images in which pixel value is proportional to flow velocity. To estimate flow velocity with a two-point (single direction) technique, it is best to use an imaging plane that is perpendicular to the flow direction and to encode for through-slice motion. If the flow is oblique to the imaging plane, flow velocity will be underestimated by a factor of $cos(\beta)$, where β is the angle between the imaging plane and flow direction.

For through-plane flows, the product of the measured velocity and pixel area is the rate of flow through the pixel. If a region of interest (ROI) which includes the entire vessel lumen is defined and the flow rates in the inscribed pixels are summed, an estimate of the volumetric flow rate through the vessel can be obtained. As described already, if the flow is not parallel to the encoded direction, the velocity will be underestimated by $cos(\beta)$. However, the cross-sectional area is overestimated by $\frac{1}{cos(\beta)}$. Therefore, the product of the velocity at a pixel and the pixel area estimates the flow rate through the pixel independent of the exact flow direction.

In practice, the evaluation *will* have large error if the edge detection of ROIs is not accurate. Differences in individual flow measurements between operators could vary by as much as 24% [52]. Some effort has been made to improve the accuracy of flow measurement. In the above study, Burkart *et al* also developed an automated method of vessel detection which yielded flow measurements that were accurate in the model system and had significantly less inter-user variability than the manual method which was used conventionally.

2.2.4.3 Fourier velocity encoding technique

The velocity mapping techniques discussed above are methods that map the phase of the signal directly in order to measure the flow. Another PC velocity measurement technique developed and used by Feinberg et al [53], Hennig et al [54] and Dumoulin et al [55] is called Fourier Velocity Encoding in which a number of flow phase encoding steps separate the different flow velocities present at a particular location. In this strategy a thin slice is excited and a signal spatial dimension (that is, readout) is collected. The second dimension is converted from spatial encoding to velocity encoding through the use of a bi-polar phase encoding gradient pulse. The resulting velocity dimension provides quantitative flow measurements. Cardiac gating may be used and a number of frames acquired to provide a third 'dimension' (time).

Dumoulin et al [56] developed this technique to measure velocities at multiple positions simultaneously. The new technique employs a comb excitation RF pulse that excites an arbitrary number of slices while the Fourier velocity phase encoding gradient pulse is advanced. This causes the signals from the spins in a particular slice to appear at a position in the phase encoding direction, which is the sum of the spin velocity and an offset arising from the phase increment given to that excitation slice as shown in Figure 2.2. This technique could be used to measure the wave speed of arteries in pulsatile flow and then obtain density information for the vessels (Caro et al and Dumoulin et al [57, 58, 56]).

Another application of the method is the simultaneous measurement of multi-dimensional
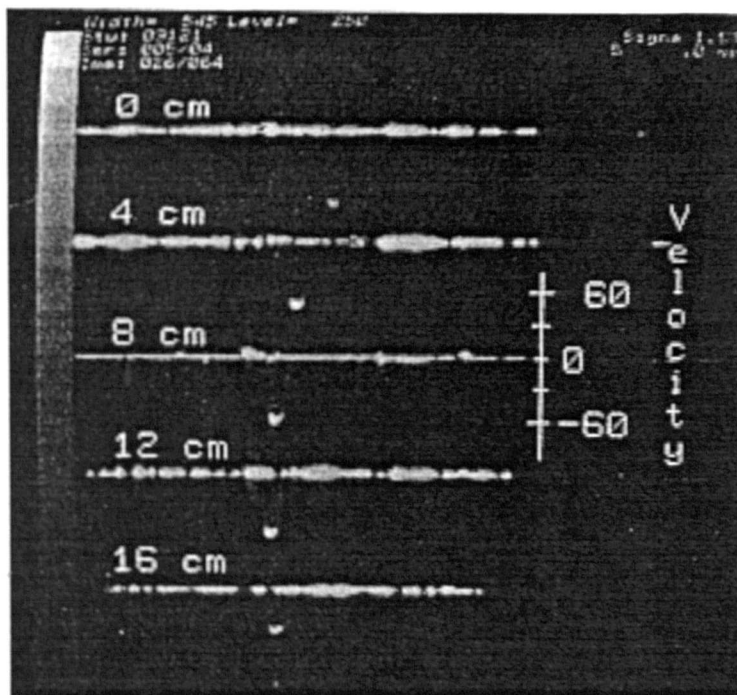
Figure 2.2: A Fourier velocity encoded image containing quantitative velocity information in the femoral artery of a healthy volunteer. Comb excitation was used to acquire data simultaneously from 5-mm slices with a 4.0-cm spacing. The data shown were obtained at 300ms after the detection of the subject's R-wave. From Dumoulin et al [56].

velocities [59]. It employs Fourier phase encoding to encode the first component, and phase contrast detection to encode the second. With this sequence acceleration information can be obtained.

2.2.4.4 Rapid phase flow imaging method

The methods previously described acquire flow data over a period of time that is long in comparison to the cardiac cycle. Rapid variations in flow cannot therefore be followed and the measured flow is a weighted average over the scan acquisition time. A number of rapid flow imaging techniques, including the echo-planar PC MRI, have also been developed.

Although the echo-planar PC MRI is a very complex technique, its ability to acquire an image within 40 ms is really attractive. A full description of the technique is beyond the scope of this review, but details can be found from [60, 61, 62, 63, 64].

2.2.5 Image Processing in MRA

Associated with the development of the MRI technique, many image processing techniques were developed and applied in the clinical MRI practises to perform angiogram generation, and even more complex techniques were used to demonstrate the velocity information on the diagnostic screen. In this section, some of the procedures are discussed.

2.2.5.1 Maximum Intensity Projection (MIP) Algorithm

The analysis of complex vascular anatomy, in particular the 3D path followed by most vessels, is greatly facilitated by postprocessing algorithms which provide a general overview of the anatomy. The algorithm most often used for evaluating 3D MRA data sets is the Maximum Intensity Projection (MIP) algorithm [65]. It creates a 2D display of a 3D data set. Using this technique, a series of parallel straight lines is projected through the set of images along a user-defined angle to determine the direction of projection for visualization of the 3D vascular structure. As the images are processed along this projection angle, the brightest

pixel within each image is extracted and used in the projection image. Thus, subtraction-like vascular images can be obtained. Since the algorithm is not very computationally intensive, it is extremely helpful in that it can provide rapid access to the MIP views. Some or all of the slices of MR images can be included in the projection volume, but the best results are obtained when only a limited volume is used. Too large a projection volume (involving many slices) increases the probability that smaller vessels and fine vascular details will be filtered out as noise [24].

2.2.5.2   Other Methods for Angiogram Generation

The MIP algorithm is quick and easy to use, but it is known to generate significant artifacts [31]. To improve the quality of angiograms more complex algorithms have been developed which provide the ability to select specific vascular features for evaluation and reduce the possibility of occurrence of postprocessing artifacts [66]. These algorithms are significantly more computationally intensive than is the MIP and require additional user interaction. Since high speed array processors have been introduced in processing MRA 3D data sets, it has become possible and practical to generate real three dimensional angiograms. Advanced visualization packages (for example AVS) can be employed to generate these kinds of three dimensional images. Murakami et al [67] compared MRA results postprocessed both by MIP and by a 3D computer graphic package. This latter involved using transverse MR images three-dimensionally reconstructed by a proprietary volume-based surface rendering algorithm called the linear surface extrapolator), the reconstructed images being able to be rotated, tumbled, or zoomed in real-time. The results show that fully 81% of the collateral vessels were seen by MIP images, but 98% of them by the 3D computer graphic images. The latter images provided complex anatomical information in a more easily understood fashion than transverse MR images of projection MRA (MIP images). These, of course, are very important information for clinical diagnosing and surgical planing. Most MR scanner manufacturers now provide some capability to postprocess 3D data sets. Some systems have integrated this capability into the operator's console whereas others have chosen to offer re-

mote evaluation workstations [68]. A review of applications of 3D imaging in medicine has been made by Zonneveld [69].

2.2.5.3   Velocity Image Processing

Different MR flow measurement methods will create different flow images. An easy way to show flow information directly is what is termed *flow visualization*. Mohiaddin and his colleagues at the Royal Brompton Hospital, London have made many contributions to MR velocity mapping and visualization. A technique they developed [70, 71] named MR velocity vector mapping allowed visualization of complex patterns of primary and secondary flow in the thoracic aorta and pulmonary arteries. Although the study was limited to two-directional flow in a single anatomical plane, the method provides information that might advance understanding of the human vascular system in health and disease.

Another MR flow velocity visualization technique was developed by Cline and his colleagues (in General Electric) in 1993 [72]. They combined blood flow information together with the corresponding vascular and brain surface. The calculated motion of a simulated bolus injection was derived from the measured velocity vector field and was animated to resemble cine angiography. This technique simplifies the flow analysis by replacing 3D blood flow vector fields with simple animation, this being readily acceptable for clinical interpretation. The resulting velocity field does not include the contribution of periodic cardiac motion (wall movement) since it is based on velocity averaged over several minutes. A much faster acquisition sequence would be required to show the periodic cardiac components of fluid motion.

2.2.6   Sources of error

MRA measurement errors may come from a number of sources of which the principal causes are: physiological motion, complexities in the flow, spins saturation and instrument error.

2.2.6.1 Errors caused by physiological motion

Lee [73] noted that the variation in delay between the ECG trigger and the start of acquisition could produce marked changes in image appearance. One value of the delay produced enhanced arterial edges with no signal within the artery, while another value might produce enhanced arterial edges along with a signal within the artery. Lee analysed the reasons for this ghosting and concluded it could be eliminated either by starting the acquisition earlier (by using a shorter delay), or by acquiring the data during a portion of the blood velocity curve that has even symmetry. Rogers et al [74] investigated the artifacts due to heart rate variations within the imaging period and showed that these artifacts were predictable and could be reduced by correcting the signal intensity for each phase view before 2D Fourier transformation.

Respiratory gating techniques have been used to minimize the ghosting effects caused by the respiration motion. But in cases where the imaging time for each slice is short, (for example the FLASH sequence takes 8 seconds and the T2-weighted turboFLASH takes only 2 seconds for each slice [75]), breath-holding is recommended in order to minimize respiratory artifacts. This is especially the case for both pulmonary and abdominal MRA.

2.2.6.2 Errors caused by complexity of flow

Local flow complexities may cause voxel dephasing and hence loss of signal in a complex flow region. This will lead to a volume overestimate when evaluating stenoses in a vessel. The underlying mechanisms of flow-induced spin dephasing have been described by several authors . Different methods have been proposed to reduce these artifacts, including flow compensation techniques (gradient motion nulling/refocusing), shortened gradient durations, reduced TEs and pixel size, bright blood flow and bright vessel techniques [76]. These methods have proved effective in relatively quiescent flows. The signal loss due to *turbulence* in a flow, (occurring for example in a poststenotic region), is however, more resistant to some of these techniques.

Kilner et al [77] reduced the TE of the field even-echo rephasing (FEER) velocity mapping sequence from 14.0 to 3.6 msec, so minimizing the problem of signal loss due to fluid turbulence in their measurements. The results showed that the 3.6-msec TE sequence enables accurate measurements of jet velocities of up to 6.0 m/sec (r = .996), but care had to be taken to prevent errors caused by misalignment, signal loss, phase wrap, or partial-volume effects.

In reporting their recent study on phantoms Furst et al [78] discussed the factors influencing the flow-induced signal loss in poststenotic flows. Their results indicated that flow model parameters (namely degree of stenosis, flow velocity) markedly influenced the length of post-stenotic signal loss (PSL) that could be compensated for by using shortened TEs and first order gradient motion refocusing (GMR). Varying flip angles had no significant influence on PSL.

2.2.6.3 Errors caused by spin saturation

In flow-related enhancement MR angiography (bright blood) one potential error is confusion of intravascular thrombus with flow because the short T1 of thrombi causes them to have a bright signal. This is usually resolved by bolus tracking and selective presaturation [24]. A thrombus will remain bright after presaturation, whereas flow can be directly visualized by bolus tracking or eliminated by appropriate presaturation schemes. In some cases changing the plane of section, the type of pulse sequence, or administering a contrast agent can be helpful.

Another source of error in flow-related enhancement MR angiography is in-plane saturation. This describes the tendency for spins to become saturated if they remain within the imaging slice for much of the acquisition period. Attenuation of the blood signal results in a consequent undesirable reduction in image contrast. There are several methods to overcome this problem, such as the use of thinner slices, smaller flip angle, and adjustment of the imaging plane. In-

plane saturation is related to the balance between the pulse sequence parameters and flow velocities in the vessel of interest.

2.2.6.4 Instrument Errors

The effects of eddy currents are particularly pronounced for techniques that require image subtraction. Phase contrast MRA typically relies on the acquisition of two images as described above. The two images are acquired with different gradient waveforms and therefore different eddy current responses. Such techniques are particularly sensitive to slight errors in the gradient waveform. Several techniques can be used to suppress these effects including using shielded gradients [79], and/or a pre-emphasis circuit [80].

Magnetic field inhomogeneities are an additional source of intravoxel phase dispersion. The effects are suppressed in spin-echo imaging by refocusing the 180° pulse, but are uncorrected in GRE sequences. Their effects can be minimized by the addition of small metal shims in the bore of the magnet at the time of installation.

2.2.6.5 Errors associated with cross-sectional images

When using 2D TOF images to generate 3D geometric models for computational flow simulation, the raw cross-sectional images form an important data set that has to be obtained. There are many factors affecting the accuracy of the cross-sectional images. Chien et al [81] discussed this problem and showed that in GRE imaging the measured luminal area can be affected by the RF flip angle due to its impact on the flow signal intensity. Spin saturation during diastole can cause a periodic variation in flow signal intensity, which may introduce errors in edge detection. This becomes worse when large flip angles are used in combination with a short TR. A flip angle of 20° − 30° was recommended to reduce spin saturation.

Partial volume effects are not linear in phase measurement in Phase-Contrast imaging. This somewhat subtle effect may lead to significant errors. A quantitative analysis of the partial volume effect has been made by Tarnawski et al [82], who showed that in the presence of

inflow enhancement partial volume effects tend to cause the flow rate to be overestimated. Another error which always exists is that moving blood shows an artificial shift in position which is related to the time delay between excitation and various spatial encoding steps. With sufficiently rapid flow or long TE, the blood may actually appear to be shifted outside the vessel lumen. In this case use of a short TE is necessary to avoid the error.

2.3 Medical image processing

From the preceding discussion, it is clear that the latest MRA techniques can provide 3D information about the arterial or cardiac anatomy. However, the raw MRA images need to be processed before any use can be made of them.

Over recent decades the impact of computational techniques on all fields of information science has been both profound and widespread. Digital image processing is one of the fields which has obtained most benefit from the advances in power of computing hardware. The development of increasingly sophisticated image processing algorithms has been a concurrent and complementary activity. In this regard, a sort of "push-pull" relationship has existed between processor hardware and algorithm development, so that as processor capabilities have expanded, new algorithms have been developed to exploit their capabilities. The available variety of algorithms is extensive, reflecting in many applications.

A typical image processing and analysis system comprises the following four stages:

1. Pre-processing

2. Feature extraction

3. Segmentation

4. Classification and description

The relation of these stages can be summarised as: image pre-processing improves the quality of raw data by reducing artifacts; feature extraction and selection provide the measurement-

vectors on which the image segmentation is based; segmentation groups pixels into regions; and classification is the step that deals with the labelling of the regions.

2.3.1   Image pre-processing

In general, due to the inherent technical limitations associated with the MR imaging process, uncertainties are introduced into the images. These include: random image noise, spectral leakage or Gibb's artifact [83], partial volume effects and MR signal intensity variation induced by nonuniform radio frequency fields. Nevertheless, the quality of MRA images depends primarily on the scan sequence used and flow conditions in the scanned vessel. A suitable choice of scan sequence and scan parameters is very important for obtaining a good quality image. A short TE, small flip angles and an appropriate Field-of-View are prerequisites for a good image. A high quality image can save a considerable amount of work in image pre-processing and minimise the risk of distortion introduced by image pre-processing.

A number of factors need to be considered when implementing a particular image preprocessing technique. These include the amount of information loss, the signal-to-noise ratio (SNR) gain, edge and fine detail degradation, and to a lesser extent computational complexity and time. Image pre-processing methods can broadly be divided into two categories: global techniques and adaptive techniques. For global methods, one transformation is applied to all the pixels of the input image, while adaptive methods involve an input-to-output mapping of the form

$$I_o(x, y) = f[I(x, y), O_\Omega(x, y)] \qquad (2.6)$$

here $O_\Omega(x, y)$ represents some local characteristics within the neighbourhood Ω around the location (x, y). Hence, the mapping function f changes adaptively with the local characteristics of the image.

Figure 2.3 gives a 2D TOF MRA image of the iliac arteries of a healthy adult. The bright
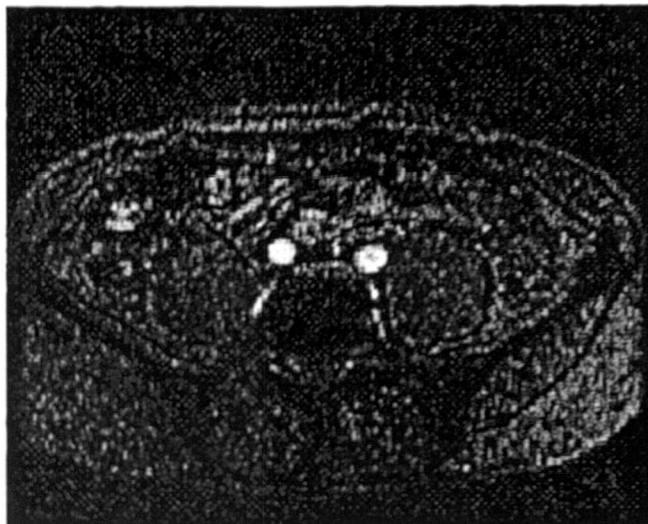
Figure 2.3: Original 2D TOF MR image acquired in the iliac arteries of a human subject.

circles are vessel cross-sections which are the Region Of Interest (ROI) of the image. To enhance image contrast, many techniques, such as the multichannel filter method [84, 85], adaptive local contrast enhancement method [86] and histogram equalization method can be used. One point should be noted here is that because the ROI is very small compared to the whole image, the global histogram can offer very limited information about the ROI or the edge of the vessel. In this case, Adaptive Histogram Equalization (AHE) [87, 88] and Contrast-limited Adaptive Histogram Equalization (CLAHE) [89] are more appropriate.

Another important aspect of image pre-processing is noise suppression. When considering the application of a filter method to medical data, image degradation by blurring or by artifacts resulting from the filtering scheme becomes unacceptable. The following requirements should ideally be fulfilled:

1. Minimization of information loss by preserving object boundaries and detailed structures.

2. Efficient removal of noise in regions of homogeneous physical properties.

3. Enhancement of morphological definition by the sharpening of discontinuities.

Some successful algorithms have been developed to treat this problem, such as local statistics, adaptive filtering algorithm [90] and gradient inverse weighted filtering algorithm [91, 92].

2.3.2 Image segmentation and geometry reconstruction

For the arterial flows of interest here, the specific aim of the MRA image processing is to generate the 3D geometry of the artery from 2D cross-sectional images. These can be achieved in two ways: (1) to segment 2D images in order to obtain vessel contours at the sections scanned, and based on these cross-sectional contours to generate the 3D contour image which will then be smoothed and interpolated to yield the 3D surface image of the vessel (2D segmenting, 3D smoothing); (2) to construct a 3D image from 2D images (obtain voxels of the image), and the 3D image will then be smoothed and segmented to give the final surface image (3D segmenting and smoothing). Both methods are discussed in detail below.

2.3.2.1 2D segmentation and 3D smoothing

In the method, the most important step is the image 2D segmentation. The main function of segmentation is data reduction without loss of 'useful' information. The image segmentation can be considered as a clustering process in which pixels are classified as belonging to a specific region based on their grey-level values and specific connectivity. Obviously such region formation is affected by both local information, i.e. the gray-level values of the neighbourhood pixels, and global information, i.e. the overall gray-level distribution of the image. A large number of algorithms with many approaches have been investigated. These approaches [93] include methods based on:

- histogram (thresholding);

- edge and boundary detection;

- region growing;

- linear feature.

Here we are only able to review those techniques of greatest relevance, with an emphasis on the Active Contour Models method. This latter is a particularly useful tool.

2.3.2.1.1 Thresholding Method   Gray level thresholding is the simplest segmentation process. A brightness constant or threshold can be determined to segment objects and background. Thresholding is computationally cheap and fast – it is one of the oldest segmentation methods and is still widely used in simple applications. It has a very simple algorithm: search all the pixels of the image, an image element of the segmented image is an *object pixel* if the grey-level of the pixel is larger than the threshold, and is a *background pixel* otherwise. Provided objects do not touch each other, and their grey-levels are clearly distinct from background levels, thresholding is a suitable segmentation method. However, only under very unusual circumstances can thresholding be successful using a single threshold for the whole image (global thresholding) since even in very simple images there are likely to be grey level variations in objects and background. These variations are, in fact, very significant in MR images. Segmentation using variable thresholds, in which the threshold value varies over the image as a function of local image characteristics, can produce the solution in these cases.

A key parameter which affects the performance of thresholding is the threshold (global threshold and local thresholds) detection. An easy and reliable way of threshold detection is based on histogram shape analysis. If the histogram is bimodal, pixels of objects form one of its peaks, while pixels of the background form the second peak, with the threshold value probably resulting from consideration of border pixels between objects and background. If the histogram is multimodal, more thresholds may be determined as minima between any two maxima. Each threshold gives different segmentation results.

Methods based on approximation of the histogram of an image using a weighted sum of two or more probability densities of normal distribution represent a different approach called Optimal Thresholding. In the algorithm, the threshold is set as the closest grey level corresponding

to the minimum probability between the maxima of two or more normal distributions, which results in minimum error segmentation. The difficulty with these methods is in estimating normal distribution parameters together with the uncertainty that the distribution may be considered normal. These difficulties may be overcome if an optimal threshold is sought that maximizes grey level variance between objects and background.

Thresholding is a very popular tool in image segmentation, and a large variety of threshold detection techniques exist. A review by Sahoo et al [94] gives a good overview of existing methods based on: histogram concavity analysis, entropy, relaxation, and multithresholding.

2.3.2.1.2 Edge and Boundary Detection Based Methods

Historically the first group of segmentation methods, which remains very important, is that based on information about edges in the image. Edge based segmentation methods rely on edges found in an image by using edge detection operators. These edges signify location in the image of discontinuities in parameters such as grey level, colour, and context, etc. But the resultant image from an edge detection technique can not be used as a segmentation result. In practice, this set of pixels seldom characterizes a boundary completely due to noise, breaks in the boundary from nonuniform illumination, and other effects that introduce spurious intensity discontinuities. Thus edge detection algorithms typically are followed by linking and other boundary detection procedures designed to assemble edge pixels into meaningful boundaries. Therefore, in the following discussion, edge detection techniques are reviewed first, and then boundary processing algorithms.

Edge detection

An *edge* is the boundary between two regions with relatively distinct grey level properties. Basically, the idea underlying most edge-detection techniques is the computation of a local derivative (or gradient) operator. Many gradient operators are used in edge detection in

order to measure the sheerness of edges. They are the Roberts operator, Laplace operator, Prewitt operator, Sobel operator, Robinson operator, and Kirsch operator [95]. Although these operators are very easy to use their results depend on the size of the object and its sensitivity to noise. It is important to realize that noise is always amplified when images are sharpened.

To obtain a good edge detection result and with minimisation of the noise, most of the modern edge detection techniques apply a smoothing process while sharpening the edge itself. The 2D Gaussian smoothing operator (also called a Gaussian filter) is always used to perform this smoothing process. It is defined as:

$$G(x,y) = exp\left(-\frac{x^2 + y^2}{2\sigma^2}\right) \qquad (2.7)$$

where σ is the standard deviation of the associated probability distribution which is the only parameter of the Gaussian filter σ is proportional to the size of neighbourhood on which the filter operates. Pixels more distant from the centre of the operator have a smaller influence, while pixels further than 3σ from the centre have no influence.

A good example of these edge detectors is the very-well known technique – Zero Crossings Edge Detection algorithm which use the fact that the zero cross points of the second derivative define the location of the edge. In this algorithm the Laplacian operator is used as an edge detector which is Gaussian-smoothed. The mathematical definition is:

$$\nabla^2 G = \left(\frac{r^2 - \sigma^2}{\sigma^4}\right) exp\left(-\frac{r^2}{2\sigma^2}\right) \qquad (2.8)$$

where $r^2 = x^2 + y^2$. Some authors use the abbreviation LoG, that is, the Laplacian of Gaussian (left hand side of equation 2.8, the second derivative of G with respect to r). The advantage of this approach compared with small size classical edge detectors is that a larger area surrounding the current pixel under consideration is taken into account; the influence of more distant points decreases according to the σ of the Gaussian. A further advantage is

that the σ variation does not affect the location of the zero crossings.

A further similar and very popular edge detector is the Canny edge detector which is optimal for step edges corrupted by white noise. The optimality of the detector is related to three criteria:

1. The detection criterion expresses the fact that important edges should not be missed and that there should be no spurious responses.

2. The localization criterion says that the distance between the actual and located position of the edge should be minimal.

3. The one response criterion minimizes multiple responses to a single edge. This third criterion solves the problem of an edge corrupted by noise and works against non-smooth edge operators.

As a conventional edge detector the algorithm of the approach is analysed in detail in Sonka [95].

Many image processing techniques work locally, in principle at the level of individual pixels i.e. edge detection methods. The essential problem in such computations is scale (σ in zero-cross method). Edges correspond to the gradient of the image function that is computed as a difference between pixels in some neighbourhood. The scale is the particular size of these neighbourhoods. The right size (scale) depends on the size of the objects under investigation. In the LoG approach, if the scale is too small then there will be many zero-crossings, most of them due to noise. On the other hand, if the operator scale is too large, the actual location of the zero-crossings may be displayed by several pixels, and some significant edges may become lost. Due to the nonuniform signal intensity distribution of a MR image, there is no single scale of smoothing sufficient to accomplish accurate edge detection on these kinds of image. *Adaptive scale selection* should be introduced, as explained below.

Garcia et al [96] presented a method for selecting proper scale parameters for edge detection. In their approach, there is a preliminary segmentation of the image into regions (R_i) with a homogeneous intensity change model. To find a proper scale for each region R_i, the scale σ is so chosen as to maximize the difference between the number of zero-crossings at σ and the number of zero-crossings at the next scale $\sqrt{2}\sigma$. The maximum of such a difference corresponds to significant information having been isolated at its proper scale as a result of removing the finer detail, at the same time there is an evidence of additional unnecessary smoothing (which would only distort the information of interest without removing it). Thus, once the image I is partitioned into a number of regions $R_1, \ldots, R_L$, each of them is described at its proper scale σ_i. As a consequence, the image I is represented in items of the scale vector $(\sigma_1, \ldots, \sigma_L)$ this vector then being applied to the edge detection itself.

Boundary Detection and Processing

As has been said, the resulting image from an edge detection method can not always provide a complete boundary. One aim of boundary detection and processing techniques is to obtain a complete boundary from sets of edge points or curves. There are many algorithms which are conventionally used to link the edge points and carry out boundary detection. They include: Edge image thresholding, Edge relaxation, Border tracing, Edge following as graph searching, Edge following as dynamic programming, and Hough transforms. Sonka et al describe these approaches in great detail [95].

In recent years, new algorithms have been proposed for boundary detection. Notably that of Yang and Li [97] and Basu et al [98]. In Yang's work dynamic mathematical morphology was employed for extracting shape information from an image. In Basu's work Variable Resolution (VR) Masks were used, whose centers are windows in normal resolution, with each of the peripheral cells used to keep some information at a reduced solution. In this way, VR approaches effectively look at a large region of the original image (or 'rough' view) at a computing cost only slightly higher than processing a small region using uniform resolution

schemes. By having this approximate look at a larger neighbourhood, the small gaps in edge can be filled and small noise contours can be avoided. The source code in C for VR boundary detection algorithms is available on request from the authors.

Active Contour Model (Snake)

A widely used and well developed approach to boundary detection is the active contour model which was first introduced by Kass, Witkin, and Terzopoulos [99] In this approach active contour models (snakes) start their search for a contour taking advantage of user-provided knowledge about the approximate position and shape of the required contour. Firstly an initial contour is placed near the boundary of the object in an image. The constraint forces which act on the snake push it towards the more accurate edge of the image by minimising the integral of the snake's total energy. This aim provides a general and unified treatment for elastic deformable models, and recently has become of wide application in image analysis and pattern recognition [100, 101, 102].

In the technique, the active contour model (snake) is a closed spline curve. The definition of 'snake energy' is slightly different with different applications and researchers. Normally, it includes internal energy E_{INT}, image energy E_{IMG} and external energy E_{EXT}. Hence the snake energy function defined by Williams and Shah's algorithm [103] is given by :

$$E = \int (\alpha(s)E_{cont}(s) + \beta(s)E_{curv}(s) + \gamma(s)E_{img}(s))ds \qquad (2.9)$$

where $E_{cont} + E_{curv}$ together comprise E_{INT}. In equation 2.9 s denotes the arc-length along the snake, and the energy term E_{cont} denotes a first-order continuity. It is given by

$$E_{cont} = \mid d - \|v_i - v_{i-1}\| \mid \qquad (2.10)$$

where v_i denotes the coordinates of the ith snake point (called snaxel by Williams and Shah),

$\|v_i - v_{i-1}\|$ the distance between v_i and v_{i-1}, and d the average distance between neighbors. The energy term E_{curv} (the curvature energy) is defined as

$$E_{curv} = \left| \frac{u_{i+1}}{u_{i+1}} - \frac{u_i}{u_i} \right|^2 \tag{2.11}$$

where $u_i = v_i - v_{i-1}$ and $\frac{u_i}{\|u_i\|}$ is a discreet approximation unit tangent at u_{i-1}.

The third term E_{img} the image energy, is set equal to the negative of either gradient magnitude or intensity. The sum of E_{cont} and E_{curv} is internal energy. The external energy E_{EXT} describes the high-level knowledge about the contour of objects and is always defined by the user. In Williams' work this item was not calculated. After minimizing the total energy E, a good contour could be obtained. Here minimizing the constituent E_{cont} forces the snaxels to be uniformly spaced, while minimizing item E_{img} forces the snake to seek points of maximum gradient or maximum intensity. All these energy terms must be scaled to lie in the same range.

After defining the energy terms, the key problem of the snake technique is the choice of the energy minimisation procedure of the active contour model. Many researchers have pointed out some of the problems in using the calculus, including numerical instability and a tendency for points to bunch up on strong edge portions. Originally (Kass *et al*, 87), a resolution minimization method was proposed; partial derivatives in s (arc-length) and t (time) were estimated by a finite difference method. Later (Amini et al) [104], a dynamic programming approach was proposed which allows 'hard' constraints to be added to the snake. In Williams and Shah, a 'greedy' iterative algorithm is presented in which each snaxel is moved to a new point in its neighbourhood whose energy is a minimum relative to other points in the neighbourhood. The algorithm terminates when the number of points moved becomes less than a preset threshold. In their approach in 1995 Chen and Lee [105] plant the search lines which are perpendicular to the initial contour, change the location of the contour points along both directions of searching lines and calculate the total energy. They used the same criterion as Williams to stop the algorithm. However, in Ranganath's work [106] the check for con-

vergence is based on the total energy of the snake, with iterations being terminated when the change in energy is below a threshold. The external force can sometimes be sufficiently large to make the snake oscillate around the equilibrium point so there was no monotonic decrease in energy. Ranganath found that a better indicator of convergence was obtained by checking for convergence after a block of iterations, typically 10. In each block of iterations, the range of the energy fluctuations was found. If this range were less than a threshold, then convergence was assumed. This technique was usually found to be more reliable than checking after every iteration. In addition he set a maximum number of iterations in case the convergence is very bad, this being so for some problems.

Difficulties with the numerical instability of the original method were overcome by Berger [107] by incorporating the concept of 'snake growing'. Their iterative snake growing always converges and the numerical solution is therefore stable. The detailed description of this algorithm can be found in Sonka's book (1993, p333) [95].

Not inconsiderable research has been done to improve the application of the snake in recent years by modifying the contour model. Cohen (1991) [108] introduced 'balloon model' to make the snake find its way. In the approach, an initial guess of the contour has to be provided manually. Accordingly, an internal pressure was introduced by considering the curve as an inflated balloon. The force due to this pressure is added to the internal and external forces to push the curve outward, as if air were being introduced inside. The curve both expands and is attracted to its edges. Separately, Cohen and Cohen make use of a "weight" force which simulates gravity into the 3D reconstruction models [109]. This allows them to be less demanding of the initialization and to give a simpler initial curve of their surface. The surface then 'falls' under the influence of the 'gravity', to catch an object which might be far from the border. The other contribution they made was replacing the finite-difference method (calculated the energy partial derivative equations) by a finite-element method. With the Finite-difference method, they only have knowledge of the functions at discrete points of a subdivision, and have no information between these points. Therefore, the distance between

successive points must be made very small to achieve sufficient precision. This is so as not to miss too much information because the external forces are applied at the grid points. They also used their algorithm to deal with true 3D MRI data and used deformable surfaces to extract the surface boundary of organs. This will be described in more detail in the section on 3D image processing).

Another very similar contour optimization technique is the Geometrically Deformed Model (GDM) introduced first by Miller et al [110], which describes a contour as a set of vertices, connected by edges. The energy function defined to control the GDM is quite different from that of the snake model; and comprises:

(a) a topology preserving energy term, dependent on an estimation of local curvature and the distance between a vertex and its neighbors;

(b) an image event energy term derived from the thresholded pixel values, and

(c) a locally defined deformation potential driving the vertices outward or inward.

The energy function is evaluated only for the vertex positions, not for the trajectory of the connection. This makes the model discrete; the length of the connecting edges defines, in fact, its resolution.

The approach of Lobregt and Viergever [111] was based on a development of this model. In their method the dynamic process controlling the contour refinement differs in nature from that of the GDM, and is described in terms of forces and force fields acting on the vertices rather than in terms of energies. The algorithm starts from an initial shape, the driving force behind the shape deformation being calculated from internal forces, derived from the shape of the contour model itself, and tries to minimize local contour curvature. The external force field is driven from some image feature energy distribution which will try to make the model follow a valley or a ridge through the 'landscape' formed by the image feature, that is, the pixel grey level. The deformation process is performed in a number of discrete steps, after each of which the situation with regard to position, velocity, and acceleration is evaluated for each

of the vertices. In this evaluation, forces on a vertex are calculated from the position of the vertex and its neighbours. These forces result in an acceleration, which changes the velocity of the vertex and, in its turn, the velocity determines the displacement of the vertex during the next deformation step. After a number of deformation steps, a stable end situation will be reached in which there is an equilibrium, described by the velocity and acceleration being zero for each vertex. The procedure avoids the following undesirable deformation effects:

- shrinking of closed models: by a proper definition of local curvature at the vertices, combined with internal forces that are zero for parts of the contour where the curvature is constant,

- clustering or gathering of vertices in corners of the models; by allowing only locally radial vertex displacements.

The above two effects are common in existing snakes.

Rueckert and Burger [112] developed an approach similar to GDM. Their adaptive spline model represents the object contour by a set of C^2 spline patches which are locally controlled by their defining control points. The splines they used are fifth-order polynomials which allow them easily to compute an interpolating curve which is C^2 continuous and provides local control. This is in contrast to natural cubic splines which are C^2 continuous but do *not* provide any local control. The concept of contour fitting is similar to the concept for GDMs. The contour fitting starts with an initial model which is placed by the user inside the object. The contour fitting algorithm then performs alternately a deformation and resampling process. The deformation process minimises the energy function of the model and the resampling process allows the spline model to adapt to the number of control points which are necessary to describe the object. If the length or the curvature of a curve segment exceeds a certain threshold, the curve segment is subdivided by adding a new control point. The contour fitting process stops if no further subdivision is necessary. This model has the following advantages:

- the energy due to elastic and bending deformations of the contour can be computed analytically, but needs a smooth shaped object which does not vary very rapidly,

- the contour shape is locally controlled: changing a control point of the adaptive spline model influences only the contour in the local neighbourhood of the control point.

2.3.2.1.3 Region Growing Methods The aim of the segmentation methods described in the previous section was to find borders between regions; the following methods construct a region directly. Region-based methods rely on the postulate that neighbouring pixels within the one region have similar values. This leads to a number of algorithms known as region growing namely, the merging, splitting, and split-and-merge approaches. Region growing techniques are generally better in noisy images where edges are extremely difficult to detect.

The general procedure of region merging (region growing) involves the following steps:

1. Define some starting method to segment the image into many small regions satisfying a given condition;

2. Define a criterion to compare one pixel to its neighbours. If the criterion is satisfied, the pixel is said to belong to the same class as one or more of its neighbours (merge) and this forms a region;

3. Merge all adjacent regions satisfying the merging criterion. If no two regions can be merged maintaining the given condition, the procedure is stopped.

From the above, the choice of merge criteria is very important in obtaining a good result. Homogeneity is an important property of regions and is used as the main segmentation criterion in region growing, whose basic idea is to divide an image into zones of maximum homogeneity. The criteria for homogeneity can be based on various factors, namely, grey level, texture, and model.

Basically, a merge criterion consists of two parts: a homogeneity test and a selection policy [113]. Two adjacent regions need to pass the homogeneity test in order to be merged. When several neighbouring regions pass the homogeneity test to merge with a given region, a selection policy is applied to choose one region from the several candidates to participate

in the merge.

In the homogeneity test, a fixed threshold test is a simple and widely used definition. In this test, the difference in feature measured between two regions (or pixels) is compared against a fixed, predefined threshold. If the feature difference exceeds this threshold, the two regions are considered non-homogeneous and a merge is denied. Otherwise, the two regions may merge if they also satisfy the selection policy.

A new approach for the homogeneity test is termed the adaptive test [114]. Unlike the fixed threshold test, the adaptive test-based homogeneity decision on local feature analysis is performed dynamically and automatically in the region growing process. The approach used is developed from existing multiple-threshold region growing algorithms which apply either position-varied, or time-varied thresholds in their segmentation processes. Position-dependent thresholds, determined using a priori knowledge about an image or by local thresholding techniques, are applied on different parts of the image. Time-varied threshold region growing refers to the application of varying thresholds during different stages of the region growing process. The algorithm of Chang and Li does not require a priori knowledge, nor does it depend on local thresholds obtained from regular sized subimages, but it uses both position and time-varied thresholds. To select the most suitable threshold for merging two regions, a feature histogram analysis is performed on the fly based on regions being formed in the merging process. The main advantage of the adaptive test is its sensitivity to regional feature variation. Also, unlike the fixed threshold method, the adaptive algorithm is easy to apply as it requires no parameter tuning. The drawback is that this test is more complex and requires more computation than the fixed threshold test.

Compared to the homogeneity test, the selection policy has been rarely reported in the literature. One method is 'best-merge' which requires the edge connecting two merging regions to be a minimum with respect to both regions, this was used in Willebeek's work [115]. The 'fast-merge' method used by Chang and Li [113] merges two regions which pass the homo-

geneity test if the value of the edge connecting them is a minimum with respect to either (not necessarily both) of the regions. 'Fair-merge' merges all regions which are considered equally suitable.

Having obtained a set of parallel 2D contours, the 3D image of the vessel can be generated by assembling the 2D images together with the set of distances between each slice in a longitudinal direction as shown in Figure 2.4. A number of approaches have been developed to construct the 3D geometry from parallel planar contours. Cline and his colleagues have made many contributions in 3D MR image processing [116, 117, 118]. One such is the development of an interslice connectivity algorithm called Marching Cubes [119] which was used by Kandarpa et al [120]. Porrill and Ivins [121] use a rational quadratic (conic) spline which was introduced by Farin [122] to fit the planar contour and then represent the 3D image surface with a tensor product conic spline which could deal with the surface bifurcation. In addition, Chen and Lee (1995) [105] carried out a 3D reconstruction of the bladder from a series of CT 2D images which were segmented by using the *snake* model. In this study, a 3D nonlinear interpolation scheme was used and initiated by the fast uniform sampling [123] of 40 points on each contour, and a linear interpolation technique for surface formation was pursued to reconstruct the surface of the object. The object was represented by stacking its contours, and the boundary surface of the object was formed by tiling triangular patches between each two contours [124].

However, it can be noticed from Figure 2.4 that the 3D vessel surface is not as smooth as it should be. To improve the quality of the 3D surface, A 3D smoothing algorithm has been developed specifically tailored for bifurcation geometries, The smoothing operation comprises two steps which will be described in the following chapter and part of the algorithm have been published in [125].
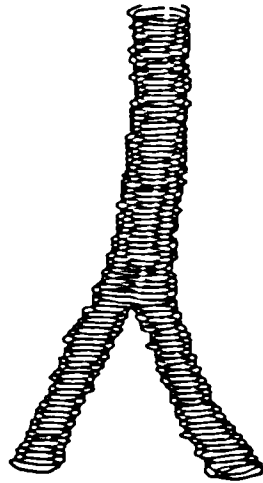
Figure 2.4: 3D contour image of a human abdominal bifurcation assembled directly from a series of 2D cross-sectional images.

2.3.2.2 3D segmentation and 3D smoothing

The first step in 3D segmentation is to detect the 3D edge in voxel images (3D images) in order to locate points corresponding to the surfaces of the 3D structure. The next step is to characterize the local geometry of these surfaces in order to extract points or lines which may be used for further analysis. Typically one must calculate second-order differential characteristics of the surfaces such as the maximum, mean, and Gaussian curvatures. The classical approach is to use local surface fitting, thereby confronting the problem of establishing links between 3D edge detection and local surface approximation. Monga et al (1991) first developed a 3D edge detection method in 1991 to process 3D NMR images [126] and subsequently to generate a theoretical link between the 3D edge detection and the local surface approximation using uncertainties inherent in edge detection [127, 128]. An improved algorithm was reported in their recent paper, Monga and Benayoun (1995) [129], where the curvatures were computed at locations designated as edge points using directly the partial derivatives of the image. By assuming that the surface is defined locally by an isointensity contour, one can calculate directly the curvatures and characterize the local curvature extreme from the first, second, and third derivatives of the grey level function. These partial derivatives can

be computed using the operators of the edge detection.

The extension of the *snake* model from 2D to 3D image segmentation was achieved by Cohen and Cohen in 1991 [108], by introducing a balloon model. A 3D generalization of the balloon model as a deformable surface, which evolves in 3D images, is presented in their later paper (1993) [109]. The *balloon* (corresponding to the *snake* in 2D) is deformed under the action of internal and external forces attracting the surface toward detected edges by means of an attraction potential. The method has been applied to MR image segmentation. To treat time-varying images, McInerney and Terzopoulos [130] described a 3D balloon model that could be inflated inside the volume of interest in multiple data slices. By applying this model to a sequence of 3D images it was possible to follow the deformation of the ventricular cavity.

Goshtasby and Turner [131] developed a procedure for segmentation of 3D cardiac MR images. In their approach, an estimation is firstly made of the locations of the ventricle by intensity thresholding and then the points are repositioned on the ventricular endocardial surfaces to those nearest locations where there are points with locally maximum magnitudes of gradient. The refined points are then used in the updated surface. These ventricular endocardial surfaces are represented by elastic surfaces whose degree of elasticity can be varied to control the smoothness of the reconstructed endocardial surfaces. To smooth out small intensity variations the volumetric image is convoluted with a 3D low-pass filter. The surface rendering is based on the assumption that ventricular endocardial surfaces have the shape of a generalized cylinder. The cross-sections of such a cylinder vary in shape and size with position along the axis of the cylinder, but their topologies remain the same. If an elastic generalized cylinder is fitted to the edge points of each ventricular surface then the cylinders will connect the points and smooth out the noise among them.

Hohne and Hanson developed a 3D image segmentation algorithm by allowing the user to segment images interactively using morphology functions [132]. This segmentation is performed concurrently with 3D visualization providing direct visual feedback to guide the user

in the segmentation process. Thus, rather than attempting to duplicate the complex and poorly understood human pattern recognition capability, the approach relies on the user's judgement and knowledge. The drawback is that the computational requirement for such an interactive 3D image processing approach is high. Another important 3D image smoothing and edge detection method is that of *nonlinear diffusion* introduced by Alvarez *et al* [133], and based on the "mean curvature motion" equation. The algorithm appears to be the sharpest possible among the multiscale image smoothing methods preserving uniqueness and stability A recent development of the *nonlinear diffusion* method, has been made by Kacur and Mikula [134].

2.3.2.3 Summary

Two types of method for 3D geometry reconstruction using 2D cross-sectional MR images have been described. These are:

1. 2D segmentation and 3D smoothing

2. 3D segmentation and 3D smoothing.

Type 2 methods have the advantage of requiring less operator interaction than type 1. Moreover, type 2 methods consider a 3D geometry (topology) as a whole which means that complex topological structures can be handled relatively easily. Nevertheless, this class of methods involves complex algorithms and high CPU consumption. They have less control of the image when the 2D image intensity levels are not uniform between each slice. It is also difficult to correct errors due to the random movement of the scanned subject. The first type of methods, on the other hand, uses relatively simple algorithms and has direct control of the signal intensity nonuniformity between each slice. In the smoothing step, measurement errors due to various reasons can be treated individually. However, they are difficult to implement when complex topological structures are involved and need more operator input when image qualities are poor.

2.4 Computational Fluid Dynamics Methods

Fluid mechanics problems can be investigated either by laboratory experiment or by numerical solutions of the governing equations or a combination of both. In CFD simulations of blood flow in arteries considered here, *in vivo* measurement of blood velocities are used as boundary conditions for the solution of the governing equations (here the Navier-Stokes equations). The governing equations are nonlinear partial differential equations and cannot be solved analytically except for highly simplified cases. However, they have been successfully treated by using various approximate numerical approaches including finite difference, finite volume, and finite element methods. To solve these equations numerically, it is necessary to discretize the fluid domain into a large number of contiguous, small-sized elements which form a computational mesh, or grid. The grid can be *structured, unstructured or hybrid* but its generation is subject to various constraints. In fact, at present, it can take orders of magnitude more man-hours to construct the grid, than it does to construct and solve the physical problem with the grid. In this section, grid generation in arterial bifurcations is discussed, followed by a brief description of the equation solver (which will be discussed in detail in Chapter 5). Finally, post-processing techniques necessary to display the whole field results are reviewed.

2.4.1 The computational mesh

The generated mesh must be sufficiently dense to ensure that the numerical approximation is accurate, but it cannot be so dense that a solution becomes impractical to obtain. Generally speaking, the grid spacing should be smooth and sufficiently refined to resolve changes in the *gradients* of the solution. The mesh should also be constructed with computational efficiency in mind. The accuracy of a numerical approximation can be impaired if the quality of the mesh is poor.

The terms used above are now defined more rigorously. A *mesh* is a set of points distributed

over a computational domain for a numerical solution of a set of partial differential equations (PDEs). This set may be *structured* or *unstructured*. In a structured mesh, the points form quadrilateral cells in 2D or hexahedral cells in 3D. An unstructured mesh generally consists of triangles and tetrahedral cells in 2D and 3D, respectively, in its most basic form.

Normally used for finite-difference and finite-volume approaches, a structured grid can give a regular lattice structure which provides easy identification of neighbouring points. A structured grid also provides a more natural representation of normal derivative boundary conditions and allows more straightforward approximations based on prevailing directions. For example directions are chosen parallel or normal to a boundary or flow axis. This structure can lead to a much simpler data set construction and allow the use of directional time splitting and flux representations. In most haemodynamics applications a boundary-conforming mesh has been used. A structured boundary-conforming mesh requires that a curvilinear surface (for a 3D problem) grid first be scribed on the boundaries so that smooth, continuous volume grids can then be generated into the interior [135].

A structured grid can be generated algebraically by interpolation from boundaries, or by solving a set of PDEs[1] in the region. Basically, the algebraic generation systems are faster, but grids generated from PDEs are smoother. The hyperbolic generation systems are faster than elliptic systems, but are more limited in the geometries that can be treated. The elliptic systems are the most widely applicable methods for problems with complex boundary configurations, but transfinite interpolation is also effective in a composite grid framework. The principles of these systems are well known and the techniques have been well developed over recent years. A number of comprehensive reviews of the field have been published [136, 137, 138, 139, 140].

It is known that structured meshes, whether derived from algebraic methods or partial differential equations, result in a set of curvilinear coordinates. One way of viewing this is that,

---

[1]These PDEs have nothing to do with the fluid flow governing equations, here the Navier-Stokes equations.

physical domain   computational domain
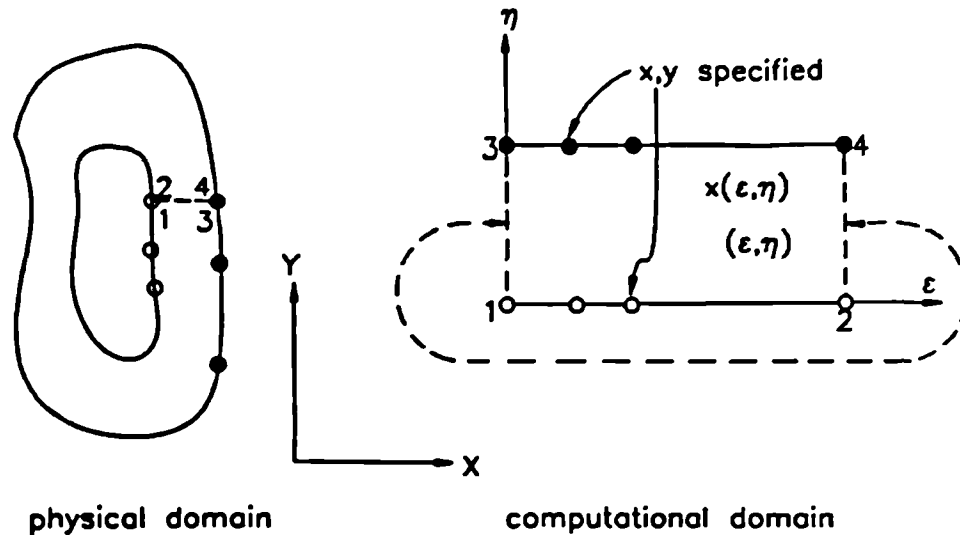
Figure 2.5: Mapping of structured grids from the physical domain to computational domain.

In two dimensions, the physical domain is mapped on to a rectangle in the computational domain, as shown in Figure 2.5. However, for realistic geometries, it is very difficult to obtain a reasonable grid with the entire physical domain transferred to a single rectangular domain. To resolve this, an important concept in grid generation for complex geometries

the *block-structured* (or *multi-block*) grid — needs to be introduced. The concept is to segment the physical domain into a number of topologically similar contiguous blocks, with grids being generated in each block. This allows both the grid generation and numerical solutions on the grid to be constructed to operate in a logically rectangular computational region, regardless of the shape or complexity of the full physical region. The full region is treated by performing operations for the solution in all of the logically rectangular computational blocks. The generally curved surfaces bounding the subregions in the physical region form internal interfaces across which information must be transferred, that is, from the sides of one logically rectangular computational block to those of another. These interfaces exist in pairs, an interface on one block being paired with another on the same, or different, block since both correspond to the same physical surface. Complete continuity of grid lines across the interface requires that the interface be treated as a branch cut on which the generation

system is solved just as it is in the interior of the blocks. The interface locations are then not fixed, but are determined by the grid generation system. This multi-block structured grid approach is now widely adopted in CFD solvers.

Surface grid generation is another important element of grid generation in dealing with complex geometries. It can be regarded as a 2D problem in its own right, and can be performed either by interpolation or by a PDE solution method. In general, this is a 2D boundary value problem on a curved surface, that is, the determination of the locations of points on the surface from a specified distribution of points on the four edges of the surface. The initial points on the surface can be obtained by measurement. Those interpolation methods based on cubic splines tend to be best for treating existing surfaces when it is important to preserve the original data points, because these approaches usually guarantee that the resulting surface will pass through the data. However, when the data are sparse, the region between data points may depart unacceptably from the measured surface. B-splines and nonuniform rational B-splines (NURBS) can be used to approximate an existing surface. However, they may not preserve the original points, but in general produce a smoother surface than classical cubic spline methods.

Yu and Soni [141] presented their recent work on surface structured grid generation and discussed the application of NURBS to the problem of grid generation for complex industrial geometries. Geometrical entities are transformed and represented using NURBS with common data structures. Techniques for reparameterization are discussed in terms of various grid topologies and distribution requirements. Elliptic grid generation methods for the construction of surface grids are discussed in Khamayseh and Mastin [142], an improved elliptic surface grid generation method for parametric surfaces being presented. Two methods of imposing grid orthogonality have been implemented and several control function options developed for maintaining a desired distribution of grid points on the surface. The overall effect of these improvements gives a reliable and versatile elliptic method for generating and improving surface grids. Several other researchers have also made contributions to surface
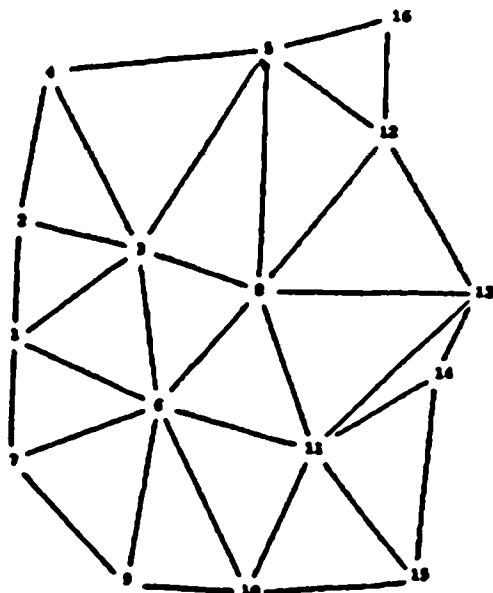
Figure 2.6: Unstructured grid of triangles showing node numbers and element connectives.

grid generation. (Chan and Buning, 1995 [143], and Knupp, 1993 [144]).

An *unstructured* grid permits an alternative approach to accommodate complex geometries. Any grid in which the points cannot be arranged in a regular array (i, j, k), with the assumption that the points $(i, j, k), (i, j+1, k)$, etc. are neighbours, is an unstructured grid, as shown in Figure 2.6. Hence, the description of an unstructured grid requires not only a list of coordinates of points, but also the connections between points to define the elements. This lack of any global pattern implies that points and elements of general shape can be introduced into a domain wherever it is appropriate. Hence, unstructured grids are well suited for applications to complex geometrical regions and grid adaptation. Traditionally, the element types used have been triangles (for 2D) and tetrahedral (for 3D). The equation solving method for an unstructured grid is based on a finite element method (FEM).

The requirements for unstructured grid qualities are not so strict as for structured grids. Here

the important thing is the grid point distribution in the flow domain and the formation of conforming, non-intersecting elements. In general, it should be appreciated that two distinct problems of *point creation* and *point connection* have to be solved in generating the grid. Many different techniques can be used to generate an unstructured grid, such as Delaunay Triangulation [145], and advancing front methods [146, 147] these latter constructing a mesh of a domain from its boundary information; namely Quadree (2D) and Octree (3D) [148]. A number of review articles on unstructured grid generation techniques has been published [149, 150, 151]).

The principal advantage of an unstructured mesh is that it provides a very powerful tool for discretizing domains of complex shape. However, such a mesh is poorly ordered and is therefore less amenable to the use of certain algorithms and vectorised computers. In addition, it requires considerably more computer time and storage, as well as a much more involved data handling procedure than does a structured mesh.

2.4.2 Numerical solution techniques

The haemodynamic problems considered here can be described as 3D, time-dependent, incompressible, viscous, laminar flows. To simulate such flows, the full Navier-Stokes equations should be treated. Producing the transformation of a partial differential equation to what is known as a numerical analogue of the equation is called *numerical discretization*. In this discretization process each term within a partial differential equation must be translated into a numerical analogue that the computer can be programmed to calculate. A variety of techniques can be used to perform the discretization and, while each technique is based on a different set of principles, there are many common features in the methods that are used. Here we discuss three major approaches namely the finite difference, the finite element and the finite volume methods.

2.4.2.1   Discretization methods

Historically, the preferred approach for CFD has been the finite difference method (FDM). It is based upon the use of so-called Taylor series to build a library or toolkit of equations that describe the derivatives of a variable in terms of the differences between values of the variable at discrete points in space or time. A comprehensive reference to the finite difference method is given by Smith [152]. By subdividing the physical domain under consideration into computational grids, the derivatives at each grid point can be replaced by the appropriate difference formula, giving an equation that consists solely of the values of variables at the given point and its neighbours. If this process is repeated at all the points, a set of equations for the variables at all the points are formed and these are solved to give the numerical prediction. However, in so doing there is no guarantee that the above principles of conservation of momentum and mass will be *locally* satisfied .

In the finite element method (FEM), the domain over which the partial differential equation applies is split into a finite number of sub-domains known as elements. Over each element a simple variation of the dependent variables is assumed and this piecewise description is used to build up a picture of how the variables vary over the whole domain. A good introductory text to the finite element method is that of Reddy [153]. Because there is a local summation of surface and volume effects, local conservation is retained, subject to the accuracy of the above assumption.

The third, and probably the most popular, numerical discretization method used in CFD is the finite volume method (FVM). It is similar in some ways to the FDM, but some implementations of it also draw on features taken from the FEM. The FVM was developed specifically to solve the equations of heat transfer and fluid flow ensuring local volumetric conservation and is described in detail by Patankar [154].

The common features involved in using these techniques may be summarised as follows:

1. Production of equations for the values of the variable at a finite number of points in the domain under consideration;

2. Requirement of a set of initial conditions to start the calculation for a time-dependent problem;

3. Requirement of boundary conditions, i.e., values of the variables at boundaries.

There are, however, a number of differences including:

1. The FDM and the FVM both produce numerical equations at a given point based on the values at neighbouring points, whereas the FEM produces equations for each element independently of all the other elements. It is only when the equations are collected together and assembled into the global matrices that the interaction between elements is taken into account.

2. The FEM takes care of derivative boundary conditions when the element equations are formed, and fixed values of variables must be applied to the global matrices. This contrasts with the other two methods which can easily apply the fixed-value boundary conditions by inserting the values into the solution, but must modify the equations to take account of any derivative boundary conditions.

Finite difference methods are based on the substitution of difference equations for the partial derivatives in partial differential equations. These difference equations link the values of variables at a set of points to the derivatives and so a grid of points is used throughout the spatial domain. If the distribution of points with a regular topology is used, then the calculation procedure carried out by a computer program is likely to be extremely efficient and hence very fast.

Finite element methods, on the other hand, produce the numerical equations for each element from data at known points on the element and nowhere else. Consequently, there is no restriction on how the elements are connected so long as the faces of neighbouring elements are aligned correctly. By this the faces between elements should have the same nodes for each

of the adjoining elements. This flexibility of element placement allows a group of elements to model very complex geometries.

Algorithms that have been developed using the FVM have tended to use a regular grid to take advantage of the efficiency of computation, just like the grids used with FDM. Recently, however, to enable calculations to be carried out in complex geometries, algorithms have been developed with the FVM that can utilize irregular, finite element-like meshes (unstructured grids). It is the concept of the inter-volume flux across a face that enables this to be done. Both finite element and irregular mesh finite volume programs pay a computational overhead for this geometrical flexibility. This overhead slows the programs down considerably.

2.4.2.2 Commercial CFD codes

It is increasingly common, even in the academic community that CFD capabilities are obtained most cost-effectively through the purchase of a commercial CFD code. There are many commercial CFD codes available now to suit different applications. Here we focus on CFX4, but this should be viewed as an example of a number of codes with similar capabilities. For instance, a very recent survey by Gosman 1997 [155] focused on an alternative code.

CFDS-CFX4 (previously named CFDS-FLOW3D), developed by the Computational Fluid Dynamics Services, UK [156], is a FVM based code using a structured, patched multi-block, nonorthogonal, curvilinear coordinate grid with a collocated variable arrangement. The basic solution algorithm is the SIMPLEC pressure correction scheme which uses a variety of linear equation solvers. Spatial discretization is achieved through the HYBRID scheme, a second-order upwind scheme, and the third-order QUICK scheme. CFDS-CFX4 has models for multi-phase flow, particle transport (for steady flow only), gaseous combustion, chemical species concentration, thermal radiation, compressible and incompressible flows, porous media flow, and conjugate heat transfer. A more detailed description of the package about the equation solving, boundary condition using and code validation can be found in a separate chapter (chapter 5).

Many CFD packages have their own pre-, and post-processors which deal respectively with grid generation and effective visualization of whole field results, which latter can be 3D, time-dependent or both. Problems associated with grid generation have already been dealt with, and it remains now to address the post-processing, that is, visualisation of 3D time-dependent data.

2.4.3 Post-processing Techniques

When the numerical solution is obtained it is necessary to determine whether or not it bears some prima facie relationship to the physical reality. If it is likely that it does, the required technical information can be extracted from the results.

Information can be produced by the solver in two main forms. These forms differ in the manner of data storage in the computer. In one form the data are stored using an internationally agreed format known as *ASCII format* which can be edited by text processor and other software, and they are effectively machine-independent. The other data storage format is known as *binary data format*, for which although there is a standard the method is usually particular to each computer operating system or computer manufacturer. Binary files are smaller in size than ASCII files for the same information.

The type of the information produced by the solver program can usually be controlled in *user defined subroutines* but it often consists of the following:

- Values of the residual error for the various partial differential equations that have been solved.

- Values of some of the variables at a limited number of locations, known as *monitor locations*, for every iteration or time step.

- Mesh data and a completive list of the flow variables at all the nodes of the domain or all the cells of the domain. These results are usually stored in binary format for the

sake of saving disk space.

A post-processor is required to have two basic functions: (1) data interpolation, and (2) graphic display or visualization.

2.4.3.1 Data interpolation

Most post-processing packages assume that the mesh and variables are stored at the same physical locations. However, for a cell-centred treatment, such as that in CFDS-CFX4, the grid and variables are not at the same positions. The coordinates of cell corners are stored in the dump file, these values giving a geometrically accurate representation. The variables are located at the cell centers, and if a mesh based upon the cell centers was used, it would be in error by half a grid cell at the boundaries. For this reason it is necessary to interpolate variables to cell corners. The interpolation procedures are carried out in a solver supported post-processor, such as JASPER in CFX, before it writes data out to other formats.

It is also a common practice to interpolate data for variables from node points to a chosen location in order to display the vector or contour on a chosen plane or along a chosen line in the flow domain. Most post-processors can offer vector plots, contour plots and mesh display for simple geometries. However, for human artery bifurcations which are 3D, asymmetric, curved, and non-planar with irregular cross-sections, flow visualization becomes extremely difficult. It is impossible to specify a plane where velocity vectors in the whole field can be displayed. To visualise the flow patterns in these models, new concepts such as *streamline*, *particle tracking* and *particle residence time need* to be introduced which involve considerably more complex data processing and calculations.

The *streamline* plot creates approximate 'presentation quality' streamlines to show the flow field in a problem. They are defined as curves tangential to the instantaneous flow field. In a steady flow, a streamline coincides with the path a particle would follow when released from some location. In unsteady flow, streamlines and particle paths are different. The calculation

of streamlines amounts to integrating:

$$\frac{d\vec{x}}{d\tau} = \vec{u}(\vec{x}) \tag{2.12}$$

where x is the position in space and $\vec{u}$ is a velocity field. The integration variable, τ is a pseudo-time variable because the integration occurs only at one instant in time.

To describe the flow direction and twisting, a number of algorithms have been developed to construct the streamribbons and streamtubes. Streamribbons are streamlines that have been given some width and rotation based on the local streamwise vorticity. Many implementations of streamribbons calculate two streamlines with the second line constrained to remain a constant distance from the first line. The end results are fed into a complicated algorithm to build ribbon surfaces. The precise definition of a streamtube is the surface formed by all the streamlines passing through a closed contour. A detailed description of algorithms for generating streamlines, streamribbons and streamtubes can be found in Darmofal and Haimes [157].

Most of the commercial post-processing packages can generate streamlines and or streamribbons such as AVS, PLOT3D, GRAFIC, VISUAL3, ENSIGHT and CFDS-FLAVIA. They are accurate for flows that do not change directions sharply, but for other flows the streamlines may have small errors or be incomplete. Each point along a streamline is calculated from the velocity data which do not consider the particle mass or momentum. More accurate streamlines can only be obtained by using a particle tracking module in steady flow when solving the governing equations. For example, in CFDS-CFX, the particle tracking module works by considering two phase flow (particle as one phase) and the particle can have mass.

For unsteady flows, data at each time step are required. A common approach is to use instantaneous flow visualization techniques to display the flow at individual time steps. Thus for a given time step, streamlines, vector plots, and contour lines are computed and sometimes saved for playback. By animating the streamlines, contour plots and vector plots computed

at each time step, one hopes to see, appreciate and understand the time-varying phenomena in unsteady flows. These methods are commonly used to show the flow characteristics but they are not adequate to reveal such phenomena as vortex formation, travel and breakdown, neither can they give particle residence times which are of great importance in analysing the blood and arterial wall interactions. In order to depict these phenomena, *time* needs to be considered in the calculation. Because instantaneous flow visualization techniques treat results at each time step independently, so no connection is made among the results at different time steps.

In unsteady flows, particle trajectories are obtained by tracking a massless particle from an injected position and time, to the time the particle disappears from the flow domain. Connection of the position points at each time step forms the particle pathline. The time between the entering of the particle and its exit from the flow domain is the residence time of the particle. Particle tracking algorithms have been subdivided into two classes (1996) [158]. They are (i) multi-step, and (ii) multi-stage schemes.

A generic multi-step scheme has the form:

$$\sum_{i=0}^{s} \alpha_i \bar{x}^{n+1-i} = k \sum_{i=0}^{s} \beta_i \bar{u}(\bar{x}^{n+1-i}, t^{n+1-i})$$

(2.13)

where s is the total number of steps, $\alpha_0 = 1$, and either α_{n+1-s} or β_{n+1-s} is non-zero. For implicit schemes, $\beta_0 \neq 0$ and a nonlinear system of three equations (three dimensions) must be solved at every time step for the new particle position $\bar{x}^{n+1}$. An advantage of multi-step schemes is that only one velocity field $\bar{u}^{n+1}$, is needed to calculate the new particle position, $\bar{x}^{n+1}$.

Multi-stage schemes are difficult to write in a single, unified form. A classic 4-stage Runge-

Kutta algorithm is usually employed which can be written as:

$$\vec{a} = k\vec{u}(\vec{x}^n, t^n),$$ (2.14)

$$\vec{b} = k\vec{u}(\vec{x}^n + \frac{1}{2}\vec{a}, t^n + \frac{1}{2}k),$$ (2.15)

$$\vec{c} = k\vec{u}(\vec{x}^n + \frac{1}{2}\vec{b}, t^n + \frac{1}{2}k),$$ (2.16)

$$\vec{d} = k\vec{u}(\vec{x}^n + \vec{c}, t^n + k)$$ (2.17)

$$\vec{x}^{n+1} = \vec{x}^n + \frac{1}{2}(\vec{a} + 2\vec{b} + 2\vec{c} + \vec{d})$$ (2.18)

A difficulty with multi-stage schemes is that they frequently require velocity data at intermediate times between t^n and t^{n+1}. Since the velocity data are only available at t^n, the velocity at intermediate times must be interpolated from the previous and or the current velocity fields. For equally-spaced time intervals, a desired fourth order interpolation given by Darmofal is:

$$\vec{u}^{n+\frac{1}{2}}(\vec{x}) = \frac{5}{16}\vec{u}^{n+1}(\vec{x}) + \frac{15}{16}\vec{u}^n(\vec{x}) - \frac{5}{16}\vec{u}^{n-1}(\vec{x}) + \frac{1}{16}\vec{u}^{n-2}(\vec{x})$$ (2.19)

While the velocity is being interpolated in time, the spatial position remains fixed at the x location desired.

Spatial interpolation means the interpolation of velocity values into a specified location. The key problem associated with spatial interpolation is to find out in which cell the particle is located. It is relatively straightforward with a fixed grid problem. However, additional complications arise when a moving grid is concerned. In this case, the previous grid information (for example, spatial locations of nodes) is also necessary to interpolate the velocity field at the desired intermediate time. Also, if the particular spatial location does not exist at a previous time needed to form the time interpolant, the time interpolant cannot be constructed and the particle integration aborts. With a multi-step algorithm, the particle integration aborts only when the particle actually encounters a domain boundary at the current time [157, 158, 159].

2.4.3.2   Visualization

Flow visualization is the final step for a CFD simulation. Visualization packages can be grouped into three categories. The first category comprises subroutine libraries such as Ghost, NAG Graphics and Uniras. These subroutines can be easily called to purpose-build visualization programs for simple or limited special applications. It is very difficult to carry out the complex tasks we have described above by calling these subroutines. The second category is turnkey systems such as Uniras, Data visualiser, Intelligent Light, NCSA Tools and PV-Wave. Software packages belong to this category have their own environment and good user interface, but are specified and only allow straightforward applications. The third category consists of 'application builders' such as AVS, apE, Khoros, and IRIS Explorer. These packages can perform sophisticated 3D visualization and permit user-organised applications.

Current systems are based on the following description in which a visualization technique is seen as four separate processes:

1. Data input: data can be structured (field) or unstructured cell data (UCD).

2. Filtering Reconstruction: interpolating data and/or generating vector or scalar data from the input.

3. Mapping to Abstract Visualization Object: slice, contour map, image display, surface view and vector drawing.

4. Rendering and output: display on graphics device and writing out of the chosen plot to an output file (normally in PostScript format).

There are a number of subroutines involved in each of the above processing stages. A particular application can be achieved by generating a special network which connects the subroutines from steps 1 to 4. A notable feature is that these packages offer the facility to incorporate user-written modules which allows advanced users to develop their own image processing subroutines to meet special needs.

The software packages discussed above are general purpose image visualization packages. Based on visualization techniques, some specially designed packages for the processing and displaying of CFD data have been developed in recent years. These include CFX-Visualise, EnSight (Engineering inSight), PLOT3D, Flow Analysis Software Toolkit (FAST). These packages normally supply powerful, easy-to-use tools through a user-friendly Motif user interface. They can calculate scalar and vector fields, plot surfaces of structured unstructured grids, compute streamlines and/or particle traces through the structured unstructured vector fields, display arbitrary cutting planes and contours, extract critical points in a vector field, plot 2D graphs of scalar functions and act as a conventional text editor for graphics. It is evident that, armed with these tools, a CFD worker can probably construct any kind of haemodynamics-related behaviour of clinical significance. However, such is very likely to involve painstaking development work.

2.5 The combination of MRA and CFD

2.5.1 Earlier work

Because of the ability of non-invasive measurement of geometry and blood velocity, MRA has been used in both laboratory and clinical studies of haemodynamics for several years. However, with all of the uncertainties in measuring velocity especially in situations with complex flows, MR measurements are subject to errors. To help understand and assess the degree of signal loss and hence the errors associated with MR measurements in various applications, well established CFD techniques have been increasingly used in recent years [160, 161, 162, 163, 165, 166, 167]. A typical procedure can be described as follows:

- CFD predictions of velocity field in a given geometrical model.

- Generation of particle trajectories using the predicted velocity data.

- Development of the relationship between a travelling particle and the normalized signal intensity of the particle according to the MR scan sequences.

- Calculation of pixel intensity at specified planes and display of simulated MR images.

- Comparison with the MR measured images acquired from *in vitro* models or *in vivo* subjects.

This procedure has been employed by a number of researchers. In a study performed by Vantyen et al [160], CFD techniques were used to provide flow streamlines through curved or branching vessels, and with the predicted flow information, images for specific MR pulse sequence parameters were generated. Simulations of steady flow in a carotid bifurcation and carotid siphon geometries as imaged by a standard, flow-compensated, spoiled gradient echo sequence, illustrated the major features seen in clinical TOF MRA studies. The combined MRA and CFD study provided insight into a number of artifacts encountered in MRA such as displacement artifacts, signal pile-up, truncation artifacts, and intravoxel phase dispersion. In their subsequent work [161], magnetization variations at a fixed point were determined in the MRA simulations, hence removing the need for streamline tracking in order to calculate the distribution of magnetization, This method inherently accounts for uniform particle density, avoids problems associated with tracking particles close to the wall, and is well-suited to modelling pulsatile flows.

Siegel *et al* [162] developed a computational simulator based on CFD calculations. It can manipulate the image artifacts that would be caused by a convergent geometry in 2D TOF MR angiography. Simulated images were compared with actual phantom images and the artifacts were highly correlated. The computer simulation was then used to test the effects of different orders of motion compensation and of fewer pixels per diameter, as would be present in MR angiograms of small arteries. CFD calculations of turbulent flow were also used in their simulator to study the amount of signal loss caused by random turbulence [163]. Images obtained by the model compared well with the actual MR images of flow in stenoses. By selectively removing the random turbulent motion in the simulation[2], this study revealed that random phase dispersion is the dominant mechanism of signal loss, while phase misregistration and mean flow phase dispersion act as secondary effects.

---

[2]In an analogous engineering situation involving 'low' turbulance, Ciofalo et al [164] obtained completive CFD predictions assuming, laminar, high or low turbulence models, and large eddy simulations

Steinman et al [165] investigated steady flows in an end-to-side anastomosis model using a combined MRA and CFD approach. By tracking particles (representing spins) through a fluid domain using velocities predicted by CFD calculation, and assuming that spatial and velocity encodings occur at discrete times during the pulse sequence, the separate and combined effects of oblique and acceleration artifacts on PC velocity images were simulated [166]. Recently, the method has been used to study the nature and reduction of plaque-mimicking flow artifacts in black blood MR images of human carotid bifurcations [167].

In all these studies, CFD has been used as a tool to provide quantitative velocity data in the whole flow domain. Most of the geometrical models and velocity boundary conditions used in CFD calculations were simplified to some extent, and the model used in MR measurements was not always the same as that used in the calculation. In other words, the CFD simulation was somewhat independent of the MR measurement. Nevertheless, it played an important role in the interpretation of MR images and in helping to understand the various artifacts encountered in MR imaging.

If CFD simulations are carried out on 'real' human arterial models with *in vivo* measured velocity boundary conditions, the predictions will represent more accurately the flow patterns in arteries. These results, once validated, will give valuable information complementary to MR measurements. The techniques discussed earlier have laid a foundation for combining *in vivo* MR images, image processing and CFD, in order to obtain a complete set of flow data that cannot be acquired by MR measurement alone. Figure 1.1 shows a flow chart of this procedure where CFD simulations are carried out by using the combination of anatomically realistic arterial models generated by MR angiograms, with MR measured velocities as boundary conditions. The aims of the research are not only to improve the MRA technique but, most importantly, to understand the complex flow pattern itself.

Research along those lines has been rather sparse. Foutrakis et al [168] made an attempt to reconstruct 3D geometries of the intracranial arteries using 2D cross-sectional MR angiograms acquired from human subjects. After image processing and 3D reconstruction, the unstructured computational mesh of the intracranial artery was generated, but CFD calculations were not attempted in this study. We embarked on this approach of research a number of years ago (with primary application to bifurcations) [169, 18, 170] and have so far successfully incorporated realistic arterial geometries into CFD simulations. The image processing and 3D reconstruction methods were published in 1996 [171], and structured grid generation of a human abdominal bifurcation in 1998 [125, 172]. The generation of velocity boundary conditions was discussed in 1997 [173], and preliminary CFD predictions in 1997 [174].

2.5.2 Problems outstanding

This overall area of research comprises the fields of MRA, image processing, CFD and flow visualisation. There exist errors and uncertainties within each step of the operation. We now give a brief discussion of the possible sources of errors and their likely effects on the final predictions.

Errors in MR imaging

Because MR imaging is the starting point of the whole procedure, errors occurring at this stage will be carried all the way through to the final results. Moreover, MR images provide the raw data for the study, so errors are very difficult to identify and correct in the following steps. Fortunately, state-of-the-art MRA techniques are now able to provide very accurate and reliable angiograms for most of the arteries. However, in regions where flows are complex, such as the internal carotid bulb, signal loss remains as a big hurdle for acquiring an accurate angiogram. In this case, a contrast agent is currently used to improve the image quality.

Errors in 3D reconstruction

While a good set of 2D angiograms are necessary for construction of an accurate geometry, errors may still be generated in the image segmentation and 3D interpolation steps. Al-

though it is reasonably easy to monitor the uncertainties in 2D image segmentations, the accuracy evaluation of 3D reconstruction is very difficult due to lack of techniques in describing mathematically arbitrary, non-planar 3D geometries. Some efforts have been made in this aspect [125, 172], which will be pursued in detail in the future. When processing MR velocity images, the main errors come from shortcomings in 2D image segmentation and image misregistration. A brief discussion of this can be found in [173].

Errors in CFD simulation

In order to assess the physiological validity of the CFD model, careful validations should be undertaken. Errors in CFD simulations may originate from a number of sources, including the mesh and boundary conditions. To guarantee the predictions are grid and time step independent, grid refinement and time step refinement tests are usually carried out for each study. For validation purposes, CFD predictions should be compared with analytical or experimental results for the same model. Since there is no analytical solution available for pulsatile blood flow in bifurcation geometries, comparisons are made either with *in vitro* laboratory data or with limited *in vivo* measurement acquired in regions away from the junction.

2.6 Conclusion

By making use of the latest developments in CFD, combined with *in vivo* MRI data for the geometry and velocity boundary conditions, the study of haemodynamics in human cardiac and arterial systems becomes a new application field for both CFD and MRI. Preliminary results have shown that this strategy can provide more comprehensive flow patterns in the human abdominal bifurcation compared with MRI measurement alone [174]. To perform this task, the first step is to acquire high quality MR anatomical and velocity images. Recent developments in MR techniques allow very fast scans of the cardiac system to be performed, improving significantly the quality of ventricular imaging. The key issue in undertaking this synthesis of research methods lies in generating a good quality mesh, which is able to de-

scribe the vessel or ventricle geometry accurately. Many algorithms have been developed to construct the geometrical model, for which either structured or unstructured meshes can be generated depending upon the problem and the equation solver. Although both the geometry and flow are of complex nature in the human cardiac system, the methods discussed here should in principle be applicable to ventricular flow problems also.

Chapter 3

Data Generation 1: Anatomically realistic model generation

One of the most important steps of CFD simulation on 'real' human arterial models is the anatomically realistic model generation. In the study, the available measurement data are series parallel angiograms which give 3D information of human arteries. Generally, 3D geometry reconstruction is performed first by processing a series of 2D images, and then generating either surface patches which describe the *boundary* of the object or a volume which describes the *structure* of the object. These latter are known as surface and volume rendering respectively. Many methods have been developed to reconstruct 3D geometries. Boissonnat [175] used the volume rendering method to generate a 3D structure from serial planar contours, while Chen et al [105] applied the surface rendering approach to generate the geometry of the bladder. Cohen and Cohen [109] developed a balloon model for recreation of 3D active surfaces from MR images, and the Marching Cubes algorithm was employed by Lorensen and Cline [119]. Although these approaches are capable of generating high quality 3D images, they are complicated and have difficulties to guarantee a satisfactory result if the 2D images are of poor quality. In this thesis, a novel 3D geometrical reconstruction method is proposed.

The method is robust and able to produce both a reliable 3D structure and a smooth surface of an arterial vessel. The resultant 3D data set has been organised in a format that allows for automatic numerical grid generation to be performed, which is essential for subsequent CFD studies.

The generation of a 3D structure from an angiogram generally involves the following steps: 1) the acquisition of 2D cross-sectional images, 2) the definition of 2D contours by image processing, 3) 3D reconstruction, and 4) the visualisation of the 3D structure. In our approach an extra step 5) was carried out to reorganize the 3D data set for numerical grid generation.

3.1   2D angiogram acquisition

As described in chapter 2, many MR angiography techniques are available to obtain human angiograms, such as 2D Time-of-flight (TOF), 3D TOF and 3D Phase-contrast (PC). For the cases concerned in this study, the following points should be noticed:

- The scan region should be sufficiently long to cover the bifurcation of interest.

- Signal loss may occur due to complex flow in vicinity of bifurcation region.

- Subject movement during the scan session may introduce error in 3D reconstruction.

- A high spatial resolution is required to obtain the details of bifurcation.

Generally, 3D techniques such as 3D TOF and 3D PC are able to offer high spatial resolution and less signal loss in complex flow regions. However, the slab (see section 2.2.1.2) of 3D TOF is normally smaller than required. Although the Multiple Overlapping Thin-slab Acquisition (MOTSA) technique can solve this problem, it is not available in the scanner we used. The other problem with 3D TOF is that the signal intensity is dependent on the distance to the scan centre plane which will cause difficulty in image processing. 3D PC is also affected by subject movement. Its long scan time (30 minutes for one session) is too much for the present

research.

2D TOF, on the other hand, is able to scan a long vessel, and the image signal intensity is independent of the scan section location. Although subject movement may cause errors in the cross-sectional images, these errors can be adjusted during 3D reconstruction. The main problem is signal loss in the bifurcation region, especially in the carotid bifurcation bulb. Contrast agent was used for carotid 2D TOF MRA to enhance signals in the bulb region.

In this study, the imaging was performed with a 1.5T scanner (Signa, GE medical systems), using a 2D TOF gradient echo sequence (TR 45 ms, TE 8.7ms, Flip Angle 60, NEX=1) and contiguous 1.5mm slices with an in-plane resolution of 1.41mm for abdominal-iliac (A-L) bifurcation FOV−32cm . The scan covered the region from 10cm proximal to the abdominal bifurcation to 15cm distal to the bifurcation. For carotid bifurcation scans, a 5 inch coil was used to obtain a high ratio of signal to noise (RSN) and contrast-agent Gd-DTPA was used to enhance signals. FOV was 12cm which gave an in-plane resolution of 0.47mm and covered 50mm proximal and 46mm distal to the carotid bifurcation.

These images were transferred for storage and manipulation via a local network using XFER (GE Medical Systems), the data transfer program, from the scanner's computer to a Sun workstation. Figure 2.3 shows a typical result of conventional MRA. The high signal regions are flow lumen. The arterial vessel can be picked out from this high signal area which is called the Region Of Interest (ROI).

3.2   2D MR image preprocessing

Once the parallel images became available at the workstation, preprocessing steps were performed. As it was very desirable to avoid loss of details of the images near the bifurcation region, image preprocessing should be undertaken very carefully in order to obtain a clear and

continuous edge of the vessel. It can be found that 2D TOF images normally have very high contrast between the flow particles and background, making the edge detection easier. The concern here is the signal loss inside ROI (vessel) even after several smoothing steps. Median filter may help, in some cases, smoothing steps are still necessary. In the image preprocessing protocol, a 3 × 3 (or 5 × 5) median filter was used in the first step. The smoothing filters were chosen according to the image quality. Small kernel Gaussian filter was used to smooth the images if there were several signal loss zones in the ROI.

3.3   2D image segmentation procedure

The aim of 2D segmentation is to produce high quality contours of the arterial vessels from 2D MR angiogram for the use of 3D reconstruction. It is one of the most important steps in 3D angiogram generation. There are a number of segmentation techniques available in image processing (see section 2.3.2.1). With regard to the problem considered here, because arterial vessels normally have a smooth internal-surface, the segmentation method needs to consider not only image intensity distribution but also the smoothness of the contour. One of the most suitable methods is the active contour model (or *snake* model), which considers a deformable contour as possessing internal energy in order to impart smoothness to the contour. When this contour is acted on by an external energy field, the contour seeks equilibrium at a local minimum of the field by moving and changing shape in a 'snakelike' manner. The external energy field provides a flexible mechanism to incorporate information about the boundary to be extracted. Such a snake model was employed here to form the main part for the 2D segmentation procedure.

The 2D image segmentation procedure contains two parts. Firstly, an automatic threshold finding program is used to find threshold values, which can roughly separate vessels from the background, for each image. An output file is generated which contains image name and threshold values for each image. Secondly, the file is read by a *snake* model and segmentation

for each image takes place. Contour images are saved for visualizing the segmenting results. B-splines of the vessel contour (200 points forming a closed contour) are also generated for each image for the use of 3D reconstruction. These two parts are described in detail below.

3.3.1 Automatic threshold value finding algorithm

Histogram is the most popular tool to find a threshold automatically. However, in our research, ROI is much smaller than the whole black background as shown in Figure 2.3. Although signal intensities within the ROI are higher than the background, the number of pixels within the ROI is very small compared with that in the background which has lower signal intensities. Global histogram cannot provide optimized threshold values.

The analysis of 2D MR angiogram pixel intensity distribution shows:

- Pixels always have positive values in the image.

- Pixels within the ROI have higher values than in the surrounding area.

- Within the ROI, higher pixel values happen in regions where particles have high velocity and lower pixel values happen at boundary area.

Therefore, if we set a small value of threshold t_0, put a seed point in vessel area which has a pixel value higher than t_0. A region growth algorithm was used to segment the connecting region area A_{vessel} where pixel values are higher than t_0 and evaluate the number of pixels inside the region called A_{vessel}. By the increasing of threshold value $t_i = t_{i-1} + \Delta t$, the value of A_{vessel} will decrease, here 'i' is the iteration counter, and recording the changing of A_{vessel} as ΔA. If $\Delta A = A_{vessel}^{(i-1)} - A_{vessel}^{(i)}$ then $\Delta A > 0$.

It is assumed that the ROI is separated from the background while ΔA has a maximum value, and the t value will be the final threshold value t_n. If the surrounding area of ROI has a uniform lower pixel value, the assumption will be true. However, if there are other vessels near (or

connected) to the ROI, the program will stop at a wrong threshold value. In practice, a reference area value A_0 is chosen, which should roughly equal the area of the ROI, and the program only stops when the Max(ΔA) is reached when $(A_0 - 10\% \times A_0) < A_{vessel} < (A_0 + 10\% \times A_0)$. In the algorithm, seed point location, reference cross-sectional area A_0, starting threshold t_0 as well as a series of image names were read by the program to start the searching of threshold value for each image.

Since for considering the cross-sectional area is reasonably constant in arterial vessel segments (except in the bifurcation region), the program works very well with a fixed A_0. For a tapered vessel, the treatment can be separated into several segments with a different A_0 for each segment. However, it would be difficult to treat a series of images when A_{vessel} varies significantly from image to image, as in the internal carotid bulb region. Fortunately, only very few images have the problem and threshold values can be chosen manually in this case.

3.3.2 The *snake* model used in the study

The second step in the procedure is the running *snake* model to obtain contour splines for each image. The model used here includes a number of control points connected by a series of B-splines. The energy definitions are:

$$\mathbf{E} = E_{inter} + E_{exter} \tag{3.1}$$

where E_{inter} is the internal energy and E_{exter} is the external energy. A higher value of E_{inter} tends to smooth the contour and a higher value of E_{exter} allows the contour to be attracted more easily towards the edge of the vessel. Therefore the ratio of these two terms reflects the smoothness/closeness of the contour. For the external energy:

$$E_{exter} = \int (w_{int}(s)E_{int}(s) + w_{edge}(s)E_{edge}(s))ds \qquad (3.2)$$

where w_{int}, and w_{edge} are the weighting factors for the image intensity energy function E_{int} and the edge energy function E_{edge}, respectively. Their expressions are given by

$$E_{int} = I(x,y) \qquad (3.3)$$

$$E_{edge} = -\;\nabla I\;x,y)^{\,2} = -\;\frac{\partial I(x,y)}{\partial x} + \frac{\partial I(x,y)}{\partial y}^{\,2} \qquad (3.4)$$

$$w_{int}(x,y) = (I(x,y) - t) * w_l \qquad (3.5)$$

$$w_{edge}(x,y) = \frac{w_e}{I(x,y) - t} \qquad (3.6)$$

where t is the threshold value found in the above section. W_l and W_e are constances. The calculation of the weighting factors $w_{ing}(x,y)$, and $w_{edge}(x,y)$ in equations 3.5 and 3.6 contain the item $I(x,y)-t$. If $t = I(x,y)$, then $w_{edge} = \infty$ which will cause trouble in the calculation. In practice, a small constant c_0 will be put in the position of $I(x,y) - t$ in equation 3.6 if $I(x,y) - t = 0$. Minimizing the external energy E_{exter} will attract the contour points to the edge points and the points which have similar values as the threshold. The definition of internal energy item is:

$$E_{inter} = \int (w_{cont}E_{cont}(s) + w_{curv}E_{curv}(s))ds \qquad (3.7)$$

where the energy term E_{cont} denotes the first-order continuity constraint and is given by:

$$E_{cont} = |\bar{d}- \| v_i - v_{i-1} \| | \qquad (3.8)$$

where v_i denotes the coordinates of the ith snaxel[1], $\| v_i - v_{i-1} \|$ denotes the distance between v_i and v_{i-1}, and d denotes the average distance between neighbours. Minimizing

---

[1]here snaxels are the snake points, or control points on the snake.

94

this term forces the snaxels to be uniformly spaced (*continuity*). The second term E_{curv} is

the curvature energy and is defined as

$$E_{curv} = \left| \frac{u_{i+1}}{u_{i+1}} - \frac{u_i}{u_i} \right|^2 \tag{3.9}$$

where $u_i = v_i - v_{i-1}$ and $\frac{u_i}{\|u_i\|}$ is a discreet approximation unit tangent at u_{i-1}. Minimizing

this term will control the smoothness (*curvature*) of the contour during the deformation pro-

cess.

In equations 3.2 and 3.7, '*s*' corresponds to a special location on the contour (or control

point). The integral is performed along the contour. All the energy terms must be scaled

to lie in the same range. It can be achieved by adjusting the ratios among weight constants

$w_l, w_e, w_{cont}, w_{curv}$ and c_0. The ratios normally don't need to be changed in the process. The

adjustment can also influence the smoothness closeness of the final contour as well as the

sensitivity of contour with the changing of threshold value.

To perform the *snake* model, an initial guess of the contour should be provided, for which a

region growing method was used. As the initial contour obtained was enclosed by edge points

one by one (boundary of the region), a down size step was performed to make several pixels

gap ($\bar{d}$) between each control point. The internal and external energy were calculated at each

control point and at the pixels adjacent to the control point along the normal direction of

the contour. The local energy minimum points were chosen as the new control points to be

used in the next iteration. The convergence is monitored by calculating the global energy E,

which should decrease gradually with each iteration. If the distance moved by the control

points is smaller than the given tolerance, the calculation has converged. it was found that

the initial contour calculated using the region growing method was very close to the final

solution, convergence can normally be achieved in less than 10 iterations. Figure 3.1 shows

the procedure of the snake model in the research. Figure 3.1(a) gives the original MRA image,

(b) shows the edge image. Initial guess of the contour is given in Figure 3.1(c) obtained by

a region growing method and the final result of the snake model is shown in Figure 3.1(d).

3.3.3   Accuracy analysis of the 2D segmentation

Because of the arbitrariness of noise distribution in MR image, a quantitative analysis of the 2D segmentation accuracy is very difficult (maybe impossible). However, a clear understanding of the factors which may cause errors and quantities which can be used to monitor the processing accuracy will help to control the overall accuracy.

From the procedure described above, it can be found that 2D segmentation errors may come from a wrong threshold value 't' and the snake model itself. The automatic threshold finding program can make mistakes when a wrong reference cross-sectional area input is used. In the *snake* model algorithm, the threshold value will influence the initial guess of the contour and the weight parameters: w_{int} and w_{edge} (in equations 3.5 and 3.6).

An easy way to the uncertainty of 't' test is to display the original image and find a suitable 't' manually. However, when many images need to be processed, which is the reason to use an automatic threshold finding program, the continuity of the final area of ROI (which corresponds to the final threshold value 't_n') for the serial images can be used to monitor the output. This is because for an arterial segment, cross-sectional areas of adjacent images (in the axial direction) should change smoothly. If the resultant area of ROI for an image is much smaller than others, the threshold value 't_n' must have been overevaluated or underevaluated.

The sensitivity test of the snake model to 't' was carried out by the comparison of contours (obtained from snake model) with different threshold values. In my experience, if the ratios among weight constants w_l, w_e, w_{cont}, w_{curv} and c_0 have been carefully adjusted, the *snake* model is not very sensitive to the threshold value. It can tolerate 10% variations of threshold value and produce similar contours.

The overall performance of the 2D segmentation procedure can be inspected visually by

(a)   (b)

(c)   (d)
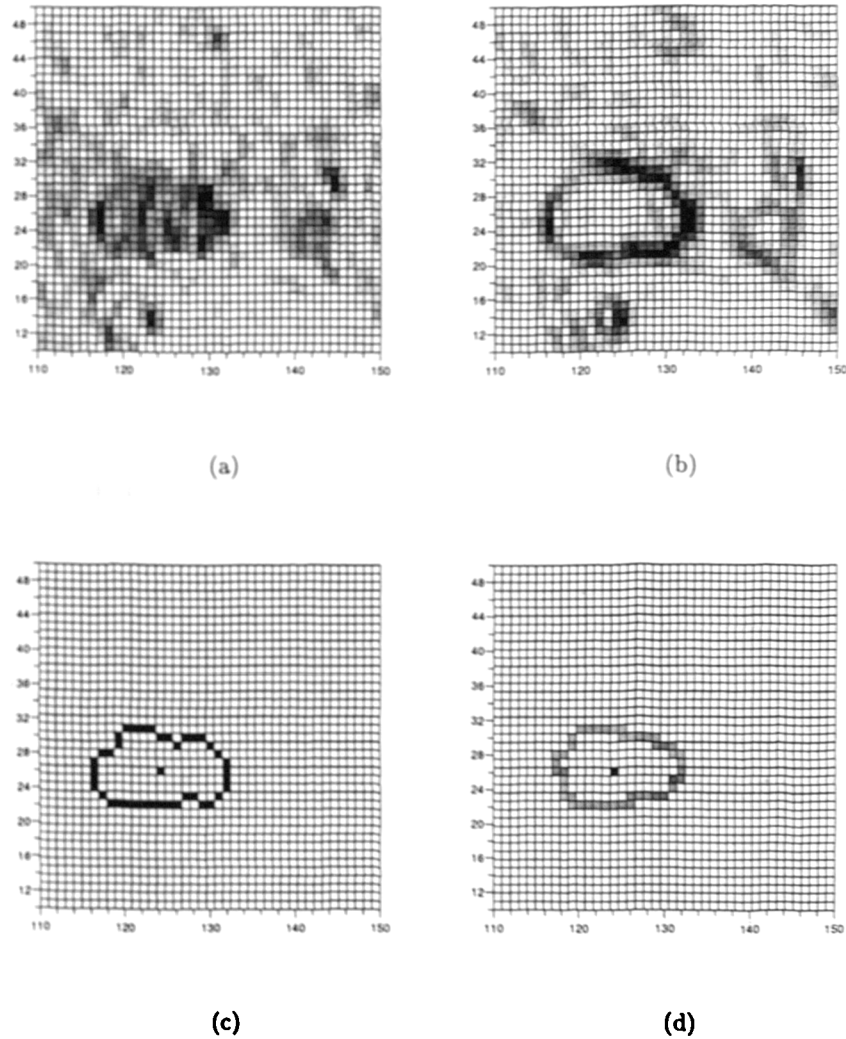
Figure 3.1: 2D cross-sectional image segmentation procedure. Image was acquired from the abdominal aorta of a healthy human subject. High intensity region (black) represents the vessel lumen; (a): original MR 2D TOF image; (b): edge image for (a), obtained by sobel operator; (c): initial guess of the vessel contour; and (d): final segmentation result from the snake model.

(a)   (b)
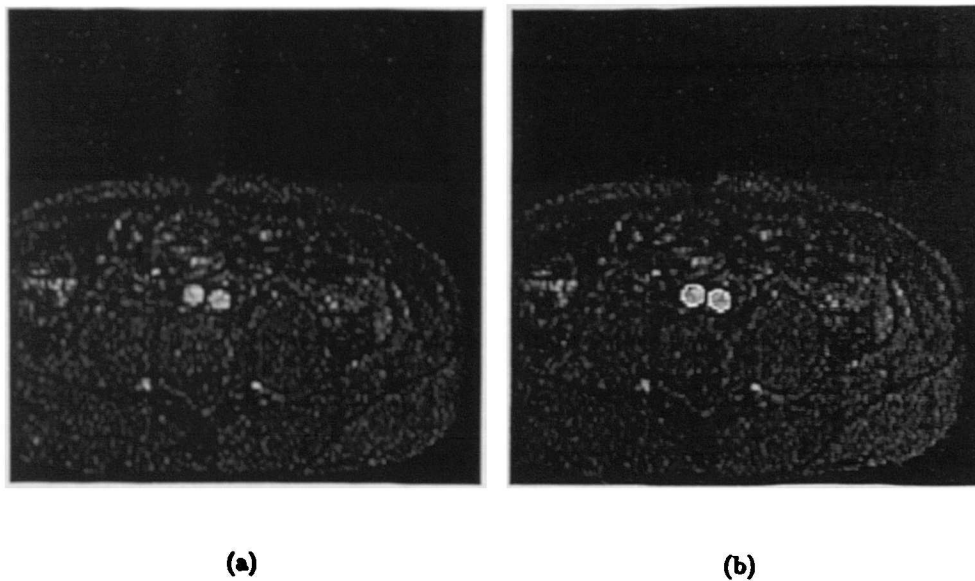
Figure 3.2: 2D MR image in human iliac arteries (3mm inferior the abdominal bifurcation), and the segmentation result by a snake model. (a) Original 2D MR image, and (b) Segmentation result of (a), Contour points are highlighted in the image which can be used to validate the segmentation result.

putting the original image and the resultant contour together (high-light the contour) as displayed in Figure 3.2.

3.4 3D smoothing and reconstruction

3.4.1 3D smoothing

Having assembled the 3D structure by adding coordinates in the axial direction, appropriate smoothing techniques were applied to yield a smooth 3D bifurcation contour image. The first step of the 3D smoothing operation was to achieve smoothness in the axial direction. Because the images were acquired at different times in the 2D TOF MR scan, subject movements are likely to cause errors in 3D reconstruction. A typical image is shown in Figure 3.3 in which the MR registration errors can be found. The axial smoothing is able to correct these errors by:

1. Finding the centre point of each 2D contour image, then forming a centre line in the common and branch vessels;

2. Using mathematical curve fitting methods (here least-squares cubic splines were employed) to smooth the centre lines;

3. Finding new centre point locations for each contour and moving the contours to new positions by matching new centre points.

The second step used in the smoothing sequence involves treating the surface. This is known as *surface smoothing*, which smooths the difference between each contour. Suppose there is an coarse surface of a tube like that in Figure 3.4. Then the algorithm of the surface smoothing may be described by the following operations:

1. Transfer of the coordinate system from Cartesian (x-y-z) to cylindrical (S-T) (here from a *physical* location to a *logical* location);
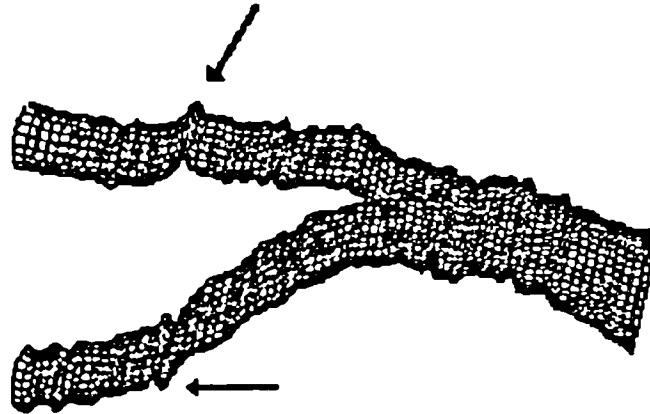
Figure 3.3: A typical 3D contour image showing the errors caused in MR registration
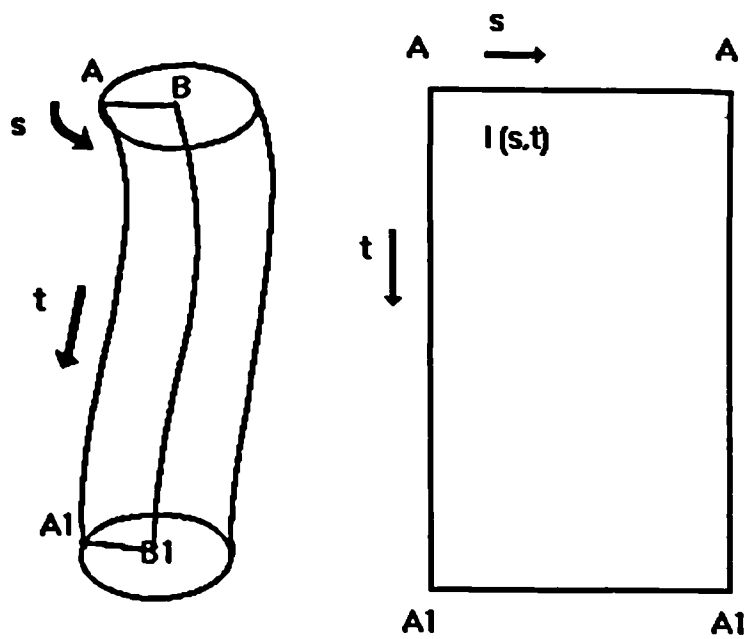
Figure 3.4: Schematic illustration of the surface smoothing algorithm, (a) curved vessel, (b) S-T image.
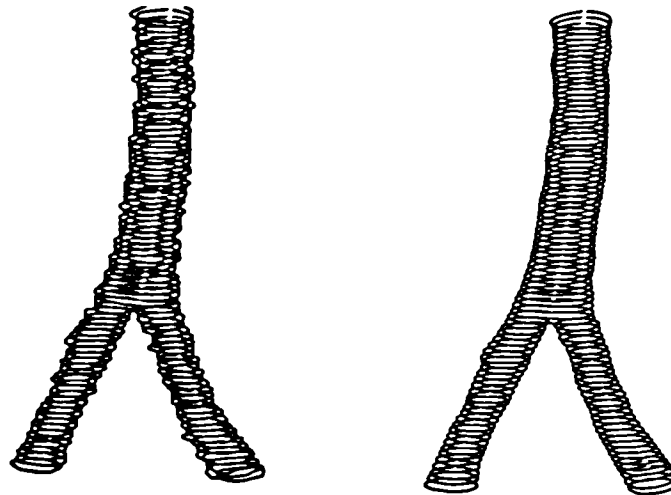
(a) before 3D smoothing   (b) after 3D smoothing

Figure 3.5: 3D contour image of a human abdominal-iliac bifurcation.

2. Generation of the S-T 'image'. Here an 'image pixel' known as (s,t) would correspond to a surface point (x,y,z) and the 'pixel' value I(s,t) denoted the radius of the point (x,y,z) on the tube surface;

3. Smoothing of the S-T 'image' by conventional 2D smoothing methods such as average, or medium filters;

4. Transfer of the coordinate system back from cylindrical (S-T) to Cartesian (x-y-z).

There are some other methods that can be used in 3D image smoothing as described in section 2.3.2.2. However, the method described here actually turns a 3D problem to a 2D calculation. It is very simple but effective. Furthermore, because the smoothing procedure is subdivided into axial smoothing and surface smoothing according to the nature of image acquiring, the process can be easily controlled by changing the smoothness parameter. Figure 3.5 shows a 3D smoothing result.

3.4.2   3D reconstruction

3D model reconstruction can be achieved by two methods as discussed in section 2.3.2. In this study, 2D contours were obtained by 2D TOF MRI scan and processed by the *snake* model. Therefore method one, which is 2D segmentation and 3D reconstruction, is used to generate a 3D model. The general task of 3D reconstruction is to generate one-to-one mapping relationship between points different contours and to construct surface rendering for 3D visualization. Although many algorithms have been developed for the 3D model generation from 2D contours [105, 116, 117, 121], most of them were designed to present the 3D object for visualization purposes. However, in the present study, 3D reconstruction was not only to visualize the geometry, but most importantly, to obtain surface point location information for the generation of a numerical mesh. Moreover, the CFD code (CFX4) requires a structured mesh, hence the surface points have to be organized in a certain structured format.

3.4.2.1   Structure generation

A multi-block grid is one of the most effective ways to generate a structured grid in complex geometrical model. For the bifurcation geometry concerned, the model can be divided into a number of topologically similar parts to build a block structure as shown in Figure 3.6. To build the structure, the bifurcation surface is divided into four patches and the point mapping relationship should follow this requirement.

When describing an abdominal bifurcation, common vessel is superior to the apex and branch vessels are inferior to the apex. The opposite would be true for the carotid bifurcation in which the common vessel is inferior to the apex. To simplify the description, in this chapter, the bifurcation model is positioned as in Figure 3.7 where common vessel is located superior to the apex and has larger z value than branch vessels. Figure 3.7 also illustrates the spatial relationship of points, lines and contours which are used in the following descriptions. The structure generation procedure can be described as:
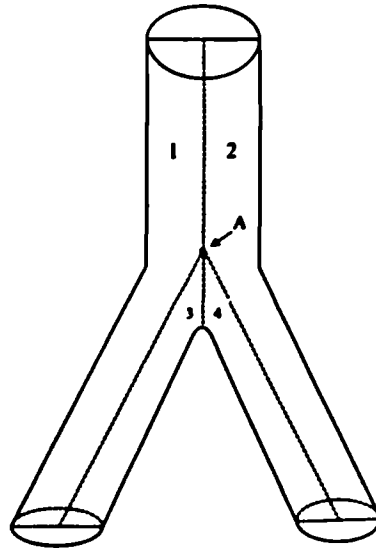
Figure 3.6: Block structure used in the study for the structured grid generation in a bifurcation model.
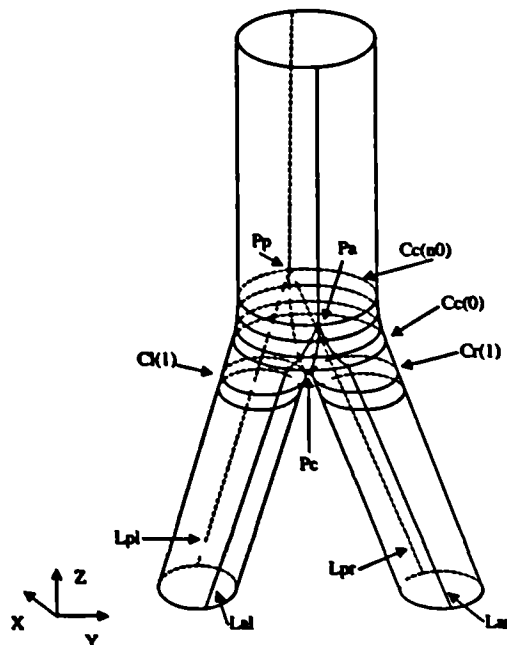
Figure 3.7: Illustration of structure and surface spline mapping points generation in a bifurcation model

1. **Rotate the model:** the 3D volume of the model is rotated by an angle so that the 'bifurcation plane[2]' is parallel to y-axis shown in Figure 3.7 (perpendicular to anterior/posterior direction) for the convenience of following processing.

2. **Generate boundary curves for patches:** projecting the bifurcation centre-lines generated in section 3.4.1, to the anterior surface (L_{al}, L_{ar}) and posterior surface (L_{pl}, L_{pr}) to form four surface curves, named *surface centre-lines*.

3. **Generate the bifurcation divider arc:** The arc, which forms the common boundary for patch C and patch D as shown in Figure 3.6 curve $\widetilde{P_aP_cP_p}$, can be generated by:

   (a) Using two intersection points of the *surface centre-lines* P_a (by L_{al}, L_{ar}) and P_p (by L_{pl}, L_{pr}) and the centre point between $C_l(1), C_r(1)$ [3], the first contours the of two branches, P_c generate a dividing plane.

   (b) Finding the intersection points of the dividing plane and contours ($C_c(n0)$ to C_c n). If $P_{crossA}(i)$ denote the intersection points in the anterior surface, $P_{crossP}(i)$ for the posterior surface, the dividing arc $\widetilde{P_aP_cP_p}$ is generated by interpolating those points in the order of $P_a, P_{crossA}(i), P_c, P_{crossP}(i), P_p$.

After all the boundary curves are obtained, the bifurcation is then divided into four patches A, B, C, D which coverd parts 1, 2, 3, 4 in Figure 3.6 respectively. Patches A and B form the left and right half surface of the common vessel while the left branch was formed by patches A and C and the right branch by patches B and D.

---

[2]The plane is defined parallel to the z-axis and passes through the central points of the first contours in the branch vessels Cl(1) and Cr(1) shown in Figure 3.7

[3]The point $P_c(x, y, z)$ has the same x,y value as the middle point on a line formed by two nearest points on contours Cl(1) and Cr(1), the z value of point $P_c(x, y, z)$ is Cr(1)(z) + 0.75(mm) which is between Cr(1) and Cc(n) if the slice thickness is 1 5mm for the contour

3.4.2.2   Surface spline mapping point generation

The 3D image was constructed by serial parallel 2D contours as shown in Figure 3.5. To generate a grid which is normally defined with a similar orientation as the 2D contours, the surface information should be given in the direction perpendicular to the grid planes.

To construct surface splines in each patch, one-to-one contour point mapping relationships have to be generated first in order to prepare for the interpolation. From the nature of the data organization, contour points throughout the model can be classified into two groups.

All contour points in patches A and B, and points in patches C and D below the first contours of the branch vessel (in Figure 3.7) will form the first part of points. The mapping relationship can be easily generated. For example for points in patch A, firstly, interpolate each contour from anterior boundary L_{al} to posterior boundary L_{pl} to obtain m equal archlength contour points $PA(i,j)$, here i represents the contour number and j is the point position in the contour and $j \subseteq [1,m]$. Then $P(i+1,j)$ will become the next mapping point for $P(i,j)$. The same operation can be done for points on other patches.

The remaining contour points form the second part. Splines produced in this part will form the flow dividing side of the bifurcation. The mapping relation generation is much more complicated. Because the bifurcation is formed by three arterial segments (common vessel, and two branch vessels) from the information we have, there is a 1.5mm gap between the common vessel and the branch vessels. The surface splines here should be able to bridge the gap and reconstruct the inside of the bifurcation.

If there are n contours in the common vessel, $C_c(n)$ presents the last contour in the common vessel, point P_a is at the n_0th contour named $C_c(n_0)$, let $C_l(1)$ and $C_r(1)$ correspond to the first contour for the left and the right branch vessels as shown in Figure 3.7, the reconstruction procedure can be described as (for anterior side):

- Interpolate the dividing arch$P_aP_cP_p$ into $(m-1)$ equal archlength part to obtain m contour points $P0(j)$, $(j = 1, .., m)$.

- For each contour $C_c(i)$ $(i = n_0, n; n_0 < n)$, find out the number of points $P0(j)$ that are located above the contour and save it in a array $Num(i)$, here $i = n_0, n$. It means there are $Num(i)$ splines passing the contour from each side of the arch $P_a\widetilde{P_cP_p}$.

- Subdivide the contour $C_c(i)$ $(i = n_0, n)$ into $(Num(i) + 1)$ parts between the segment from $P_{crossA}(i)$ to the intersection points with L_{al}, and find out $Num(i)$ mapping point locations for the contour on the left side (or patch C) $P1(i, j)$, here $i = n_0, n$ and $j = 1, Num(i)$.

- Repeat the same operation on the right side to find out the mapping points on patch D $P2$ i, j), i and j have the same meaning as above.

- Generate the mapping point relationship from left side (points on $C_l(1)$) $P_L(1, i)$ to left side contour points $P1(i, j)$ then to the point on the arch$P_a\widetilde{P_cP_p}$ $P0(i)$, then to the right side contour mapping points $P2(i, j)$, eventually to the points on $C_r(1)$, $P_R(1, i)$, here $i = 1, ..., m$. For the spline which has a top point $P0(i)$ located lower than $Cc(n)$, mapping point will jump from $P_L(1, i)$ to $P0(i)$ then to $P_R(1, i)$ directly.

It is noted that different splines may have different numbers of mapping points. The reason for connecting mapping points from patch C to patch D together at $P_a\widetilde{P_cP_p}$ is to generate a smoother shape at the bifurcation dividing region. The shape and smoothness of $P_a\widetilde{P_cP_p}$ can be controlled by the interpolation procedures described in the next section.

3.4.2.3 Surface splines interpolation

After the preparation of data file for each spline (generating the mapping points), surface interpolations are undertaken to generate the surface numerically from the measured surface points (here is 3D contours). Among the various interpolation methods, those based on cubic

splines tend to be best for treating existing surfaces when it is important to preserve the original data points, because these approaches usually guarantee that the resulting surface will pass through the data. However, when the data are sparse, the region between data points may depart unacceptably from the measured surface. B-splines and nonuniform rational B-splines (NURBS) can be used to approximate an existing surface. They may not preserve the original points, but in general produce a smoother surface than classical cubic spline methods.

The surface generation algorithm used in the study is based on *least-squares cubic splines* [176] as used in central lines smoothing. The interpolation fits cubics splines to arbitrary data points with arbitrary weights but itself chooses the number and positions of the knots, the user only having to supply a threshold for the sum of squares of residuals. There are 40 (this number may vary) cubic splines around each vessel. The surface grid can then be generated by cutting those splines at chosen planes.

Figure 3.8 shows an example of the B-splines for the abdominal bifurcation. There are 21 splines in each patch forming half of the vessels, here named spline group. Groups one and two form the parts 1 and 2 (in Figure 3.6) respectively, being divided into two parts at point A to form the outside circle of the branches. There are 900 equal arc length points in each spline in these two groups. Spline groups three and four form the inside circle of the branch vessels (patches C and D) and meet at the bifurcation region with 500 equal arc length points on each spline.

3.5 Structured numerical grid generation

3.5.1 Grid generation

To generate a numerical grid in an arbitrary 3D model, a very important step is to find the surface grid points which can define the 3D model shape completely. The generation of a grid on a general surface is a 2D grid problem on its own, which can be done either by inter-
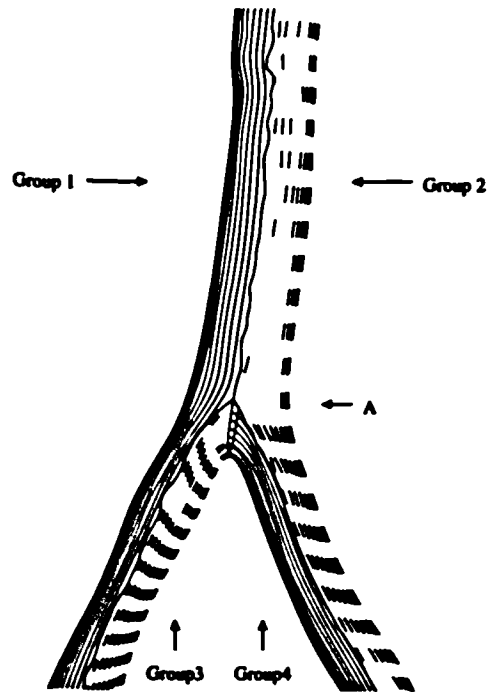
Figure 3.8: An example of the B-splines for the abdominal bifurcation. The splines are divided into four groups.

polation or by solving a set of partial differential equations. In general, it is a 2D boundary value problem on a curved surface, that is, the determination of the locations of points on the surface from a specified distributions of points on the four edges of the surface.

With the surface splines, the grid can be generated in the bifurcation model in three steps. Grid distribution along the axial, circumferential and radial directions is defined by steps one, two and three respectively.

The first step is to specify a grid distribution along the axial direction in each patch. Non-uniform cubic spline interpolations were used along three chosen surface splines in the group to obtain grid distribution along the axial direction in the spline groups described in Figure 3.8. For spline group one, the first and third splines are obtained from L_{al}, L_{pl} (named as S_{al}, S_{pl}) respectively, and the second one is the middle spline in the group (11th spline if there are 21 splines for each group), which represent the most outside spline (to the left for group
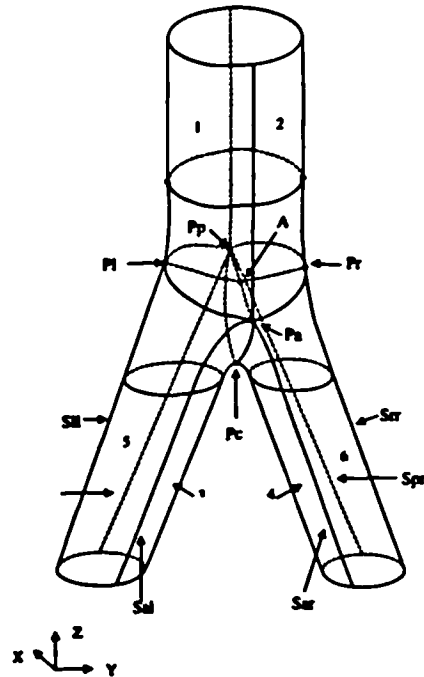
Figure 3.9: Illustration of splines in structured mech generation for a bifurcation model.

one). With the location of interpolated grid points on these three splines, grid planes are determined by the correspondent point on each of three splines at each level. The same operation is undertaken for spline groups two, three and four. The common boundary of two patches will share the same data file. In order to generate non-uniform grid distribution, a power law was used in the algorithm which can be described as:

- The spline S_{ll} and S_{rr} in groups one and two were divided into two segments at point P_l and P_r as shown in Figure 3.9 by a criteria that the point has the shortest distance from point A to the spline. The splines S_{al}, S_{ar}, S_{pl}, and S_{pr} were also divided into two parts at points P_a, and P_p respectively. These operations actually separated the bifurcation into six topologically similar parts which would eventually form the blocks for the model. This final block structure divided parts 1 and 2 (shown in Figure 3.6) into blocks 1, 5 and 2, 6 respectively (shown in Figure 3.9).

- For each segment of spline, if L is the arc length of the spline segment, $S(i)$ represents the distance from the grid points P_i to P_{i-1} on the same spline and the starting point P_1 is the middle point (point P_l for the spline S_{ll}), therefore $S(1) = 0$

$$d_0 = \frac{L}{\sum_{j=1}^{n}(b)^j} \tag{3.10}$$

$$S(i+1) = S(i) + d_0 \times (b)^{i-1} \tag{3.11}$$

where n is the number of grid point along the axial direction in the block, and b is the power parameter. If $b = 1$, a uniform grid distribution will be generated and the distance between each grid point is $\frac{L}{n+1}$. Non-uniform grid distributions can be obtained when $b \neq 1$, while high density grid can be created in the bifurcation region if $b > 1$.

The second step of grid generation is to define grid planes and calculate boundary points on the model surface. With the location of grid points on the splines, the grid planes are then defined by choosing corresponding points on the splines for each block, here three points were used to define a grid plane. The intersection point of the plane with each spline in the block will form the boundary of the grid plane and a cubic spline will be generated to obtain the grid distribution along the plane boundary (or circular direction) by the criteria that the circular angle between each grid point remains constant. Together with the grid distribution along the axial direction, the surface grid is completely defined. Figure 3.10(b) gives an example of the surface grid for a human abdominal-iliac bifurcation.

The third step is to interpolate grid points within the boundary on each grid plane. The interpolation from surface grid to the internal volume of the model was carried out on each grid plane. The strategy is similar to that used in step one, i.e. to generate a non-uniform grid distribution along the radial direction on each grid plane, producing denser grid near the wall and coarse grid in the centre region as shown in Figure 3.10(c).
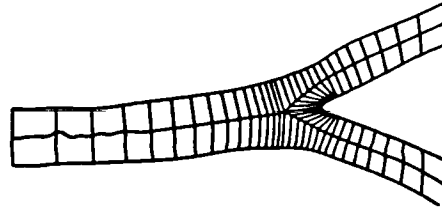
(a)
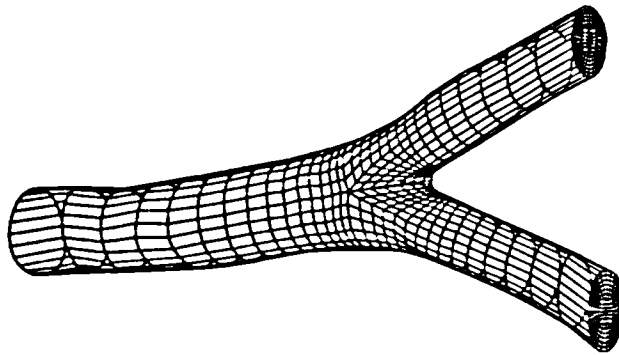
(b)
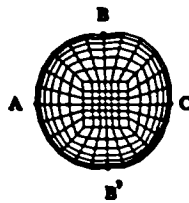
(c)

Figure 3.10: Illustration of grid generation. (a): Block structure description; (b) surface grid

3D plot of a human abdominal bifurcation; and (c): grid distribution at a grid plane;

3.5.2 Grid quality evaluation

Post-processing of grid generation usually includes two steps: grid smoothing and grid quality evaluation. The grid can be evaluated qualitatively and, to some extent, quantitatively, by the examination of certain computable properties. These properties are related to grid quality in that they are directly or indirectly linked to local truncation error or algorithm convergence. Following Kerlick and Klopfer [177], and Gatlin [178], the grid quality measures considered in the recent work of Luong [179] are *skew angle, aspect ratio, grid Laplacian,* and *spacing arc length.* For a 3D problem, four values can be calculated for each property at each grid point. The definitions of the parameters can be found in their paper [179].

The definitions of grid quantities in this study were the same as used in the structured grid generation package SOPHIA (a pre-processor of CFX4.0). While they can describe the grid quality from different aspects, the smoothness of the grid cannot be found from those quantities. If the error caused by grid roughness needs to be taken into account, grid quantities such as *grid Laplacian* should be introduced in the program. The program also outputs the locations of the worst cells or vertices.

The quality of the grid was evaluated *quantitatively* by calculating:

1. four quantities which are cell based. They are:

   - Volume: The volume of each cell,

   - Skew: Ratio of the shortest cell diagonal over the longest cell diagonal,

   - Twist: Cosine of the largest angle between diagonally opposite edges of a cell, and

   - Taper: The minimum of the ratio of the smallest face over the largest face in a pair of opposite faces.

2. two quantities which are vertex based:

   - Orthogonality: The maximum angular deviation from 90 degrees of any pair of 'adjacent' edges meeting at the vertex, and

- The ratio of the minimum volume over the maximum volume of any cells having the point as a vertex. [180]

A typical grid quantity results is shown in Figure 3.11 for an abdominal aortic bifurcation.

3.6 3D structure and grid visualization

Because of the geometrical complexity of a 3D arbitrary object such as arterial bifurcation, 3D plotting of the intermediate results at each stage of procedure is necessary. Although it is a programming problem, a good interface will help considably in understanding data flow step by step. There are several ways to present graphic results in on-line applications. A straightforward method is by calling "Graphic Subroutines" to form a graphic part. With different combinations of subroutines, it is able to make complex plotting. However, it is not easy to control the plot parameters such as rotating, moving as well as zooming. *Uniras* fortran subroutines were used at the early stage of this study to show 3D structures.

Because of the above disadvantages, a more sophisticated way is used now by calling ('system call') a small graphic package in the program ('plotmtv' from public domain of internet). This method can offer a good Graphic User Interface (GUI) and the plotting parameters can be easily controlled. With this technique, intermediate results of 3D data processing can be easily viewed and examined. Many figures in the thesis were produced this way.

In this study, the individual function programs (such as structure reconstruction and grid generation programs) are still separated from the Graphic program, most of the operating parameters still have to be input by the operator line by line. The ideal solution would be to generate a fully user friendly interface by putting all applications in a graphic environment. To achieve this, a graphical development platform is necessary and more programming work needs to be done.

	MIN	MAX	AVERAGE	STD
VOLUME	0 3767 E 9	12181E 7	263 E 8	2 4 E 8
SKEW	0 278 E+ 0	0 99582E+00	0 8 96E+	13899E+ 1
TWIST	0 83138E+ 0	0 99996E+00	96824E+	157 E 1
TAPER	0 63 31E+ 0	0 99746E+	0 8 646E+	69 53E 1
STRETCH	0 1976 E+ 0	0 99969E+00	0 75316E+	12632E+
ORTHOGONALITY	0 10 E+01	0 626E+02	198E+ 2	121E+ 2

	0.0 .1	.1 .2	.2 3	.3 4	5 6	6 7	7 8	8 9	9 1
SKEW	0	0	4	141	218	41	4	1745	4539
TWIST	0	0	0	0	0	1 3	1572	9	8 91
TAPER	0	4	0	0	256	1450	274	4363	2 62
STRETCH	0		37	85				2887	774

	80. 90.	70. 80.	60. 70.	60. 70.	5 . 6	40. 5 .	3 . 4 .	20. 3	1 . 2 .	1
ORTHOGONALITY	0	0	8	308	521	750	1787	3844	1732	
BAD										GOOD

Figure 3.11: A typical set of grid quantity results for an abdominal bifurcation model

114

3.7 Accuracy analysis of the geometrical model reconstruction

All numerical approximation procedures are subject to errors. The ultimate goal of this study is to obtain a 3D configuration that is both physiologically realistic (that is to retain as much as possible the original features of the vessels), and mathematically smooth. From the preceding discussion, it is clear that numerical errors may come from two sources: (1) 2D image segmentation, and (2) 3D smoothing.

The 2D cross-sectional images are processed by using the well-known *active contour model* (or *snake model*). Since the final contour is determined by the image pixel intensity, as well as the shape of the contour, some uncertainties could be introduced. The quality of the resulting contour is monitored by highlighting the contour points in the original image as shown in Figure ??(b), so that the best fitted contour can be selected.

The accuracy of the 3D smoothing procedure needs to be assessed from two aspects: axial and surface interpolations. The interpolation algorithm employed here is *"Least-square cubic splines"* [176]. The algorithm fits cubic splines to arbitrary data points with arbitrary weights but itself chooses the number and positions of the control knots. The user needs only to supply a threshold for the *sum of squares of residuals "S"*, with which the smoothness/closeness fitting ratio can be easily controlled. When S=0 the spline becomes a cubic spline with non-error interpolation at measured points. However, in practice a small non-zero S value is chosen to obtain a reasonably smooth curve. Two numerical experiments have been carried out to study the effect of S on the accuracy of the axial and surface interpolation steps, respectively.

- The axial interpolation scheme was assessed by comparing the 3D vessel centrelines of the bifurcation obtained with different "s" values. Figure 3.12(a) gives a comparison of the vessel centrelines before and after smoothing. In this case it is found that when

(a)

(b)
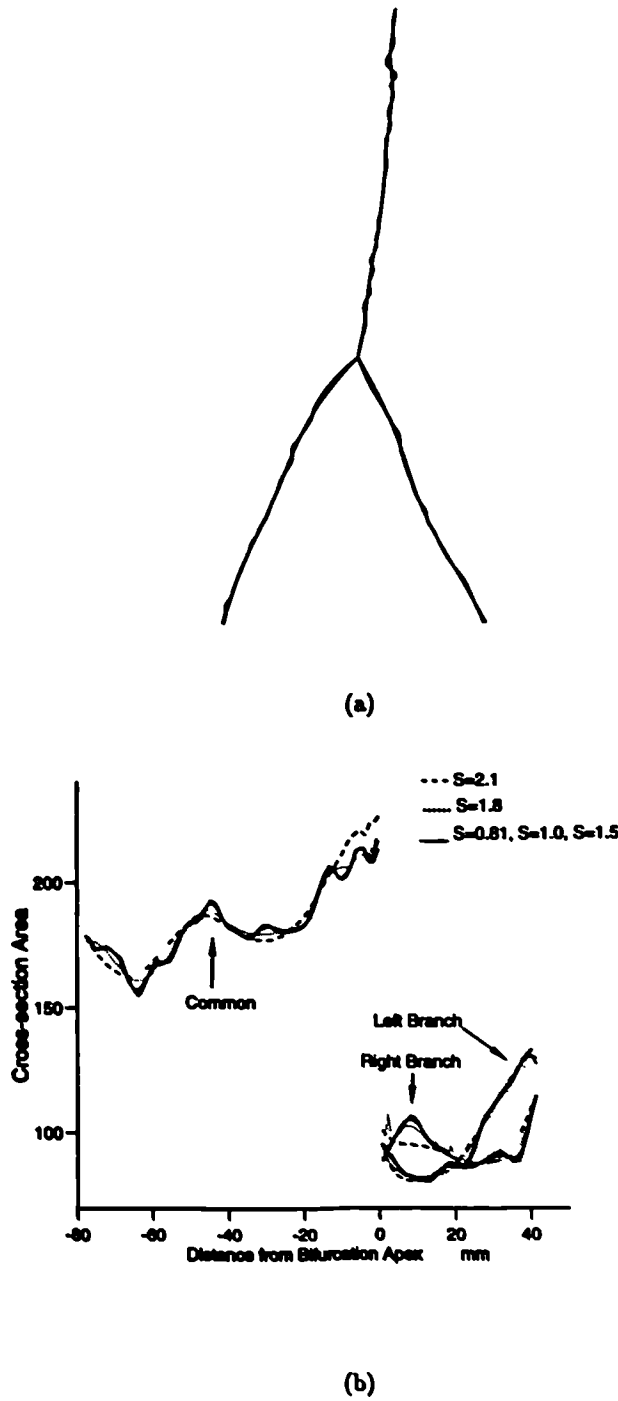
Figure 3.12: Uncertainty test for the 3D smoothing algorithm. (a): Comparison of the vessel centrelines before and after smoothing; (b): cross-sectional area curves for different S values.

$s < 1.5$, the smoothed centrelines show little difference from the original lines. The smoothed centrelines given in the figure were obtained with s=1.9, which appeared to be the most suitable value for the bifurcation geometry studied.

- The surface interpolation scheme was assessed by comparing the cross-sectional areas of the 3D vessel along its axial direction for different "S" values[4]. Figure 3.12b shows the results for S values ranging from 0.8 to 2.1, and the area curve based on the original contour. Results for S from 0.8 to 1.5 are found to be very close to each other, indicating that most of the changes of area agree well with the original contour. However, for $S < 1.5$, the smoothness is not satisfactory. For "S" = 1.8 or 2.1, more errors are introduced. In other words, S=1.5 seems to be the optimum value for this case.

It should be noticed that the comparison discussed above only gives an integral result of contour change by calculating the cross-sectional area. It does not tell local changes in the surface especially uncertainties involved in the reconstruction of the bifurcation dividing surface carried out in section(3.4.2.2). Further quantifying parameters need to be evaluated for the specified accuracy requirements. For example, distances from point A to grid points on the bifurcation arc are able to give information on the bifurcation dividing surface reconstruction.

---

[4]This "S" is for surface interpolation which is independent of the "s" used in axial interpolation.

Chapter 4

Data generation 2:

Velocity boundary condition

generation

The numerical grid generated above is able to represent the complicated geometry of a human arterial bifurcation allowing numerical simulation of blood flow in the model to be performed. However, CFD simulations need not only the numerical mesh in the flow domain but also dynamical boundary conditions which can be variously velocity distribution in the boundary planes, mass flow rate in and/or out of the boundary planes and the pressure distribution in the boundary planes. Very few non-invasive techniques can be used to measure velocity distribution clinically. In this study, the Cine MR phase-contrast (PC) technique was applied to acquire 3D velocity distributions at chosen planes in the arteries of interest.

4.1   MR velocity image acquisition

The MRA techniques have been used in clinical routines to obtain vessel structure information for patients. In principle some quantitative information can also be obtained by these techniques and this has been recognized for decades. Numerous approaches have been proposed

that depend on either time-of-flight or phase contrast effects. Phase contrast MR methods are

based on the principle that the transverse magnetization of spins moving in the presence of a

magnetic field gradient develops a velocity-proportional phase shift relative to static spins as

described in section(2.2.2). The cine Phase Contrast Imaging Technique was developed on

this principle and is being used increasingly to analyse vascular systems noninvasively. This

technique is promising for both anatomical display and quantitative haemodynamic evalua-

tion of various arterial and venous vessels.

In the study, MR images were acquired by a MR whole body scannar (Signa 1.5 T, GE)

with a conventional cine MR PC sequence. The scan parameters are: TR: 33ms, TE: 6.1ms,

Flip angle: 20 , Slice thickness: 5mm, Matrix 256x128, NEX: 2, Flow Encoding 100 cm/sec

and FOV = 20 cm for the human abdominal-iliac bifurcation and 12 cm for the carotid

bifurcation. ECG gating was used to acquire 16 velocity images with equal time intervals

between each other in one cardiac cycle. To obtain three components of velocity at the scan

planes, three separate scans were performed with velocity encoding in Superior Inferior, An-

terior Posterior and Left Right directions respectively. Because of the small velocity value in

A P and L R directions (or components), flow encoding was set to be 50 cm sec for the scans.

4.2 MR velocity image segmentation

Figure 4.1(a) shows an example of the cine PC phase image acquired in the abdominal aorta.

The aim of the image processing is to segment the image and pick out the vessel which forms

the region of interest (ROI). Because the pixel intensity inside the ROI is proportional to

the velocity value at the pixel, any large deviations of pixel intensity from its original value

inside ROI should be avoided during image processing. From the sample tested it was found

that the image had very high random noise and the ratio of signal to noise (RSN) was very

low. In some cases, at low flow phases in the cardiac cycle, signals are covered by noise. In

these cases, the lumen edge cannot be determined satisfactorily. However, the cine PC tech-

nique offers spin magnitude image at the same time as the phase image. A pair of phase and magnitude images is shown in Figure 4.1(b), the latter has high RSN. Although it does not give quantitative velocity information, the magnitude image defines the accurate geometry of the vessel and this information can be used in phase image segmentation.

4.2.1   2D Cine PC magnitude image segmentation

In the study, the segmentation algorithm for 2D TOF image (described in section 3.3) was used directly to process the PC magnitude image. In most cases, the magnitude image has a very good quality and a clear boundary for the arterial vessel. However, in some cases, even if the RSN is high, because veins are close to the arteries, it is very difficult to separate angiogram from the similar signal intensity veinogram background. In this case, manual segmentation is necessary.

Several factors need to be considered when an image is segmented manually. These include

(a)   (b)
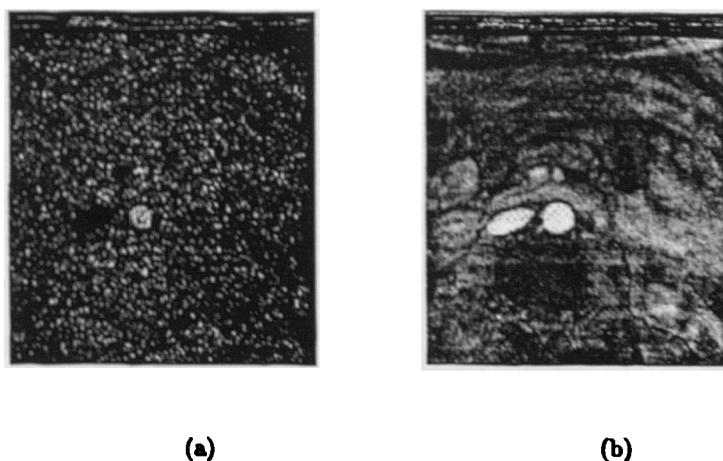
Figure 4.1: Sample images of the Cine PC scan: (a) phase (velocity) image; and (b) magnitude image.

relative phase image, images in nearby time points, and images at the same time point but different scans (or velocity components). Considering 16 time points in one cardiac cycle, 48 images are acquired for three velocity components at one measured plane. To obtain velocity at three boundary planes, a total of 144 images need to be processed. If one or more planes are needed for CFD validation, a large number of images have to be processed. Therefore, velocity image processing would be very time consuming if the magnitude image could not be segmented automatically.

4.2.2 2D cine PC phase image segmentation

The phase image segmentation procedure is composed of the following steps:

- segment the spin magnitude image by a region growing technique to obtain the vessel image

$$I - \begin{cases} I_m, & \text{if } (i,j) \subseteq \text{ROI}; \\ 0, & \text{otherwise.} \end{cases}$$

- register the 2D phase image with the magnitude image by calculating the correlation factor between two images.

- operate the phase image I_p by: $I_{p1} = a \times I_m + I_p$; where a is an integer, greater than 10000.

- let I_{p1} 0 if $I_{p1} < \frac{a}{2}$

- set the resultant phase image $I_{pr} = I_{p1} - a \times I_m$

The segmented velocity image can then be smoothed by conventional 2D smoothing methods giving a reasonably continuous velocity distribution at the plane in question.

4.3   Velocity image registration and interpolations

During each MR scan session, the following procedures are executed to obtain a complete set of images required for the study.

- Series 1: Localize scan to obtain the physical location of the target vessels. This scan is very quick (2 or 3 minutes). The information can be used to choose the 2D TOF scan region and the location of velocity scan planes.

- Series 2: 2D TOF scan to obtain geometrical data. The scan sequence was described in section(3.1).

- Series 3. Choose two or three planes from the image in serial 1 and perform the first Phase-Contrast scan. Velocity encoding is normally in the axial or Superior/Inferior (S/I) direction to acquire velocity (phase) images and magnitude images. It takes 12 minutes for a NEX 2 and matrix 256x128 scan.

- Series 4 and 5: Repeat step 3, but the velocity encoding directions are in the Anterior/Posterior (A P) and Right/Left (R/L) respectively to acquire in-plane velocity information.

It should be noted that anatomical and velocity data are acquired with different scan sequences and at different times. Different velocity component data are also acquired at different times. To match the measured velocity data with geometry, image registration steps are needed: firstly, combine three velocity component images to 3D velocity vectors, and secondly, put velocity data to the bifurcation boundary planes.

Since phase images give velocities at each pixel point, while, in a CFD calculation, the velocity boundary condition requires velocity values at each cell centre point and each calculation time step. Therefore, velocity interpolations in both space and time are necessary. A pair of NAG surface interpolation subroutines was used to perform the velocity spatial interpolation. The subroutines generate a 2D surface which interpolates a set of scattered data points, using

the method of Renka and Cline [181].

Velocity image registration has been achieved in two different ways in this study: (1). Physical registration, and (2). Logical registration. The former was developed at the early stage of the work, while the latter is the method adopted at present.

4.3.1 Physical registration

Physical registration is a straightforward way in which an assumption is made that after proper coordinate transformations (different for individual scans), all velocity images can be combined to produce velocity vectors at each pixel and each time point. These velocity vectors can then be located to the physical position of the boundary plane according to scan parameters such as Field-of-view (FOV) and plane location.

After segmenting all velocity (phase) images velocity image registration is performed by the following steps. Firstly, it is assumed that the vessel contour locations in image serial 3 are the true vessel locations, the relative images in serial 4 and 5 can be registered at the same contour location as in serial 3 by matching the contour centre points. Velocity vectors for each pixel are also generated. Secondly, the pixel location is converted from (i,j) to physical location (x_m, y_m) according to the FOV and scan plane location. The region surrounded by the contour should ideally overlap the boundary plane region, otherwise adjustment needs to be made. Thirdly, interpolation is performed to obtain velocity vectors at each cell centre point $\vec{V}(x_n, y_n, z_n)$, or in three components format $U(x_n, y_n, z_n)$, $V(x_n, y_n, z_n)$, $W(x_n, y_n, z_n)$.

It should also be mentioned that in this study, the bifurcation model was assumed to be rigid. However, it is found that movement of the arterial vessel during the cardiac cycle is about 10% of its diameter in the radial direction plus a small movement of the whole vessel (changing the centre point). The adjustment of the vessel centre point displacement can be achieved by adding factors in the "x" and "y" directions but the adjustment of wall movement in the

radial direction is very difficult because it is asymmetric, nonlinear and case-dependent. In this approach, only the first adjustment has been made and it is guaranteed that each phase image pixel in the ROI is located inside the mesh region.

4.3.2 Logical registration

In CFD solver CFX4.0, time-dependent velocity boundary conditions are specified in a user subroutine USRBCS, where velocity data are organized in a structure based on block number and integer parameters (I,J,K), which give the relative location of the grid in the block, for each cell centre point. Only velocity values for each component (U,V,W) are read, it does not need the physical location (x_n, y_n, z_n) of each mesh cell centre point. Therefore, it is possible to process each phase image separately regardless of the spatial relationship among them.

The 2D segmentation produces arterial contours and values of each velocity component at each pixel and time step. To perform the registration, it is assumed that the segmented arterial contour represents the true lumen inner surface at that moment, and a mesh is generated within the contour using the same grid generation parameters as used in the bifurcation mesh generation, velocity data are then interpolated from phase image pixels to mesh cell centres and arranged in a format that can be read into USRBCS.

Because this method does not rely on any physical location relationship among images, it is called logical registration. By using this method, the only common information shared among images are the mesh generation parameters. One of the main advantages of the algorithm is that there is no need to generate spatial relationships among images. In pratice, phase image registration among serial 3, 4, 5 can be avoided, eliminating registration errors due to mismatch between velocity image and boundary plane as described above. Another advantage is that it has the ability to compensate the non-linear error caused by vessel wall movement in the radial direction during cardiac cycles. This is because the arterial wall

moves during the cycle, so that at a given plane the absolute grid coordinates extracted from images acquired at different times may vary. However, the relative positions of grid points to the vessel wall do not have to change with time. The method also guarantees that all phase image velocity pixels are inside the vessel boundary plane which will benefit the evaluation of flow rate. On the negative side, this method is heavily dependent on the accuracy of vessel contour segmentation.

4.3.3   Error analysis of the registration methods

A mislocation of vessel wall for one velocity component will cause misregistration of the velocity vector when three velocity components are combined together, which will obviously give a wrong result. Because of random noise in the MR image, there is no fully automatic image segmentation technique that can guarantee an accurate result without careful checking. Frequent inspection of the segmentation result is a good way to minimise errors, a specifically designed, easy to use graphic user interface will be useful for this purpose.

4.3.4   Temporal interpolation

The temporal interpolation is obtained by using cubic splines to interpolate velocity values from 16 points in one cardiac cycle to the time steps which are needed by the computational simulation (here 40) at each mesh point at the boundary planes. Either uniform or non-uniform time steps can be achieved by the interpolation to meet the requirement of CFD calculation.

One difficulty in generating velocity boundary conditions from MR velocity images is the conversion from image pixel intensity to velocity value as described in section 2.2.4.1. It is known that the phase image pixel intensity is proportional to the velocity value at the same point. However, it is not able to answer the question of quantitative pixel intensity to absolute velocity conversion from scan information. To convert the pixel intensity to absolute velocity

value, first, it would be necessary to calculate the Reynolds number of the flow through the

plane. As the Reynolds number is directly proportional to the flow rate, for a given Reynolds

number, there will be a corresponding flow rate. In the following computational cases 1 and

2, the absolute velocities were determined based on an temporal mean Reynolds number of

500 and 300 respectively.

Chapter 5

CFD code description

CFD methods were generally described in section(2.4). In this chapter a more detailed description of CFD techniques, with an emphasis on the techniques used in the CFD package CFX4, is given.

The CFX4 flow modelling software is a suite of programs for the prediction of laminar and turbulent flow, and heat transfer. The first version of the code (originally FLOW3D) was limited to simple Cartesian and cylindrical geometries. Release 2 of the software overcame this limitation through the use of a body-fitted coordinate system. Release 3 and 4 extended the geometric capabilities of the code by using the facility of multi-block, or block-structured grids; i.e., the grid may now be constructed by gluing together an arbitrary number of topologically-rectangular blocks.

The suite of CFX programs consists of four parts. They are:

1. Pre-processor. The problem geometry and numerical grid can be defined in this part. The package offers easy to use interactive grid generators such as CFX-MESHBUILD and CFX-BUILD to generate grids in regular geometries. This study deals with irregular, complex geometries which cannot be defined by the software directly. Instead, purpose-built grid generation programs have been developed, which were covered in

127

chapter 3 and 4.

2. Frontend Module. The Frontend takes the input specification of the problem and converts it from a form convenient for the user into a form designed for efficient execution. At the same time, detailed error checking is performed. The problem is specified in a single data file by the Command Language itself. User-defined Fortran routines may be included for features that are too complex to be described using the Command Language.

3. Solution Module. The solution module solves the discretised representation of the problem. It receives the information in a form that permits maximum efficiency on different types of computer including vector and parallel processors. This is the main part of the package used in this study.

4. Post-processor. Although the package supports a graphic post-processor to visualize the predictions in various forms, they are not quite suitable for presenting arbitrary 3D objects. Instead, a specifically designed post-processing graphic package – EnSight was used in the study to show the predictions.

The pre-processing and post-processing parts have been described in previous chapters. In this chapter, the solution module, which is the core of a CFD package, is described and discussed. The description was organized in a sequence that started from the governing equations, discretization, and solution methods to the definition of boundary conditions. Finally, possible validation methods are discussed.

5.1 Governing equations

The basic set of equations solved by the program for the flow comprise equations for the conservation of mass, momentum and energy. Written in coordinate free tensor notation,

they are continuity equation

$$\frac{\partial \rho}{\partial t} + \nabla \cdot (\rho \mathbf{U}) = 0 \tag{5.1}$$

momentum equation

$$\frac{\partial \rho \mathbf{U}}{\partial t} + \nabla \cdot (\rho \mathbf{U} \otimes \mathbf{U}) = \mathbf{B} + \nabla \cdot \sigma \tag{5.2}$$

where σ is the tensor:

$$\sigma = -p\delta + (\zeta - \frac{2}{3}\mu)\nabla \cdot \mathbf{U}\delta + \mu(\nabla \mathbf{U} + (\nabla \mathbf{U}^{\ T}) \tag{5.3}$$

and **energy equation:**

$$\frac{\partial \rho H}{\partial t} + \nabla \cdot (\rho \mathbf{U} H) - \nabla \cdot (\lambda \nabla T) = \frac{\partial p}{\partial t} \tag{5.4}$$

where H is the total enthalpy, given in terms of the static (thermodynamic) enthalpy h by:

$$H = h + \frac{1}{2}\mathbf{U}^2. \tag{5.5}$$

Here ρ is the fluid density, $\mathbf{U} = (U, V, W)$ the fluid velocity, p the pressure, T the temperature and t is time. Further $\mathbf{B}$ is a body force, μ is the molecular viscosity, ζ is the bulk viscosity and λ is the thermal conductivity.

These equations represent 5 transport equations in the unknowns U, V, W, p, T, ρ, h. They are completed by adding two algebraic equations from thermodynamics, the **equation of state**, relating density to temperature and pressure,

$$\rho = \rho(T, p) \tag{5.6}$$

and the **constitutive equation**, relating static enthalpy to temperature and pressure

$$h = h(T, p) \tag{5.7}$$

All the above transport equations can be expressed as a scalar **advection-diffusion equation**, given in coordinate free notation by:

$$\frac{\partial \rho \Phi}{\partial t} + \nabla \cdot (\rho \mathbf{U} \Phi - \Gamma \nabla \Phi) = S \tag{5.8}$$

and in index notation by:

$$\frac{\partial \rho \Phi}{\partial t} + \frac{\partial}{\partial x^i}(\rho U^i \Phi - \Gamma \frac{\partial \Phi}{\partial x^i}) = S \tag{5.9}$$

where Γ is the diffusion coefficient, and S is a source or sink term representing creation and destruction of Φ and Φ is a general form of field variables.

5.2 Discretisation and solution algorithms

5.2.1 Discretisation: rectangular grids

In this section, some details are given of the discretisation methods, both temporal and spatial, used in CFX4 The basis of the code is a conservative finite-difference, or finite-volume, method with all variables defined at the centre of control volumes which fill the physical domain being considered. Each equation is integrated over each control volume to obtain a discrete equation which connects the variable at the centre of the control volume with its neighbours.

All of the equations to be solved, except the continuity equation, have the same general form of equation(5.8 Integrating over the control volume gives:

$$\int \frac{\partial \rho \phi}{\partial t} dV + \int \rho \phi \mathbf{U} \cdot \mathbf{n} dA - \int \Gamma \nabla \phi \cdot \mathbf{n} dA = \int S dV. \tag{5.10}$$

where Γ is the relevant effective diffusivity for the variable ϕ. All terms in the equations are discretised in space using the second-order central differencing except the advection terms and the convection coefficients obtained using the Rhie-Chow interpolation formula.

5.2.1.1 Diffusion terms

To illustrate the diffusion and advection terms, consider the control volume shown in Figure 5.1. The diffusion term at the west face of the control volume is discretised as

$$\int \Gamma \nabla \phi \cdot \mathbf{n} dA = \frac{\Gamma A_w}{h_w}(\phi_P - \phi_W) \equiv D_W(\phi_P - \phi_W). \tag{5.11}$$
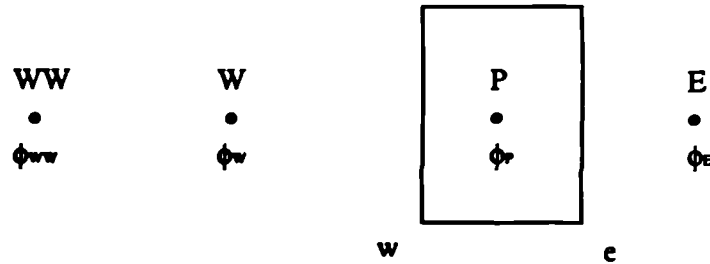
Figure 5.1: Control Volume Notation

Here A_w is the area of the west face, h_w is the distance between the west (W) and central (P) nodes and D_W is the west diffusion coefficient.

5.2.1.2 Advection terms

The treatment of the advection terms determines the accuracy of the solutions of the model equations in CFX4. *The terms are difficult because more accurate schemes tend to be less robust or slower.* Because of this, there is a choice of discretisation methods available in the code. These range from diffusive, simple upwind schemes through to bounded, quadratic upwind schemes.

- **Upwind Differencing (UDS)** In this scheme, the advected value of the variable ϕ at the west face of the control volume (ϕ_w) is taken to be ϕ_W, so that, at the west face

$$\int \rho \phi \mathbf{U} \cdot \mathbf{n} dA = \rho \mathbf{U}_w A_w \phi_W \equiv C_W \phi_W. \qquad (5.12)$$

Here C_W is the convection coefficient at the west face. This gives a matrix coefficient for the west point of:

$$A_W = MAX(C_W, 0) + D_W \qquad (5.13)$$

131

- **Central differencing (CDS)** This is the most natural discretisation for the advection term. In the scheme, ϕ_w is given by

$$\phi_w = \frac{1}{2}(\phi_W + \phi_P).\tag{5.14}$$

This scheme is formally second-order accurate, but is rarely used because it is not robust. It often requires very small under-relaxation factors or gives non-physical solutions.

- **Hybrid differencing (HDS)** This is a modification to UDS in which central differencing is used if the mesh Peclet number ($Pe = \rho u x/\Gamma$, where u is the velocity, x is the cell width and Γ is the diffusion coefficient) is less than 2, and UDS, but ignoring diffusion is used if the mesh Peclet number is greater than 2. The west matrix coefficient in this case is

$$A_W = MAX(\frac{1}{2}C_W, D_W) + \frac{1}{2}C_W.\tag{5.15}$$

This scheme is again first-order accurate, but is slightly better than UDS because second-order central differencing will be used across streams and in regions of low flow. *This scheme is used as the default in the program.*

- There are other higher order accurate schemes which are less compact than previous schemes because of the presence of the ϕ_{WW} and/or ϕ_P terms. For example, in the second-order accurate Higher-order upwind differencing (HUW), $\phi_w = \frac{3}{2}\phi_W - \frac{1}{2}\phi_{WW}$; in the third-order accurate Quadratic upwind differencing (QUICK), $\phi_w = \frac{3}{8}\phi_P + \frac{3}{4}\phi_W - \frac{1}{8}\phi_{WW}$. For special requirements, other higher-order accurate schemes are available in the code, such as **CCCT**, **CONDIF**, **MUSCL**, **NOCONV** and **NOMATX**.

5.2.1.3 Time stepping procedures

For transient problems, the time derivatives of flow variables in the differential equations can be approximated in many ways.

- **Backward difference:** by default, a fully implicit backward difference time stepping procedure has been implemented. That is, if the equations are written in the form

$$\frac{\partial \phi}{\partial t} = F(\phi) \qquad (5.16)$$

the discretised form is

$$\frac{\phi^n - \phi^{n-1}}{\Delta t} = F(\phi^n) \qquad (5.17)$$

The terms on the left hand sides can be absorbed into the source and sinks for each equation and the resulting equations at the nth time step look like the discrete steady state equations. These can then be solved using the standard steady state techniques.

- **Higher order accurate algorithms** are also available in the code. They are: Second-order backward difference which needs ϕ^{n-1}, ϕ^{n-2} and the time difference on the previous time step (if it is not the fixed time step case), to obtain ϕ^n; Time centred **Crank-Nicolson treatment**. It is a two step procedure, the first being to use a backward difference procedure over the first half step, and then an extrapolation to give the solution at the end of the time step. Although it only needs ϕ^{n-1}, a centred time value ϕ^* is also needed to be calculated to obtain ϕ^n.

5.2.1.4 Source terms

For each equation, the source term is written in the following way:

$$\int S dV = SU + SP\phi_p \qquad (5.18)$$

where SP is non-positive. The SP term then enhances the diagonal of the matrix giving more diagonal dominance and thus better solution behaviour.

5.2.2 Discretisation: Body-fitted grids

For the treatment of arbitrary geometries, body-fitted coordinates are included in the package. It is achieved by employing the algorithm proposed by Rhie and Chow [182, 183].

The basic idea of the **Boundary fitted coordinate systems** is to use a curvilinear coordinate transformation to map the complex flow domain in physical space to a simple (i.e. rectangular) flow domain in computational space. In other words, the Cartesian coordinate system $(x^i) = (x, y, z)$ in the physical domain is replaced by a curvilinear coordinate system $(\xi^i) - (\xi, \eta, \zeta)$ such that boundaries of the flow domain correspond to surfaces $\xi^i = $ constant. The equations are then discretised with respect to *the computational space coordinates*. Boundary conditions may then be implemented naturally in the rectangular computational domain, at the expense of making the partial differential equations more complicated due to the non-linear coordinate transformation. Because of the complexity of a general 3D domain, it is not always easy, or indeed possible, to construct an orthogonal coordinate system. Also even when it is possible to construct an orthogonal coordinate transformation, it is not possible to have complete control over the distribution of grid nodes on the boundary or over the spacing between grid lines in regions where it is desired to have a high degree of resolution. Therefore, it is assumed that the computational space coordinate system (ξ^i) is a general non-orthogonal system.

It should be assumed that the coordinate transformation is non-singular. As a consequence the Jacobian matrix is non-singular, so its inverse always exists, and its determinant is always non-vanishing. Moreover, it is assumed throughout that the coordinate transformation is positively oriented, that is for a right-handed frame of local basis vectors in computational space is mapped to a right-handed frame in physical space, and vice-cersa. We then have two basic transformation equations

$$\frac{\partial \phi}{\partial \xi^i} = \frac{\partial x^j}{\partial \xi^i} \frac{\partial \phi}{\partial x^j} = J^j_i \frac{\partial \phi}{\partial x^j} \tag{5.19}$$

$$\frac{\partial \phi}{\partial x^i} = \frac{\partial \xi^j}{\partial x^i} \frac{\partial \phi}{\partial \xi^j} = \bar{J}^j_i \frac{\partial \phi}{\partial \xi^j} \tag{5.20}$$

Of these two equations, (5.20) is the most important, since, in the final analysis, all derivatives must be expressed relative to computational space, where variables are defined on a rectangular grid, so that derivatives may be approximated by standard finite difference oper-

ators. It is therefore important to be able to obtain numerical approximations to the inverse Jacobian matrix.

The price that has to be paid for the simplicity of implementing boundary conditions using body-fitted coordinate systems is the increase in complexity of the equations of motion when transformed to the non-orthogonal coordinate system (ξ^i). As described earlier, the main idea, in its simplest form, is to take the equations of motion in physical space, and to replace all physical space derivatives by computational space derivatives using equations(5.19) and (5.20).

The full discussion of the mathematical analysis of coordinate and equation transformation is very complex which can be found in [184]. After the transformation, the discretisation of the advection-diffusion equation is then straightforward. The finite difference representation of the values of ϕ on control volume faces and the computational space derivatives $\frac{\partial \phi}{\partial \xi^j}$ for the total flux vector can be achieved by the methods described in section(5.2.1), such as UDS, HDS, or higher-order accurate CDS, HUW, and QUICK.

5.3 Solution strategy for the linearised transport equations

5.3.1 Solution strategy

After the discretisation step, the governing PDEs are all transformed to linearised algebraic equations which can be solved by computer with appropriate numerical methods. A number of different methods are available for the solution of the linearised transport equations. Flexibility is provided in order to cater for the widest possible range of problems, but sensible defaults are set so that, for the majority of problems, the user need take no action in respect of the solvers.

The linear equations are derived by integrating transport equations over control volumes (cells), thus each equation may be regarded as 'belonging' to a particular variable and to a particular cell. Such an equation is a formula which describes the influence on that particular variable in that particular cell of (a) other variables in the same cell; (b) values of the same variable in neighbouring cells; and (c) values of the other variables in neighbouring cells.

Iteration is used at two levels: an **inner iteration** to solve for the spatial coupling for each variable and an **outer iteration** to solve for the coupling between variables. Thus each variable is taken in sequence, regarding all other variables as fixed, a discrete transport equation for that variable is formed for every cell in the flow domain and the problem is handed over to a linear equation solver which returns the updated values of the variable. The non-linearity of the original equations is simulated by reforming the coefficients of the discrete equations, using the most recently calculated values of the variables, before each inner iteration.

5.4 Boundary conditions

After the generation of the model grid, boundary conditions are the most important factors to define the physical problem and influence the CFD predictions. Several different types of boundary conditions can be used in CFX4. However, the choice of which type of boundary condition to be used really depends on the available information and problem itself.

5.4.1 INLETS (Dirichlet boundary conditions)

An **INLETS** is a boundary where the values of variables are specified. Mathematically, this is known as a Dirichlet boundary condition. As one of the most important vectors in CFD, velocity values are always used as INLETS boundary conditions. The velocity at an inlet can be specified in one of two ways. Either normal and, if required, angular components of velocity should be set, or each individual component of velocity should be set. The two methods cannot be mixed on a given patch. Note that the patch type INLET can be

used to define *outflow*. That is, the velocity component perpendicular to the inlet can be specified to have a direction that is pointing away from the computational domain. This is only recommended for strongly diffusive flows where the user is sure that the outflow field is physically correct, say for example it is obtained from experiment or it is specified as fully developed. If the flow is convection dominated, and the outflow field is unphysical, the solution will display unphysical boundary layers normal to the outflow boundary.

5.4.2 Mass flow boundary conditions (Neumann boundary conditions)

Mass flow boundary conditions are used to model inflow and outflow boundaries where the total mass flow rate into or out of the domain is known, but the detailed velocity profile is not. Historically, in the first release of CFDS-FLOW3D, mass flow boundaries were first used to model *outlets*, and they were named **OUTLETS**. In this case, the following conditions are imposed:

1. **Neumann boundary conditions** are imposed on all transported variables, velocity k, ϵ, temperature etc. This means that their gradients are specified, rather than their values. All transported quantities are given zero normal gradient, with the exception of velocity, which is given constant normal gradient, as explained below.

2. This is equivalent to an assumption of fully developed flow at the outlet. It is most accurate when the outlet is placed far downstream, and the width of the flow domain is unchanging at the outlet. It is rather inaccurate if the flow is still developing as it goes through the outlet.

3. Pressure is extrapolated from upstream.

4. In order for the pressure correction equation, which is derived from the continuity equation, to be well posed in the case of incompressible flow, it is essential to maintain global mass continuity. That is, the total flow out of the domain must be equal to the total flow into the domain at all stages of the solution procedure.

The fully developed flow approximation is not valid for the case which has a sudden contraction at an outlet or has a sudden expansion at the outlet. In the former case, it may be better to model the 'outlet duct' and continue the outlet for a few control volumes downstream. In the latter case, greater accuracy can only be achieved by extending the flow domain to contain the region into which the flow expands.

Multiple outlets can be set if the mass flow boundary patches were put into 'groups'. Having defined the groups of mass flow boundary patches, it is necessary to define the total mass flow rate out of each group. There are two ways to do this:

- The actual mass flow rate of each group may be set (in kg/s by default).

- The fractional mass flow rate of each group may be set, based on the fraction of the total rate into the domain through all the inlet boundaries.

If the flow is incompressible, and no pressure boundaries have been set, it is essential to satisfy global mass conservation. It is generally more convenient to specify fractional mass flow rates. Global continuity is then achieved if and only if the fractions for each group sum exactly to unity. It is noted that the flow need not necessarily be out of a mass flow boundary. It also makes sense to have flow into a mass flow boundary. This is simply achieved by setting the appropriate mass flow rate to be negative, as the convention is that a positive mass flow rate at a mass flow boundary is out of the flow domain.

5.4.3 Pressure Boundary Conditions

Pressure boundary conditions are used to model inflow and outflow boundaries where the surface pressure is known, but the detailed velocity distribution is not. This condition is suitable for the case of a vessel venting fluid to the atmosphere at a constant pressure. Also, fixed values of temperature and user scalars may be specified at pressure boundaries. These values are used if the flow is into the solution domain.

Historically, pressure boundaries were introduced as a alternative to mass flow boundaries for flow problems with multiple outlets. The idea is that , in viscous flow problems with multiple outlets, steady state mass flow rates through the outlets, if they exist, depend on the relative pressure distribution across the outlets. If the pressure distributions are known, the mass flow rates can be predicted. Conversely, if the mass flow rates are known, the pressure distributions can be predicted. For the problem to be well posed, one of these pieces of information must be known. Which one is known determines the choice between pressure boundaries and mass flow boundaries.

The following conditions are imposed at outflow through a pressure boundary:

- Dirichlet boundary conditions are imposed on pressure.

- Neumann boundary conditions, i.e. zero normal gradients, are imposed on velocity.

- Neumann boundary conditions, are also imposed on all other transported variables.

As for mass flow boundaries, the assumption of zero normal velocity gradient is equivalent to a fully developed flow approximation. Note that, unlike the case of mass flow boundaries, the Neumann conditions on velocity are not modified to achieve global mass conservation. This is taken care of automatically in this case by the velocity-pressure correction procedure.

5.5 Validations

One current major difference between numerical simulation and physical model measurement is that a validation procedure is normally necessary for numerical simulation. This is because the CFD codes, possibly for reasons of commercial competition, have had their various features incorporated rather quickly. This means the procedure of 'code validation' (usually checking against careful experimental 'benchmark' data of high reliability) is still incomplete. The other reason is that the approximation errors of numerical simulation come not only from numerical techniques such as the spatial discretization algorithm, but also from the definition of the boundary conditions. Therefore, some justification of the quantitative accuracy

of CFD results should be made wherever possible.

For overall validation, there are normally two stages, internal and external. Firstly, internal validation checks the numerical errors. This can be achieved by testing the effects of:

- changing the density (or distribution) of the mesh, and

- (for time-dependent flow) changing the time step on the predictions of flow parameters in the regions of interest.

Secondly, external validation compares the numerical simulation results against data external to the code such as:

- analytical solutions of the basic equations,

- in vitro or in vivo measurements and

- comparative predictions using different codes.

The external validation is much more demanding because of the inconsistent availability of external data. For a very simple case like flow in a straight tube, analytical solutions can be obtained. A very popular example is the comparison of CFD predictions with Womersley's analytical solution for pulsatile flow in a compliant tube [185].

For most cases, however the Navier-Stokes equations cannot be solved analytically. When the model geometry is simple or can be described analytically, published experimental results (for the same model) may be available and quantitative validation can then be done. However, when the problem turns to be more complicated such as an arbitrary 3D geometry model or an anatomically realistic arterial model the validation will be very complex. It is because there is not only the difficulty of making an arbitrary physical model for experimental measurement but also the difficulty of the geometrical description of the model. This means even if there are experimental data available, an identical geometrical model generation for numerical simulation is still very difficult. Modern imaging techniques can help in such cases. The

in vivo arbitrary arterial vessel can be measured by state-of-the-art angiographic methods like MRI and/or ultrasound and numerical simulation can be based on these imaged data. MRI and ultrasound can also measure in vivo velocity in the vessel, enabling a comparison of prediction and measurement results to take place. These kinds of validation can offer some guarantee of the similarity of the model geometry. However, in analysing validation results, some other effects such as measurement resolution and wall movements, should be taken into account. It must be remembered that the numerical simulation is only performed on an arterial segment whereas in vivo measurement measures whole body effects.

As an overall comment on experimental comparisons, it is, of course, essential to apply 'best practice' rules to assess *experimental* uncertainty. As an alternative to measurement, validation by comparison predictions using different codes can be undertaken. This is particularly valuable if the codes use quite different algorithms, even, say, finite element and finite volume approaches. Although there is no consequent physical measurement, identical predictions from different CFD codes will give more confidence in the numerical results.

In this study, both internal and external validations are undertaken. The internal validation contains grid resolution and time step refinement tests. Apart from these, boundary condition setting and its effect on CFD predictions are also very important points which will be discussed in detail in the following chapters. Because of the arbitrary geometry of the bifurcations, there is no other study result that can be used to validate the overall CFD predictions. The external validation is carried out by comparing MR velocity measurements with CFD predictions at selected cross-sections in the model. Considering the fact that it is more likely to have measurement errors in measuring velocity profiles at the plane in branch vessels, the comparisons are normally carried out at a plane in the common vessel. Although the agreement of velocity profiles on a plane in the common vessel between the measurement and predictions does not indicate the agreement in the rest of the flow domain especially in the bifurcation region, a good comparison result at the chosen plane will give more confidence in analysing the CFD predictions.

Chapter 6

CFD predictions cases 1:

a human abdominal bifurcation

6.1 Introduction

At the aortic bifurcation, the iliac arteries frequently branch at different angles from the parent aorta and in some cases have out-of-bifurcation plane curvature. This asymmetry may contribute to the known differences in the incidence of atherosclerosis between right and left iliac arteries [186, 187, 188]. Combining data from these studies (a total of 273 patients), it appeared that disease was more common on the left than the right side in the ratio of 65 % to 35 %. There is strong evidence that atheroma occurs predominantly in the less acutely branching iliac artery. Further, there may be no side predilection at symmetrical bifurcations.

In order to understand how the artery is influenced by haemodynamic-related factors, detailed knowledge of flow patterns in complex geometrical models has been the aim which many researchers pursue. Caro et al [57] shows that many of the human aortic bifurcations and arterial bendings are non-planar. Relatively small values of the parameters which render the geometry non-planar appear significantly to affect the velocity distribution.

There are several parameters known to influence the local haemodynamics in the abdominal

bifurcation. The angle of bifurcation and branch-trunk area ratio have been investigated experimentally. Recently, the importance of considering the branchings of the abdominal aorta and its dorsoconcave curvature has been demonstrated in qualitative flow visualization studies [189]. Even the downstream iliac bifurcation has to be taken into consideration due to the triphasic flow waveform with retrograde flow during part of diastole [190]. As it is technically difficult to make anatomically realistic bifurcation models, which are generally constructed from autopsy, the experimental investigation was limitted to a small number of individual cases.

In this research five different human volunteers were scanned and abdominal bifurcation models (geometry reconstruction) were generated by the method presented in above chapters. Due to the poor quality of the velocity images, only two of them can be used in CFD simulations. In which, one was studied and published [191], the other is presented here. In this chapter, interesting flow parameters such as velocity and wall shear stress are presented via 3D vector and contour plots. Validation procedures are also carried out for the model.

6.2 Model geometrical description and boundary conditions

The numerical grid of the aortic bifurcation of a healthy human subject generated from MRA images has already been shown in chapter 3 Figure 3.10(b). The grid contains 24 blocks, making a total of 15300 3D computational cells and 23408 nodes.

Figure 6.1 gives 3D surface rendering for the abdominal bifurcation at four different view angles. The orientation in Figure 6.1(a) posterior to anterior (P/A), left to right (L/R), inferior to superior (I/S) are defined as the Cartesian coordinate system positive directions of x-axis, y-axis and z-axis respectively. The orientation description parameters such as P/A, L/R and I/S will be used in the following discussion.
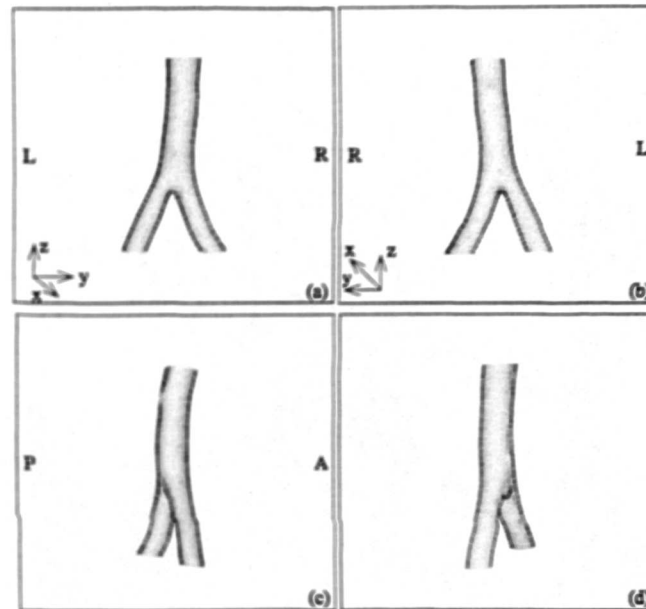
Figure 6.1: Geometrical description of the abdominal bifurcation model. (a) anterior view; (b) posterior view; (c) left view; (d) arbitrary view angle

The 3D surface rendering of the bifurcation shows that although the aortic bifurcation is complicated in shape, the two iliac arteries virtually lie in the same plane as shown in Figure 6.1(c). However, there is an out-of-plane curvature towards posterior-right in the common vessel as can be seen in Figure 6.1(d) and in (b). This curvature may alter flow patterns in the branch vessels. The two branch vessels are different in shape, the left branch is straight while the right branch has a bending toward to the right side.

The logical registration method described in section(4.3.2) was used to process the Cine 2D PC velocity images. A very effective way to demonstrate the processed velocity image results at the boundary planes is to plot the 3D velocity vectors and compare them with the geometry
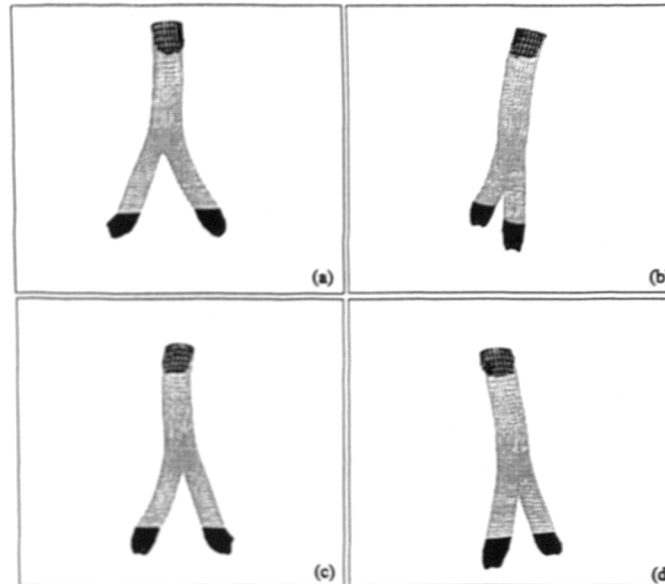
Figure 6.2: 3D velocity profiles at boundary planes during flow acceleration phase

model. If the data processing is correct, the vectors should follow the shape of the geometry model at the boundary planes. Figure 6.2 gives the 3D plot results from different view angles.

In this subject, the distances between the aortic bifurcation and iliac bifurcations are very short (about 50mm, less than 6 diameters long). Consequently, flow at the exits of the iliac arteries cannot be assumed to be fully developed. Since the common vessel is more likely to have a developed flow than its branches, MR measured 3D velocity profile boundary conditions were specified at the two exit planes and a mass flow boundary condition was prescribed at the entrance to the abdominal aorta. The boundary plane grids shown in Figure 3.10(c) were formed by 8 patches according to the block structure. From the measured velocity data at the inlet of the common vessel together with the areas of each grid cell, mass flow rate ratios among the patches at each time step can be derived which were used as the inlet boundary condition in the abdominal aorta.
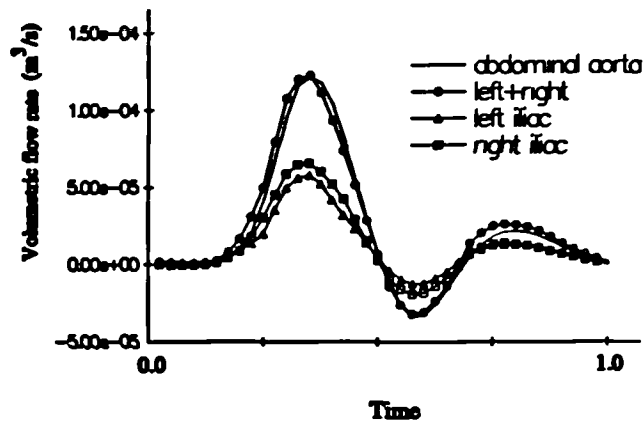
Figure 6.3: Volumetric flow rate calculated from MR measured velocity images for the three boundary planes.

Figure 6.3 shows the velocity waveforms corresponding to the subject studied. From this figure it can be found that: (1) blood velocities are very low during part of the cardiac cycle (from time step 0 to 8, 20%). Consequently, flow patterns are not expected to change very much during this part of the cycle; (2) following flow deceleration, flow reversal occurs (from time step 21 to time step 27, 17%). The figure also shows that mass conservation is generally satisfied among the inflow and outflow boundaries ($M_{common} \approx M_{left} + M_{right}$) in most of the time during the cycle. It is not expected to achieve a perfect fit because of measurement and processing errors, and the compliant nature of arteries.

6.3 CFD Predictions

To give a complete picture of the flow patterns at the bifurcation, CFD predictions are displayed in the form of velocity profiles including velocity magnitude contours, 3D vectors and secondary flow, as well as wall shear stress distributions at some time instants during a cardiac cycle. Because of the geometrical complexity, there is no symmetrical plane in the model that can be used to present the CFD predictions, flow parameters are displayed at a number of selected transverse sections.

6.3.1 Velocity distribution

Predicted velocities are presented in two different fashions. Firstly, to give an overall picture of velocity variations along the axial direction, 10 planes are chosen along the longitudinal direction of the model and velocity contours are presented on the planes at three time points in a cycle. Secondly, to show more detailed flow patterns in the common, left branch and right branch vessels, four planes are chosen (perpendicular to the vessel axis) to present velocity contours, secondary flow and velocity profiles at different time steps.

Figure 6.4 a), (b and (c) show the variation of velocity contours along the axial direction of the model at time steps 9 (early stage of flow acceleration), 17 (mid-way of flow deceleration) and 23 (maximum reverse flow phase) respectively. During early flow acceleration, flow is developing in the common vessel and high velocities are skewed towards one side following the abdominal aorta curve (posterior side). Although only three snapshots are presented here, it has been found that in most of flow acceleration and early flow deceleration phases, flow is typically "plug" in the abdominal aorta and develops little in the iliac arteries.

At mid-way of flow deceleration (Figure 6.4(b)), flow in the daughter vessels is affected by the curvature of the common vessel. High velocities are not found near the inner wall of the daughter vessels as observed in planar bifurcation model, but move towards the posterior side
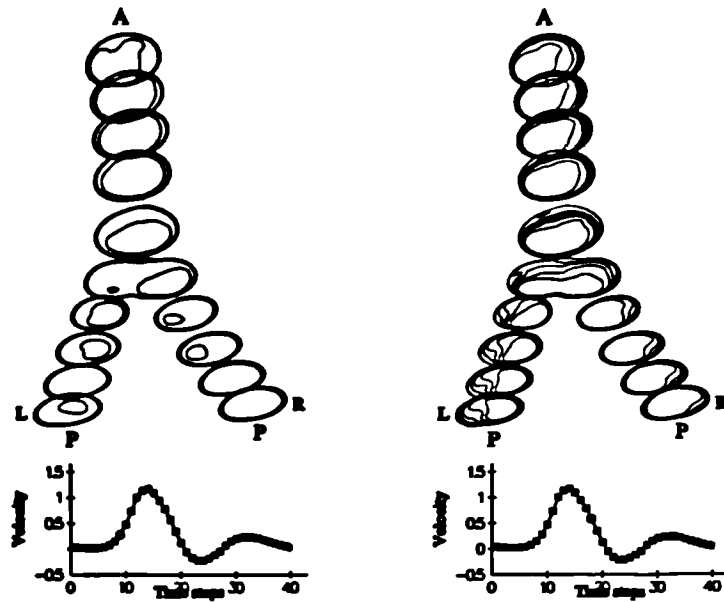
a   at time step 9   (b) at time step 17
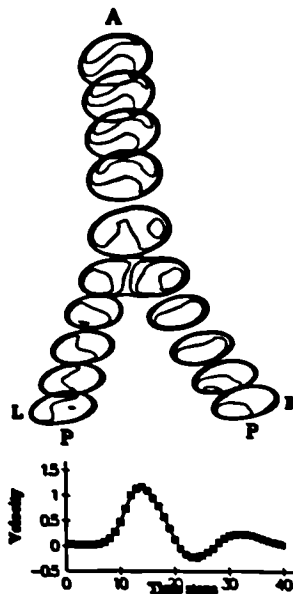
(c) at time step 23

Figure 6.4: Velocity distribution (contours) along the model axial direction at different time

points in a cardiac cycle. The velocity magnitudes are in the range of 0.0—0.578(m/s).

149

of the vessel. They are between right-posterior for the left branch and left-posterior for the right branch.

Figure 6.4(c) shows the velocity contours at a diastolic phase. When flow is reversed, flow patterns are now different from those described above. In the left branch vessel higher velocities can be seen near the outer wall of the vessels with low velocity near the inner wall. In the common vessel, instead of being at the outside of the curve (posterior side), high flow is shifted towards inside (anterior side).

To give a clear and more complete picture of the time-dependent velocity distributions, velocity data are shown at four chosen planes. They are plane A (top of the curvature in common vessel , plane B (upstream of the bifurcation flow divider), planes C and D (one diameter downstream of the bifurcation) as indicated in Figure 6.5, and at time steps 10, 16, 19, 22, 29. At each time step, velocity contours, secondary flows and velocity profiles along two perpendicular centrelines are given in Figures 6.6(a) and (b), 6.7(a) and (b) and 6.8. The definition of orientation parameters (Anterior/Posterior, Left Right) is the same as in Figure 6.1(a). The velocity curve at the bottom of each figure indicates the time point at which the flow pattern is displayed. At each plane secondary velocity vectors are shown on the left and velocity profiles and contours are given on the right. All secondary flow vectors are plotted on the same scale. The legend gives the velocity contour values.

From Figure 6.6(a), it can be noticed that the velocity profiles are flat almost everywhere, while secondary flow can be noticed at planes C and D. In the flow deceleration phase (Figure 6.6(b)), velocity profiles are developing and high velocities skew towards P-R in the left branch and L-P in the right branch vessel. Secondary flow patterns do not change very much but are stronger than in Figure 6.6(a). A single vortex appears near the L-A side wall in plane C and at R-A side in plane D. From the velocity profiles at the (f) and (h) in Figures 6.6(a) and (b), it can be found that both vortices occur at locations where velocities are relatively lower. There is no evidence of flow separation.
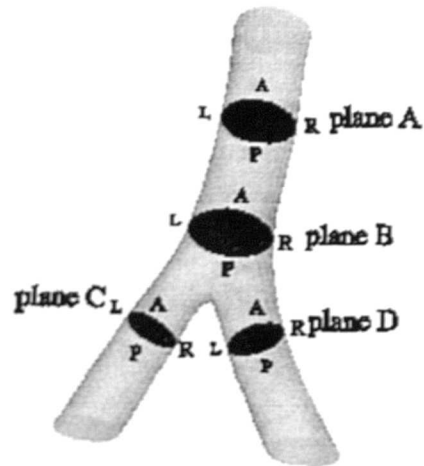
Figure 6.5: 3D surface rendering of the human abdominal bifurcation showing the locations of the chosen planes where velocities are displayed. Planes B, C and D are approximately one diameter away from the apex.

Figure 6.7(a) shows the velocity distribution at the moment when flow starts to reverse. As expected, the change in flow pattern starts from the boundary (near wall) area where the forward momentum of blood is small. It can also be noticed that the backward flow in the right branch is higher and occurs earlier than in the left branch. The high reverse velocity regions are close to the L-P, R-P and Anterior wall in the left, right branch and common vessel respectively. The backward flow develops further until it reaches a maximum as shown in Figure 6.7(b). A one-vortex secondary flow pattern can be found at plane C.

Velocity distribution in a diastolic phase is shown in Figure 6.8. At this moment, high velocities occur near the Anterior, A-R and Posterior wall in the left branch, right branch and common vessel respectively. These patterns are different from those discussed above.
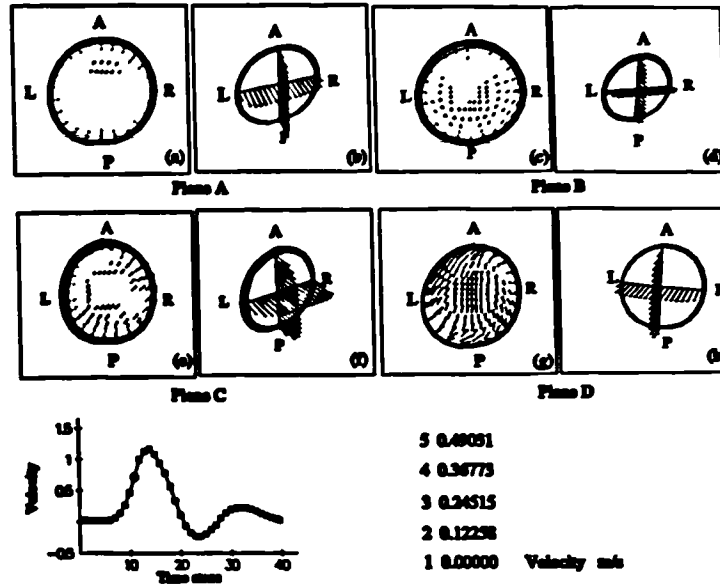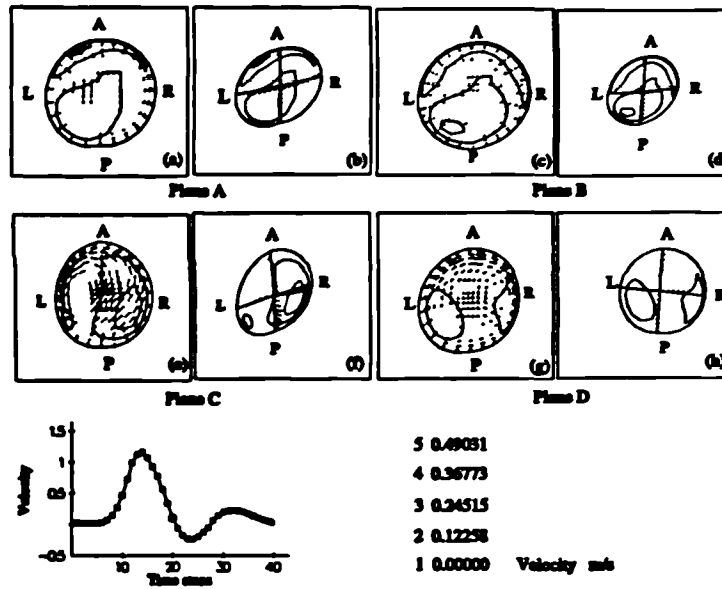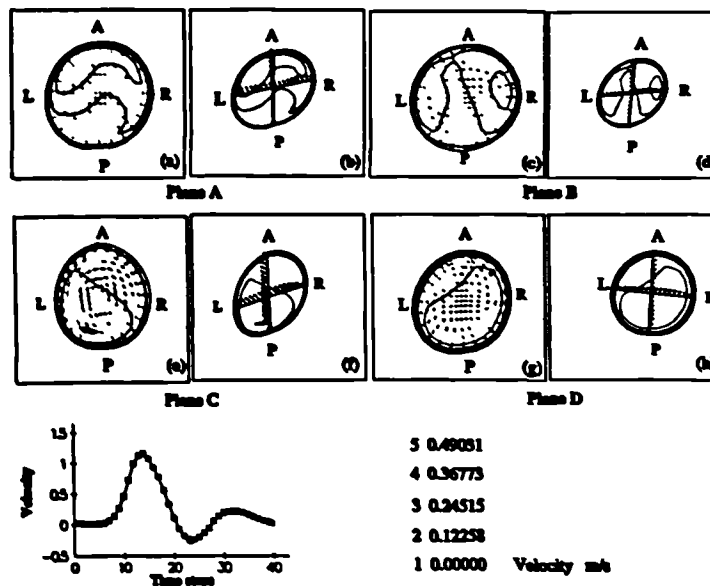
(a flow acceleration
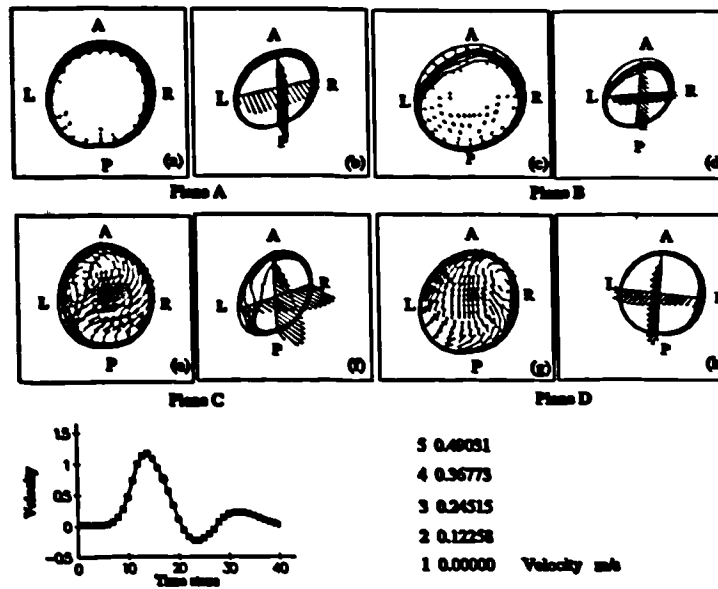
(b) flow deceleration

Figure 6.6: Velocity distributions at four planes in flow acceleration and deceleration phases. The velocity curve at left bottom in each figure gives the time phase of the result in the cycle. It corresponds to the central point velocity in the common vessel.

(a) beginning of reverse flow

(b) maximum reverse flow phase

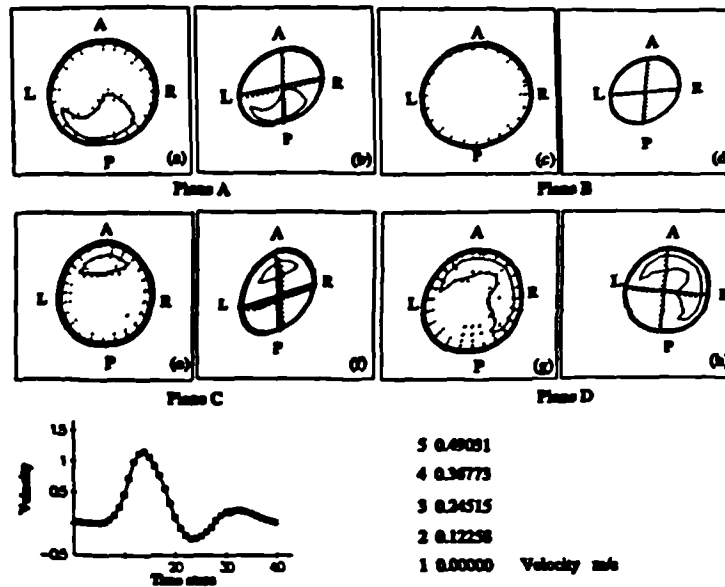Figure 6.7: Velocity distributions at four planes in reverse flow phases

Figure 6.8. Velocity distributions at four chosen planes at a diastolic phase.

6.3.2 Wall Shear Stress distribution

Wall shear stress (WSS distributions are presented in the form of contours on the wall surface at four time steps. They are time step 10 (midway of acceleration), time step 17 (midway of deceleration), time step 23 (reverse flow) and time step 30 (diastolic phase) as shown in Figures 6.9(a), (b) and 6.10(a) and (b) respectively.

From Figure 6.9, it can be found that in the common vessel the high WSS region is close to the posterior side (outside of the curvature) and the low WSS region occurs on the anterior side at both flow acceleration and deceleration phases. Comparing the two branches, the right branch vessel always has a higher WSS than the left branch during these times.

Figure 6.10 gives WSS contours in the reverse flow and diastolic phases. Different from above, high WSS occurs in the anterior and low WSS happens in the posterior region during the reverse flow phase. Although there is another flow acceleration phase in diastole, WSS patterns in Figure 6.10(b) are not the same as in Figure 6.9(a).
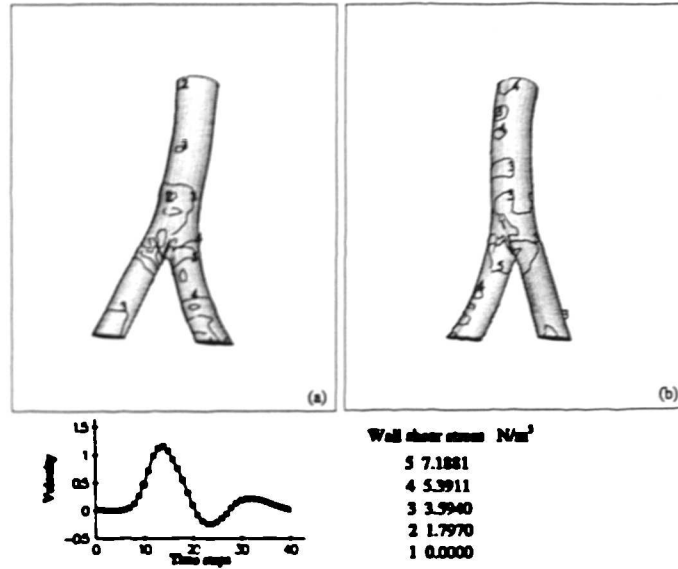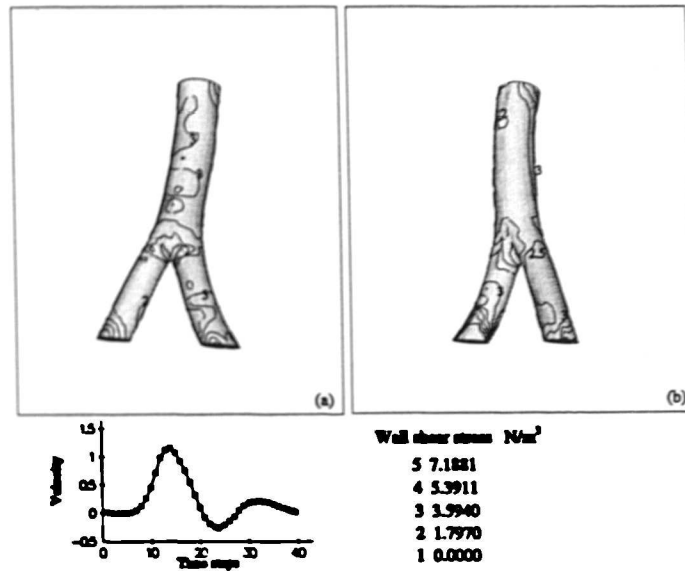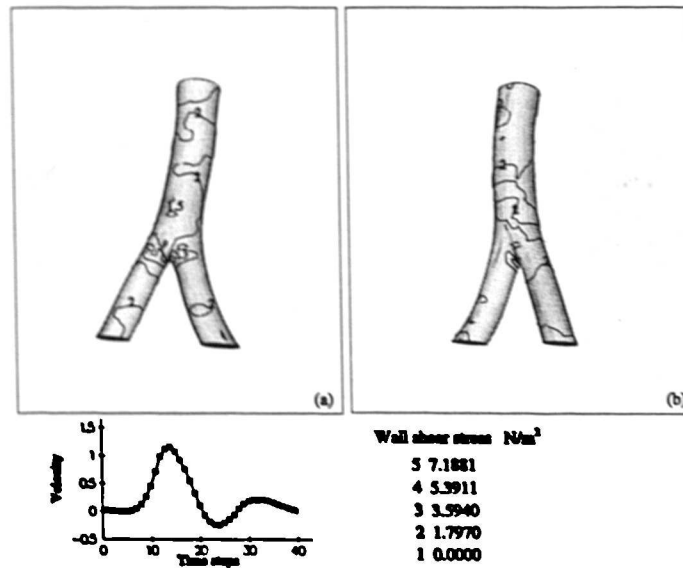
(a) flow acceleration phase
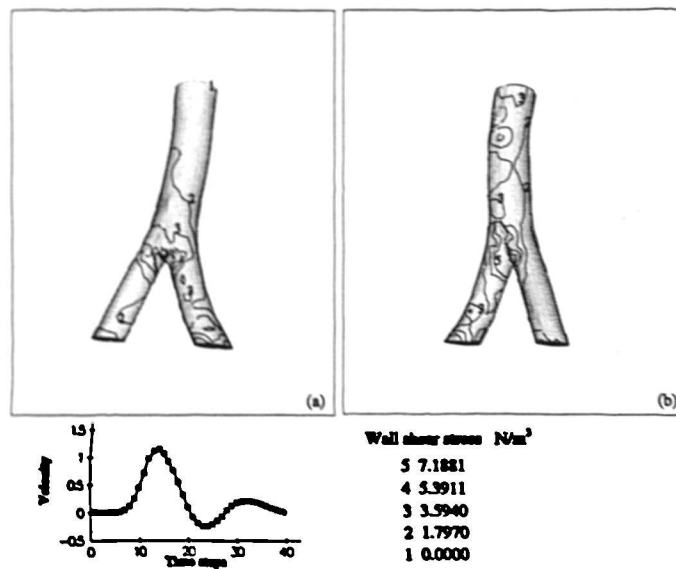
(b) flow deceleration phase

Figure 6.9: WSS contour plots in flow acceleration and deceleration phases at different view angles.

155

(a) reverse flow phase

(b) diastole phase

Figure 6.10: WSS contour plots at reverse flow and diastolic phases at different view angles.
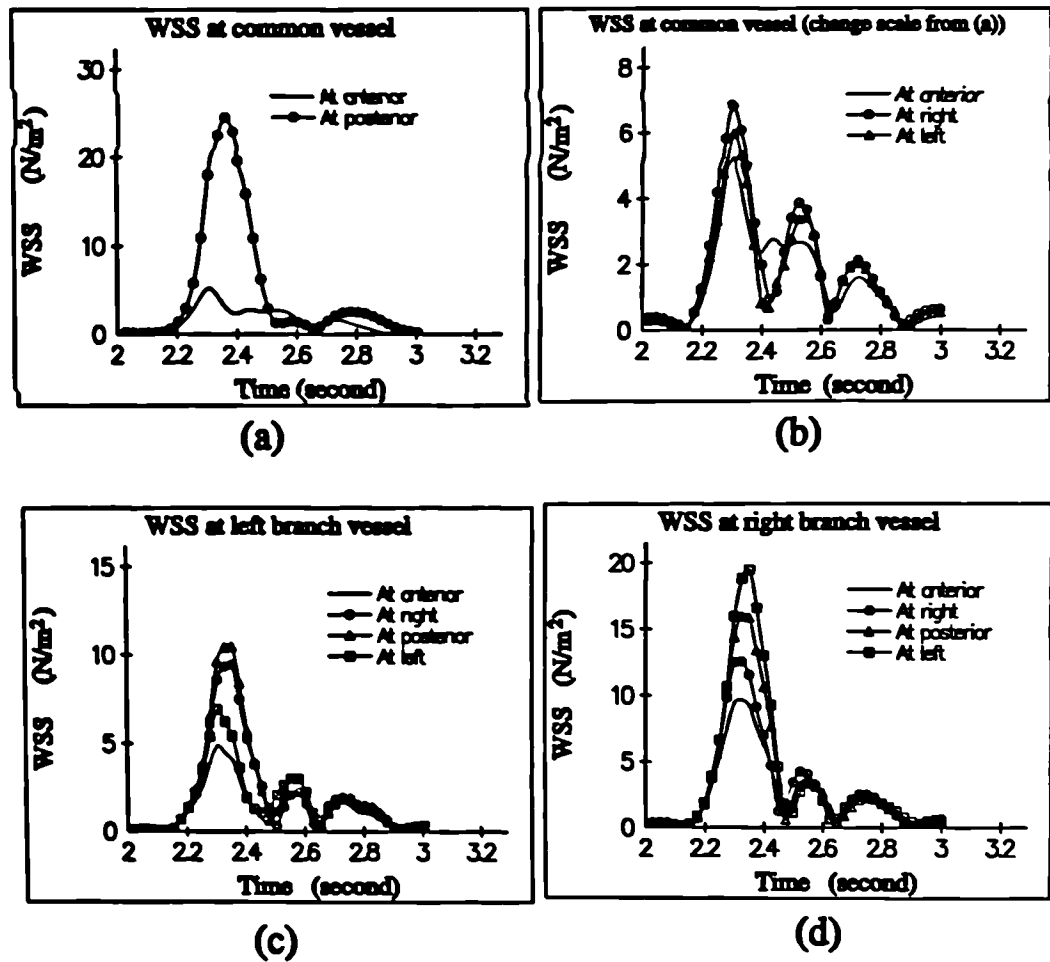
Figure 6.11: The WSS magnitude against time in one cardiac cycle at four points around the chosen planes. (a) On plane B, (b) still on plane B but with a finer scale to show in more details of WSS at the anterior, left and right points. (c) on plane C, and (d) on plane D.

To examine the WSS variation during the whole cycle, magnitudes of WSS at four points on planes B, C and D are plotted vs time (Figure 6.11). From Figure 6.11(a) and (b), it can be found that the peak value of WSS at the posterior point is significantly higher than that at the anterior point in systole. If we go back to the geometrical model in Figure 6.1(c), it can be noticed that there is a large slope on the posterior surface (in the bifurcation region) which forms a contraction in the region, while the surface at the anterior side is much smoother region, this geometrical feature may be the reason of higher WSS in posterior than in anterior. The shape of the surface may come from the curvature in the common vessel, however, the exact quantities are influenced by the interpolation parameters in the reconstruction of the flow division patch (see in section(3.4.2.2)). There is no significant difference in the reverse flow and diastole phases for the WSS at the posterior and anterior points in plane B.

Comparing the two branch vessels, WSS on the right side is slightly higher than on the left. It can also be found in Figure 6.11(c) (left branch) that $WSS_{right} > WSS_{left}$ in systole phase and it reversed in reverse phase, that is $WSS_{left} > WSS_{right}$. The same thing happens in the right branch as well in Figure 6.11(d) (right branch).

6.3.3 Summary of the CFD predictions for the abdominal bifurcation model

Main flow characteristics found from this case study may be summarized as follows:

- 'Plug' flow was observed in the whole flow domain during acceleration phases which would 'wash out' the blood in the domain.

- No significant flow separation was evident in the bifurcation region.

- From velocity contour plots it could be noted that even a mild curvature could result in asymmetric flow patterns in the branches. High velocities occurred between P and R in the left branch and P and L in the right branch during flow deceleration phases due to the non-planar effects.

- Velocity profiles had opposite features during the forward and reverse flow phases (a high velocity region in the forward flow phase turned to be a low velocity region during the reverse flow phase, and *vice versa* for low velocity regions). WSS patterns followed this change in velocity distributions. Therefore, there were no permanent low or high WSS zones at this bifurcation.

- Because of the curvature in the abdominal aorta, The WSS distribution along the circumference of planes B, C and D changed significantly. Higher WSS was found at the posterior side and lower WSS happened at the anterior side. Most of the WSS test points experienced both a relatively high WSS and low WSS during a cardiac cycle, indicating that there were no permanent low or high WSS zones in this model.

6.4 Validations

CFD validations are carried out in two main parts. Firstly, computational uncertainties are assessed by (A) the internal validation and (B) the uncertainty test of assumption of boundary condition setting. The internal validation has been achieved by testing the CFD predictions at different grid density (spatial resolution) and time steps (temporal resolution). To test the uncertainties of assumption of boundary condition setting, an extra CFD simulation has been done in which the entrance plane in the common vessel is set as INLET boundary with measured velocity profiles and mass flow boundary conditions are used at the two exit planes in branch vessels. Comparisons are carried out between the CFD predictions obtained with different sets of boundary conditions.

Secondly, comparison is made between the CFD predictions and *in vivo* measured velocity data. To validate the overall CFD predictions for the model, velocity profiles are measured by MR 2D Cine PC techniques at plane A in Figure 6.5. Comparisons of predicted velocity contours and measured velocity contours are made at different phases in a cardiac cycle.

6.4.1 Part 1: computational error assessment

6.4.1.1 Grid resolution and temporal resolution tests

The grid resolution test was designed according to the nature of the grid itself. The idea is to use a higher grid density in regions where high gradients of flow parameters are expected. If the grid parameters K, I, J represent the grid number in the model axial direction, circumferential direction and radial direction in the grid plane respectively, then the highest grid density happens in I direction and the lowest grid density happens in K direction. The grid resolution test will test the density changing effects in low density directions. Four different grid parameter combinations are used to generate grids in the model for the test.

Seven independent grid parameters are needed to generate the structured grid in the bifurcation model. They are: $K_{com}, K_{left}, K_{right}, NI, NJ, B_{axial}$ and B_{radius} which give the grid distributions in the axial direction along the common, left branch, right branch vessel, number of grid in the circumferential and radial directions, and non-uniform grid distribution parameters in the axial and radial directions respectively. Although grid distribution along the radial direction will influence the accuracy of WSS calculation, because of the non-uniform grid distribution along radial direction, the grid resolution near the wall in the radial direction is generally higher than 0.15mm which is significantly higher than grid resolution in other directions. Therefore, the grid resolution test was designed to test the distribution variations along the axial and circumferential directions, as follow:

- $K_{com}-15$, $K_{left} = 20$, $K_{right} = 20$, NJ=6, NI=24, $B_{axial}=1.05$ and $B_{radius}=1.30$. This forms a low density grid named *Low*. It gives a total of 9900 cells and 15428 node points grid.

- $K_{com}-25$, $K_{left} = 30$, $K_{right} = 30$, NJ=6, NI=24, $B_{axial}=1.05$ and $B_{radius}=1.30$. This was the grid used in the study, here called *Normal*. It gives a total of 15300 cells and 23408 node points grid.

- $K_{com}=30$, $K_{left} = 40$, $K_{right} = 40$, NJ=6, NI=24, $B_{axial}=1.05$ and $B_{radius}=1.30$. This

forms a high density grid named $High_1$. It gives a total of 19800 cells and 30058 node points grid.

- $K_{com}=25$, $K_{left}=30$, $K_{right}=30$, NJ=6, NI=32, $B_{axial}=1.05$ and $B_{radius}=1.30$. This forms another high density grid named $High_2$. It gives a total of 21760 cells and 31328 node points grid.

CFD calculations have been carried out for three cycles for all simulations to minimize the influence of initial conditions. The cycle period is 1 second, therefore the x-axis in Figure 6.12 ranging from 2.0 to 3.0s corresponds to results obtained for the third cycle. Comparisons are carried out at three points on plane B in the common vessel for velocity, they are: at the centre point, the point which is of half-radius distance from the center towards to posterior side and a point near the wall at the posterior. Three points were chosen to compare the WSS. These are: one on plane B (anterior), one on plane C (posterior) and one on plane D posterior) in Figure 6.5.

The velocity comparison results for grid density test are shown in Figure 6.12. Identical predicted velocities are obtained at the central and half-radius points for different grid densities. However, at the near wall point, maximum velocities (V_{max}) vary slightly for different grid densities. Higher grid density seems to have a lower V_{max}. There is a 8.8% difference in V_{max} between the *Normal* grid and the $High_2$ which has the lowest V_{max} value. The difference in V_{max} between the *Low* grid and *Normal* grid is 12.7%, and only 4.4% between the *Normal* and $High_1$.

The results presented above show that near wall velocities are more likely to be influenced by the grid density, indicating that WSS may be more sensitive to grid density. Figure 6.13 shows the WSS comparison results for grid density test. Again, differences happen in the common vessel near the bifurcation region. In Figure 6.13(a), the difference of maximum WSS (WSS_{max}) between *Normal* and $High_2$ grid density is 6.3% and between *Low* and *Normal* grid density is 14.6%. Identical WSS curves can be found for the WSS on the chosen
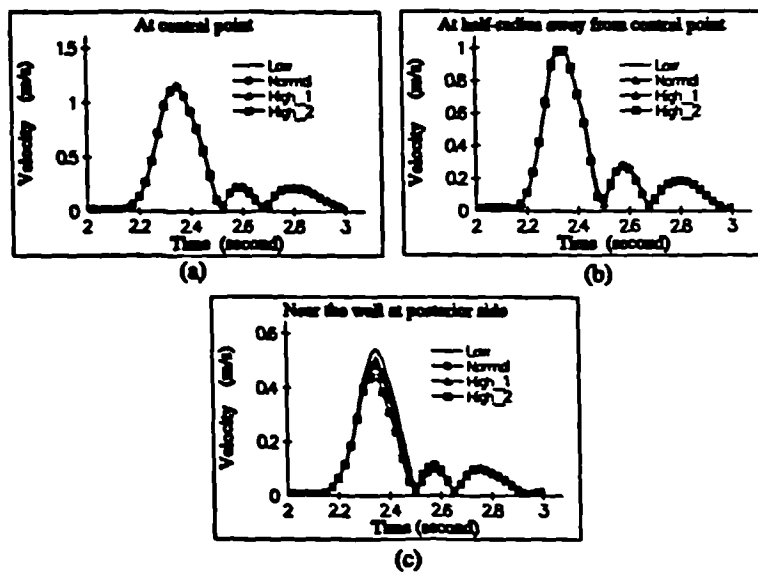
Figure 6.12: Comparison of velocities (magnitude) at three points on plane B in the common vessel for different grid densities. (a) velocities at the central point; (b) velocities at a point half-radius away from the center towards the anterior; (c) velocities at a near wall point on the anterior side.
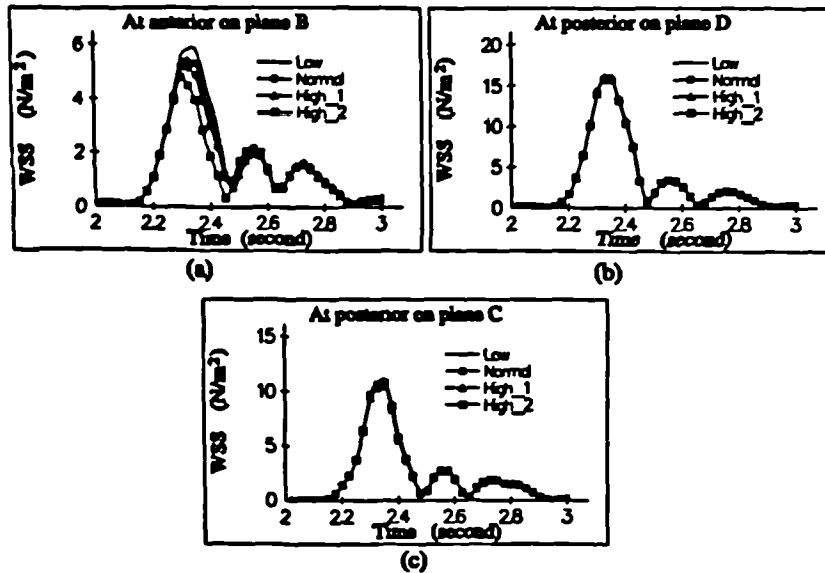
Figure 6 13: Comparison of WSS at three points. (a) at anterior on plane B; (b) at posterior on plane D (right branch ; (c) at posterior on plane C (left branch)

points in left and right branch vessels at different grid density. It is therefore concluded that *Normal* grid can give reasonably accurate CFD predictions.

The temporal resolution tests are carried out by changing the number of time steps in one cycle (*Nstep*) from the normally used 40 to 60 and 80 for the *Normal* grid density model. Figure 6 14 gives the comparison of velocity at a central point and a near wall point in the common vessel (close to the bifurcation region) for three simulations. The WSS comparison results at three points for three different *Nstep* are shown in Figure 6.15. Identical curves of velocities and WSS are found in the tests, indicating that WSS results are independent of the total time step if it is larger than 40.
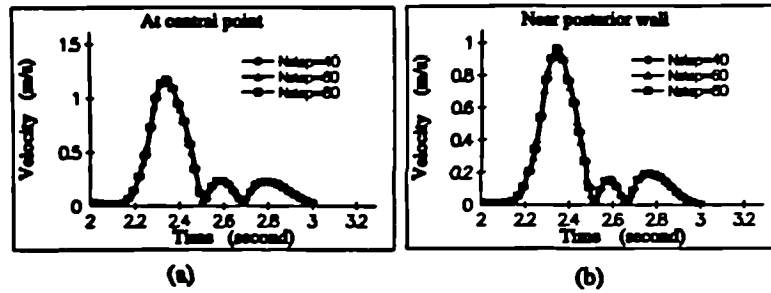
Figure 6.14: Comparison of velocities (magnitude) at two points in three different *Nstep* simulations. (a) at central point in the common vessel near the bifurcation region; (b) at near wall point in the common vessel close to the bifurcation region.
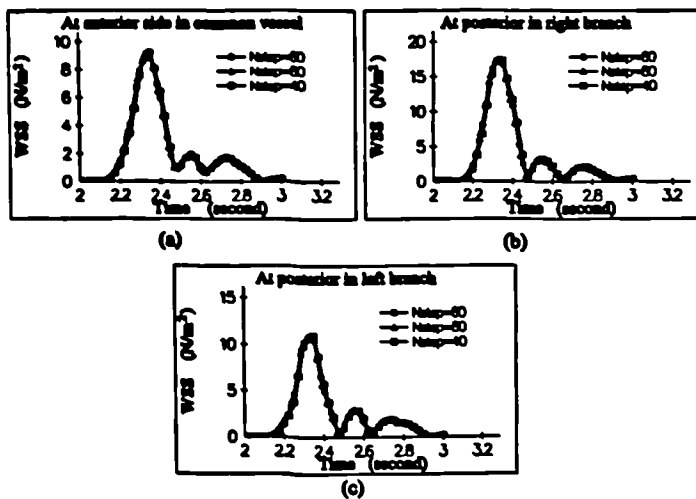

Figure 6.15: Comparison of WSS at three points in three different *Nstep* simulations. (a) at anterior on plane B; (b) at posterior on plane D (right branch); (c) at posterior on plane C (left branch)

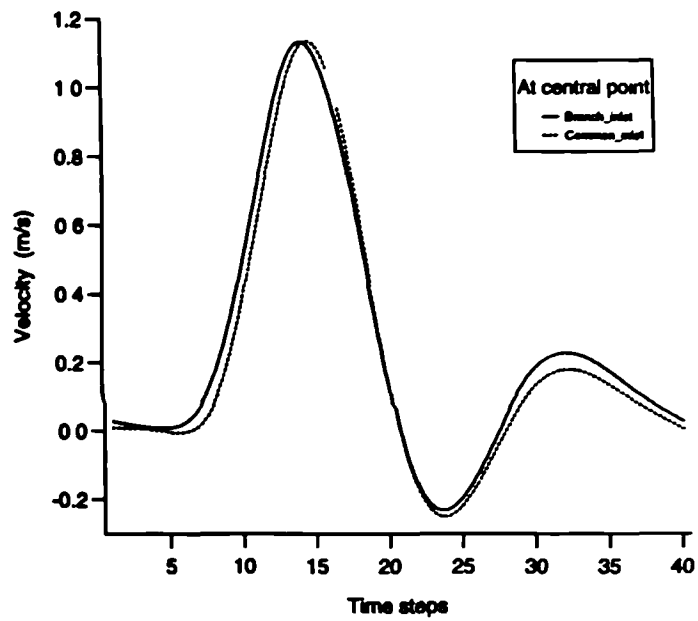### 6.4.1.2 Comparison with different boundary conditions

Boundary conditions used in the above CFD simulations have been discussed in section 6.2. Because the secondary flow at the branch exits cannot be ignored, velocity profiles (or Dirichlet boundary conditions) were prescribed at the two exits and a mass flow rate boundary condition (or Neumann boundary conditions) at the the entrance plane in the common vessel.

It is suggested in the CFX manual that this type of combination is for strongly diffusive flows where the user is sure that the outflow field is physically correct, say for example it is obtained from experiment. If the flow is convection dominated, and the outflow field is unphysical, the solution will display unphysical boundary layers normal to the outflow boundary (see section(5.4.1 . In the case investigated here, velocities at the model exits were obtained from MR measurement, therefore it is considered to be physically correct subject to measurement errors. On the other hand, the average Reynolds number is about 500, therefore, the outflow is convection dominated. To what extent the predictions are affected by the different boundary condition sets will be examined in this section.

In doing so, an additional CFD simulation has been performed. In this simulation, the '*Normal* grid' is used and the time-dependent velocity profiles are prescribed at the entrance plane in the common vessel and mass flow boundary conditions are prescribed at the exit planes in the two branch vessels. The treatment of mass flow boundary is the same as in section(6.2). There are eight patches for the left and eight patches for the right branch exit according to the grid block structure. The time-dependent mass flow ratios among the 16 patches are calculated based on the measured velocity profiles. These time-dependent mass flow ratios among the sixteen patches are used as mass flow boundary condition.

Figure 6.16 gives the comparison of predicted velocity for the two simulations at two points in the common vessel (near the bifurcation region). It can be seen that the velocity predictions with the two different sets of boundary conditions are in reasonable agreement at the test

(a At central point
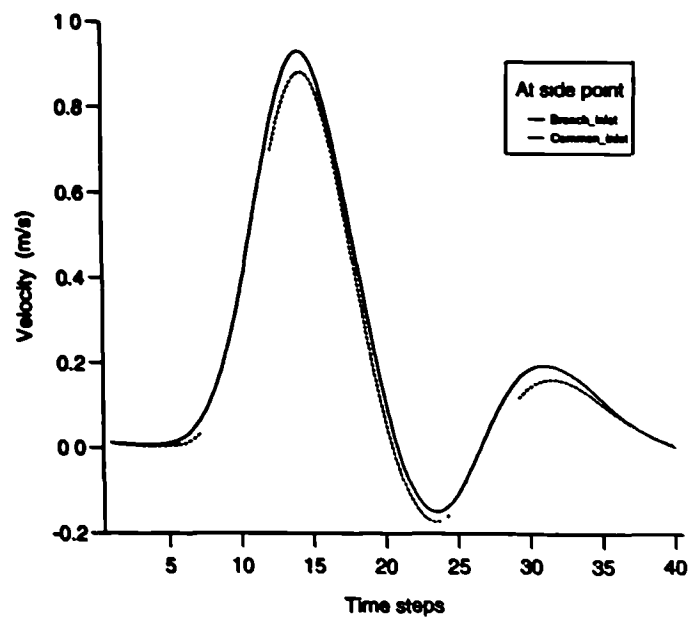
(b) Near wall point

Figure 6.16: Comparison of velocities for two simulations with different boundary conditions at two points in the common vessel near the bifurcation region.
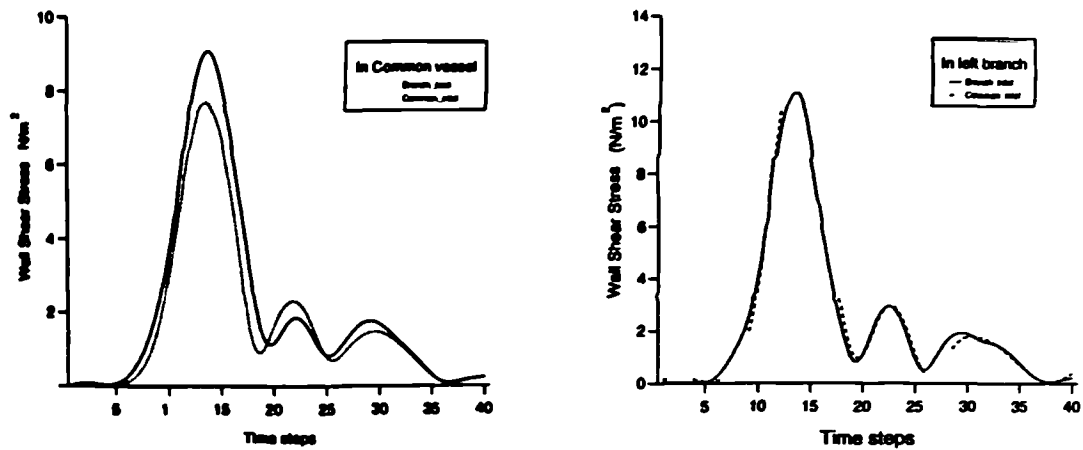
a common vessel, posterior

(b) left branch, posterior
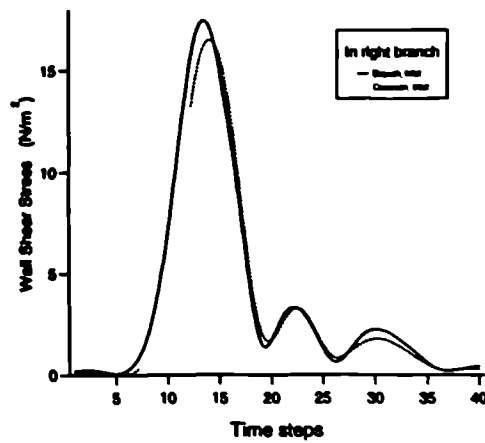
(c) right branch, posterior

Figure 6.17: Comparison of WSS between two simulations at three points on the posterior side. They are (a) in the common vessel posterior side near the bifurcation, and on the posterior side about one diameter downstream in the left (b) and right (c) branch vessels respectively.

points. The difference at the near wall point is 7.0% at peak flow phase.

However, the comparison of WSS in Figure 6.17 shows noticeable differences between the two simulations. Although both curves (WSS vs. time) are similar in shape, the differences at peak flow phase in the common, left and right vessel test points are 18.7%, 20% and 5.3% respectively. The WSS prediction in the old simulation (velocity profile at exits or branch-inlet) has a higher value in the common and right vessels and lower peak value in the left branch vessel than those in the new simulation (velocity profile boundary at entrance or common-inlet). In conclusion although the predicted velocities are in a good agreement between the two simulations, WSS still show marked differences especially in the left branch vessel. It is difficult to say which boundary condition gives more accurate results. Considering it is more likely to introduce errors in branch vessel velocity measurement and the natural situation of the flow, the use of the old set of boundary conditions (branch-inlet) should be very carefully limited.

6.4.2   Part 2: Overall CFD simulation validation

6.4.2.1   Comparison with MR measured velocity profile in the abdominal aorta

The overall validation of CFD predictions is carried out by comparing the CFD predicted velocity contours with the MR measured velocity results at a chosen plane in the common vessel, the plane A in Figure 6.5. The MR scan sequence and image processing programs used to generate the velocity information are the same as those used in generating velocity boundary conditions in Chapter 4. Comparisons are presented by drawing velocity contours at different phases in a cardiac cycle. To show the velocity variation during a cycle, velocity vs time curves are plotted at a number of chosen points in the plane.

Figure 6.18 give the comparison of velocity contours between measurements and CFD predictions at different time steps. The contour patterns agree reasonably well after flow decel-

(a) Flow acceleration   (b) Flow deceleration   (c) Early reverse flow

| velocity (m/s) |
5	0.8143
4	0.6107
3	0.4072
2	0.2036
1	0.0000

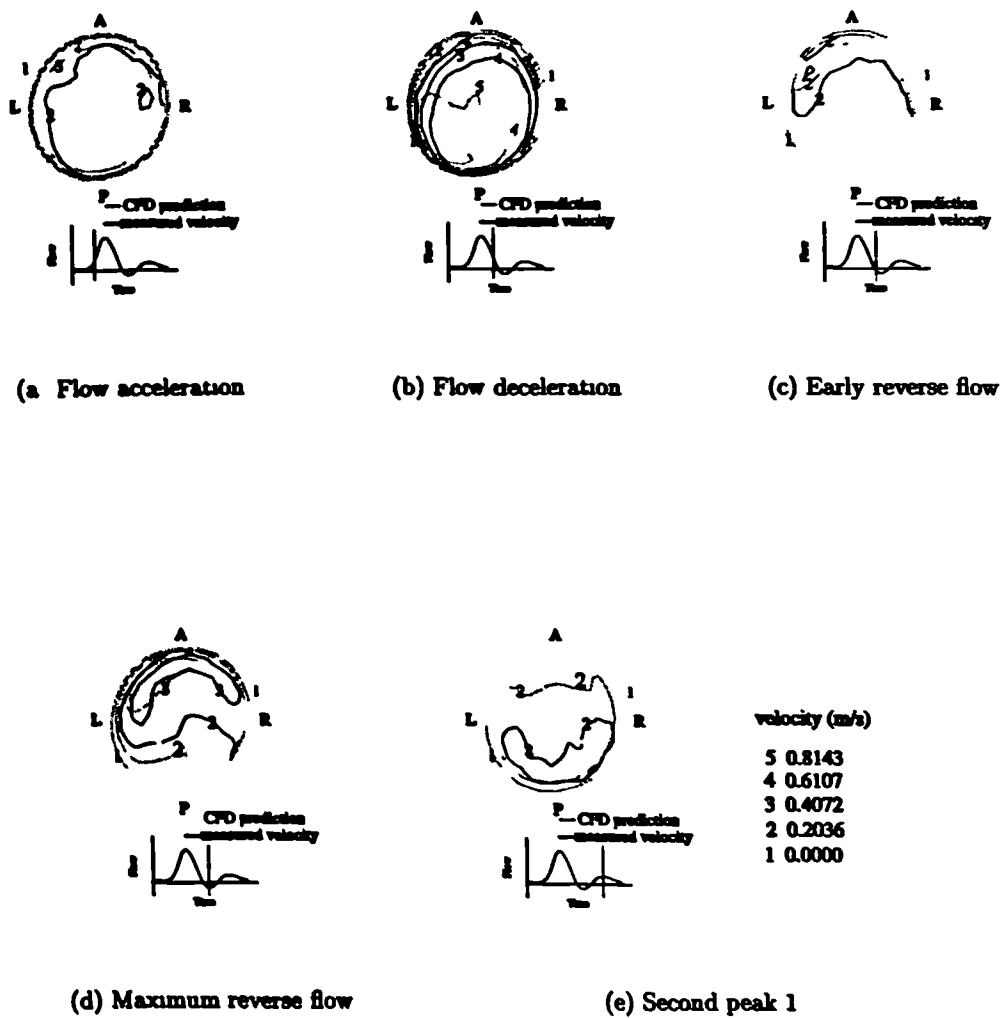(d) Maximum reverse flow   (e) Second peak 1

Figure 6.18: Comparison of velocity contours between MR measurement and CFD predictions at different time phases in a cardiac cycle.

eration as shown in Figure 6.18(c), (d) and (e), although quantitative values may differ. The comparisons of velocity variation with time during the cardiac cycle between the measurement and predictions, are shown at five different spatial points at plane A in Figure 6.19. Figure 6.19(f) defines the point locations. Predicted velocities are generally higher than the measurements. Marked differences are noticed at the systolic peak. In both measured and predicted results, 'plug' flow patterns exist during most of the systolic flow acceleration phases.

Because of the partial volume effect in MR velocity measurement, near wall velocity values are not very reliable, thus the very near wall point is not chosen in the validation test. Again, the predicted velocities show good consistency with the measured values during the second and third waves (here the second wave represents the back flow phase). Nevertheless, differences exist during the systolic flow acceleration and deceleration phase. The maximum velocities differ by 17.7%, 25.7%, 51.8%, 3.2% and 23.8% at the posterior, anterior, left, right side and central points respectively. It can also be noticed that there is a small time lag between predicted and measured maximum velocity especially in Figure 6.19(a), (d) and (e). The measured results are one time step (about 25ms) later than the predictions.

6.4.2.2 Assessment of uncertainties in the overall validation

The comparisons show that the velocity profiles are qualitatively similar between the CFD predictions and MR measurement. However, quantitatively, there are differences between them. One major source of the difference may come from numerical simulation errors and, as have been seen, physical model assumptions such as rigidity of the wall. The aim of the validation is to quantify this uncertainty. On the other hand, measurement errors also contribute to the difference, and sometimes they may overtake those of the numerical simulation. Therefore, it is necessary to assess the uncertainties in MR measurement.

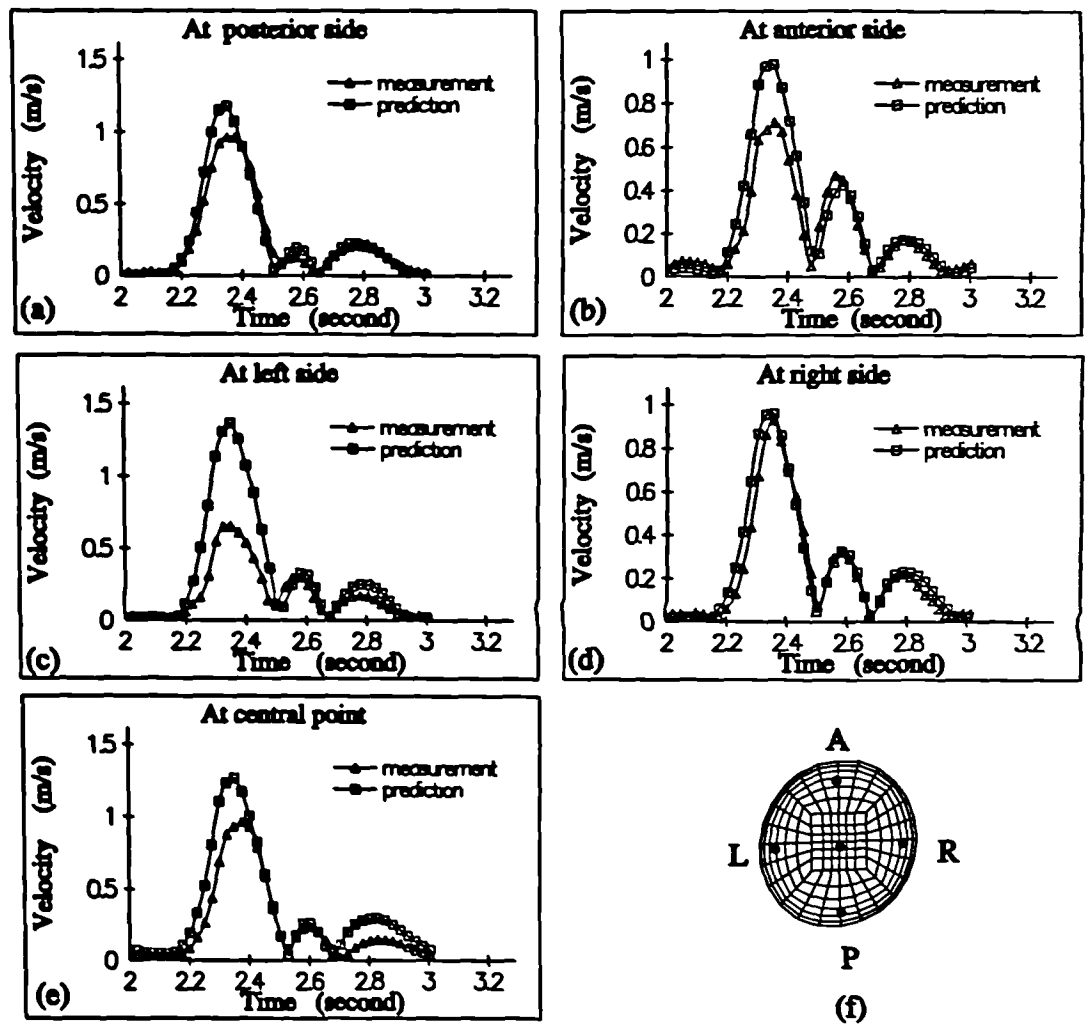From the nature of data generation, the uncertainties in MR measurement should come from

Figure 6.19: Comparison of velocity magnitudes for MR measurements and CFD predictions at chosen points.

(a): velocity measurement, and (b): velocity image processing.

Uncertainties in MR in vivo velocity measurement

There are many factors which can cause errors in MR scanning, especially in MR velocity measurement. First of all, to obtain a good ratio of signal to noise, a typical MR Cine 2D PC scan normally has a large slice thickness ($\geq 5mm$). The measured velocity value in each pixel is actually the average value of spin in the whole volume of the voxel. If the slice is not perpendicular to the vessel axis, which is a frequently encountered problem in measuring velocity in bifurcation branch vessels, the partial volume effect will result in significant errors in vessel boundary definition. It will either overestimate the ROI area or underestimate the velocity value in the boundary pixel. Other factors such as complex flow, and ECG gating technique may introduce additional errors in MR velocity imaging. A detailed MRI measurement error analysis can be found in a recent review by the author [192].

Uncertainties in MR velocity image processing

As described in section 2.2.4, a MR phase image normally has a very low ratio of signal to noise especially in slow flow region. For example, a frequent situation is the (qualitatively) near-zero velocity for the flow at a vessel boundary. A good quality magnitude image can always help to segment the phase image. However, in some cases, even a magnitude image cannot satisfy the segmentation conditions.

The scan sequence used in this study only allows one velocity component to be measured in one scan. To obtain a velocity vector, three separate scans are needed which take approximately 45 minutes (15 minutes each). During the scans subject movement is unavoidable. Vessel wall location will not, therefore, remain in the same pixels for the three velocity component phase images at the same time point. Therefore, *an accurate registration of three component phase images is critical to obtain a reliable result.*

A mislocation of the vessel wall for one velocity component will cause misregistration of velocity vector when the three velocity components are combined, yielding a wrong result. Because of random noises in the MR image, there is no fully automatic image segmentation technique which can ensure an accurate output result without close checking. Careful operator-checking of the segmentation result may help to minimize errors, and this can be facilitated by a graphic user interface, specifically designed to maximize ease of use.

6.4.3   Summary of the validation

The validation has been carried out in two parts. In the first part, computational uncertainties have been discussed. It is found that for the bifurcation geometry concerned, the *normal* density grid which was defined in section(6.4.1.1) and used in the study is sufficient to produce reasonably accurate predictions. Although modern workstations are capable of handling problems with much higher grid density, the demand in storage space will be huge. The dump file for the *normal* grid with 40 time steps is already over 50Mbyte, and it is about 80Mbyte for the $High_2$ grid. A huge dump file will cause difficulties in post-processing. The temporal resolution test shows that 40 time steps in one cycle is enough to follow the pulsatile flow.

The choice of boundary condition is another very important factor which may influence the final predictions. Normally *Inlet* boundary condition should only be used at the entrance. In cases where velocity profiles are specified at the exits as in the study, results need to be checked carefully.

The overall CFD prediction validation has been achieved by comparing the MR measured velocity with CFD predictions. Qualitatively, the velocity contours agree very well between them. However, quantitative differences are found especially at the first peak velocity phases. Various factors that may attribute to the observed difference have been discussed.

6.5 Conclusion

The complete set of methods of the combination of MRI and CFD developed in preceding chapters have been tested in an *in vivo* human abdominal-iliac bifurcation.

Comprehensive CFD simulations for the bifurcation model were carried out. The time-dependent velocity and WSS distributions for the model were presented. It was found that even a small curvature in the abdominal aorta (superior to apex) would cause asymmetrical flow patterns. Because of the nature of the flow waveform, velocity and WSS have opposite features during the forward and reverse flow phases, therefore, there is no permanent low or high WSS zone in this bifurcation model during a cardiac cycle.

To prove the stability and the reliability of the method, the validation has been carefully designed to include both numerical accuracy tests and overall validations. In the latter, an attempt was made to compare the CFD predicted velocity contours with the MR measured velocity contours at a cross-sectional plane in the abdominal aorta. The results showed a generally good agreement between the calculations and the measurement though local discrepancies still exist. The source of these discrepancies came from the MR velocity measurement, image processing and numerical errors.

Chapter 7

CFD predictions case 2:

a human carotid bifurcation

7.1 Introduction

The human carotid bifurcation is another very important site for haemodynamics investigation. Because of the area expansion at the entrance to the internal carotid (bulb), blood flow becomes very complicated in this region. The most important fact is the development of artherosclerosis. Carotid aneurysm is another life-threatening disease at the carotid bifurcation because of the blood flow behaviour. In haemodynamic research the carotid bifurcation is one of the most popular models and has been studied by numerous researches. Hydrogen-bubble visualisation experiments were used by Palmen et al [193] to visualize the flow in stenosed carotid bifurcation models. Anayiotos et al [194] used a single component Laser system to measure velocity distribution in carotid bifurcation models with both compliant and rigid wall to examine the influence of wall movement. Numerical simulation techniques were used by Perktold et al [195, 196] to study the flow patterns as well as the stress distribution on the wall in the carotid bifurcation region. Lee and Chiu [197] also used numerical methods to study the intimal thickening as a function of shear in carotid bifurcation. Although the internal carotid sinus was commonly considered in these studies, most of the models used were simplified in geometry. In this chapter, a comprehensive CFD research on an *in vivo*

175

human carotid bifurcation is presented. Validations were undertaken by grid resolution tests and comparison with MR measured velocity profiles in the common carotid. Furthermore, the effects of different boundary condition settings are discussed.

7.2　Model geometrical description and boundary conditions

The model was obtained from the right carotid bifurcation of a 40 years old healthy male volunteer. The 3D geometry reconstruction is shown in Figure 7.1(a), (b),(c) and (d) at different view angles. The original position (scan position) of the bifurcation is shown in Figure 7.1(a). However, for the convenience of following presentation, it was rotated by an angle so that the bifurcation plane is located in the coronary plane as shown in Figure 7.1(b) where the internal carotid artery (ICA) is on the left and the external carotid artery (ECA) on the right. The orientation parameters are defined in the figure, so that: posterior to anterior (P A) (shown in Figure 7.1(d)), left to right (L/R), inferior to superior (I/S) coincide with the Cartesian coordinate system positive directions of x-axis, y-axis and z-axis respectively. The orientation description parameters such as L/R, P/A and I/S used in the following discussion will be the same as those defined in Figure 7.1(b) and (d).

Viewing the model from different angles, it can be found that there is a curvature in the common carotid artery (CCA) towards the anterior side. The cross-sectional area expands rapidly at the end of CCA which eventually forms the internal carotid bulb. Under certain flow conditions, this sudden expansion may cause the flow to separate and reverse. Furthermore, the branch vessels are not only curved in the bifurcation plane but also have out-of-plane bending. In the ICA, following a bending towards the posterior-left in the bulb region, the vessel curves towards the anterior-right side. All these complex bendings may have a non-planar effect on the flow. The CFD study was aimed to provide the detailed fluid flow behaviour within this geometrically complicated model.
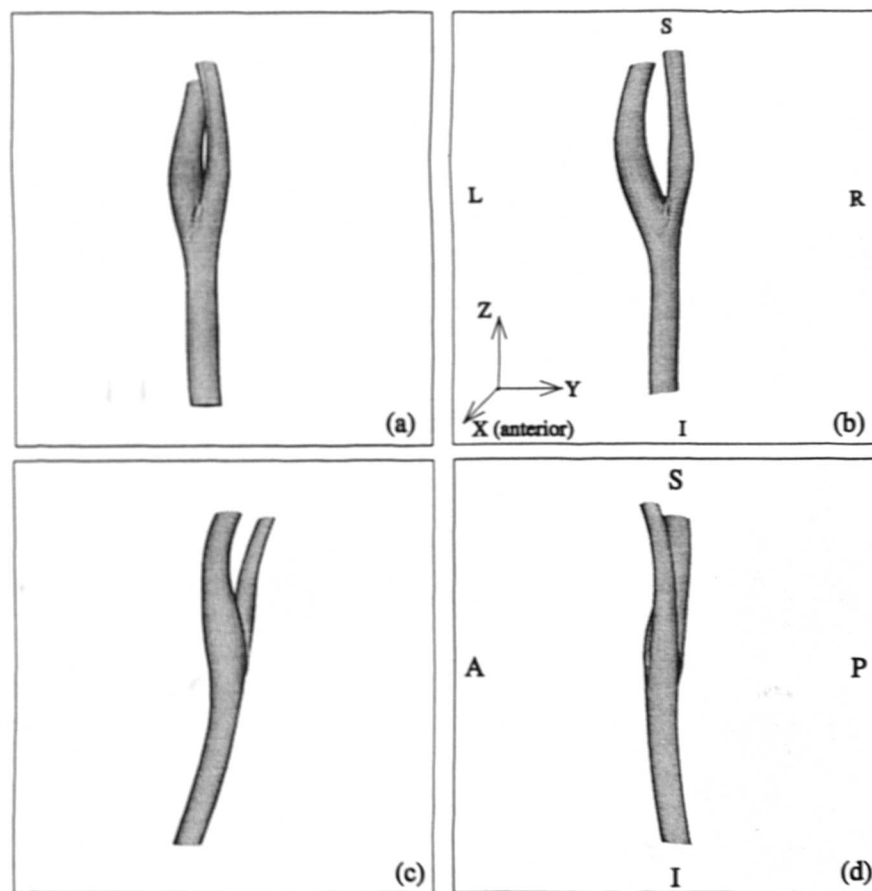
Figure 7.1: 3D geometrical model of the human carotid bifurcation, showing in different view angles. The definition of the orientation parameters are shown in (b) and (d).

We are essentially interested in the flow behaviour and WSS distribution in the common carotid and internal carotid vessels, especially the bulb region of the latter. Because of this, we have avoided some complexity, by ignoring any additional arterial branches in the external carotid when reconstructing the 3D geometry. A recent research carried out in our group showed that flow in the internal carotid would not be significantly influenced by ignoring those small vessels in the external carotid [198]. In this model, the common vessel and branch vessels have equal lengths. 3D velocity profiles were measured by MR PC techniques at one plane in the CCA (entrance to the bifurcation) and two planes downstream of the bifurcation apex in the ICA and ECA (exits of the bifurcation). The scan plane in the branch vessels is not perpendicular to the vessel axis and the ratio of spatial resolution to diameter is larger than in the common carotid, hence there is a larger partial volume effect, thus greater errors in branch vessel velocity measurements are likely to occur. In the CFD study, velocity profiles measured in the common carotid were used as the inflow boundary condition and mass flow ratio between the internal and external carotids as outflow boundary conditions. The effect of different boundary conditions on the flow will be discussed as well.

Figure 7.2(a shows the volumetric flow rate vs time curve derived from MR measurement at the common carotid entrance plane. It can be found that there is no reverse flow phase during the whole cycle. Following the first main peak wave caused by constriction of the heart, several small peak waves can be evidenced. Figure 7.2(b) shows the mass flow ratio between two branch vessels calculated from the measured velocity profiles. Under the *in vivo* pulsatile flow conditions (average heart beat rate 60/min), the average Reynolds number and Womersley parameter [1] are 300 and 4.3. Only laminar type flow is considered in the study because of the low Re number.

---

[1] defined as $Re = \frac{4Q}{\pi D \mu}$, where Q is the average flow rate in the common carotid vessel over a whole cycle.
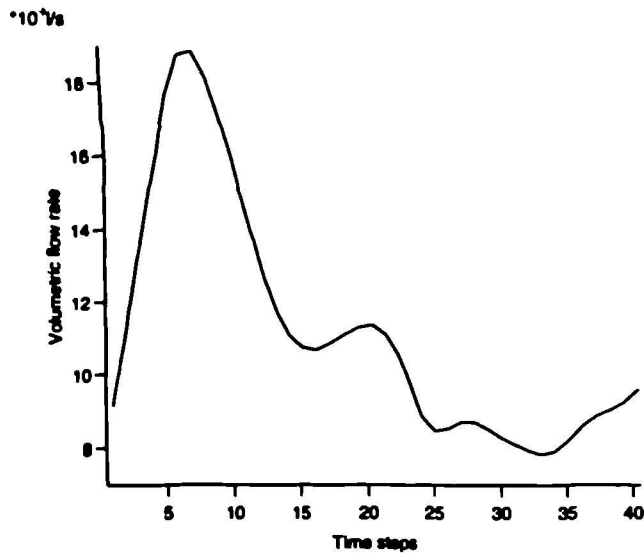
(a)
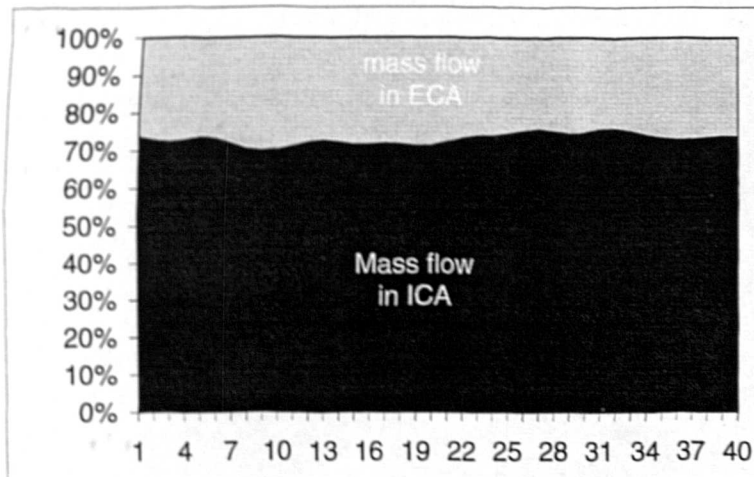
(b)

Figure 7.2: Velocity boundary conditions. (a): volumetric flow rate at the common carotid entrance plane; (b) time-dependent mass flow ratio between the two exit planes.

7.3 CFD Predictions

It is rather difficult to present the CFD predictions due to the non-planarity of the bifurcation and pulsatility of the flow. Although CFD calculations produced a complete set of haemodynamic data including velocity, pressure and shear stress distributions in the entire fluid domain during the whole cardiac cycle, only part of them are given here.

7.3.1 Velocity distribution

Three sets of serial figures are used to present the velocity distributions in the bifurcation model. Firstly, the velocity contours are plotted along the axial direction of the model to give an overall picture of the flow patterns at different time points (time step) in a cycle; Secondly, the 3D flow separation zone and its variation during the cycle has been demonstrated by a series of 3D plots; Thirdly, 3D velocity vectors including secondary flow patterns together with velocity contours are shown to focus on the local flow characteristics at several chosen planes of interest (bulb region).

Figure 7.3(a), (b), (c) and (d) show the velocity contours along the longitudinal direction at time steps 5 (mid-way of flow acceleration), 8 (first peak flow phase), 11 (mid-way of flow deceleration) and 20 (second peak flow phase) respectively. It can be found that the flow patterns do not change very much in branch vessels throughout the cardiac cycle. In the CCA, the high velocity region is skewed towards the back (L-P side) of the CCA curvature which is demonstrated more clearly in (c) and (d). This is due to the entrance velocity profiles, indicating that there may be another bending in the CCA inferior to the model. As expected, high velocity regions occur in the inner-wall of branch vessels (Right side for ICA), but after two diameters distance downstream, it has rotated to the anterior side in the ICA due to the out-of-plane curvature.

Another noticeable feature is that there is a relatively large space between the first and sec-

a at time step 5   (b) at time step 8

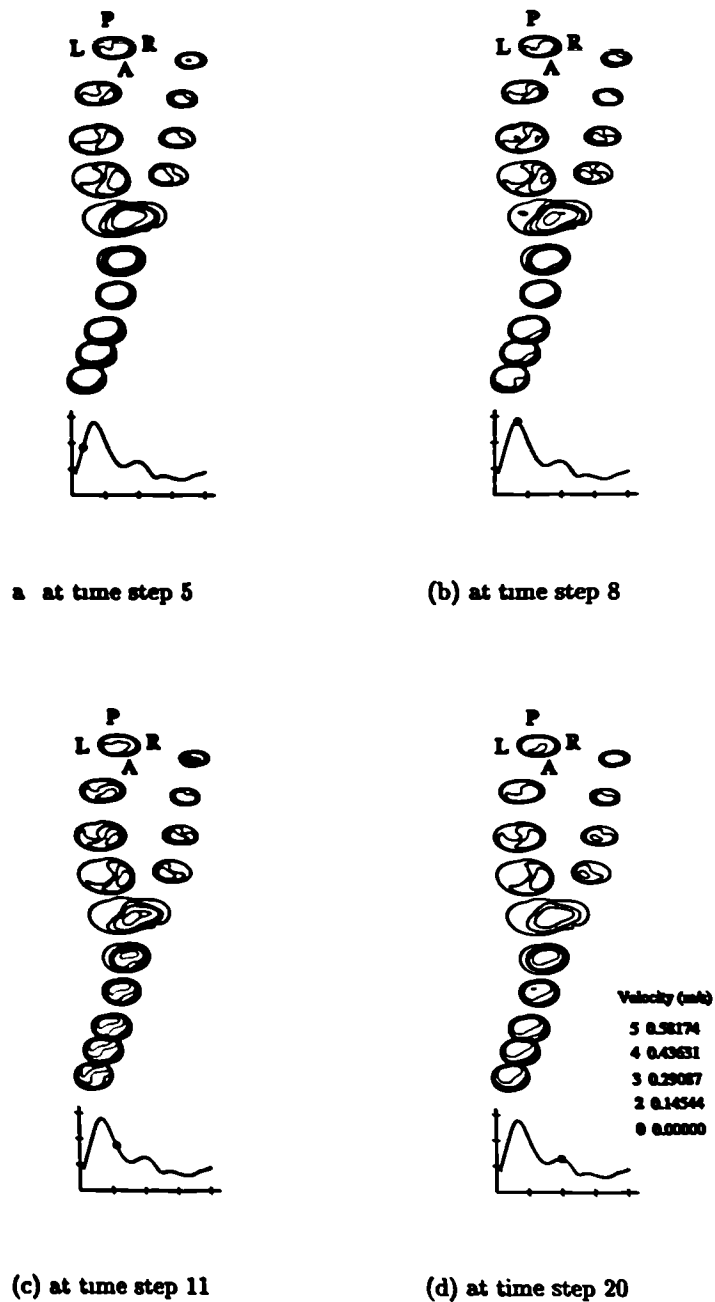(c) at time step 11   (d) at time step 20

Figure 7.3: Velocity distribution (contours) along the longitudinal direction at different time points in a cardiac cycle

ond level of contours in the bifurcation region and early part of ICA segment, suggesting that there is a large region of very low velocity (magnitude) and flow separation in this area.

Flow separation in the common carotid and internal carotid bulb is one of the most important flow features at the human carotid bifurcation. It is known that in the flow separation zone, fluid particles have very small forward or backward momentum. Because the model's longitudinal direction is in the Z-axis positive direction and the angles between vessels' axial directions and Z-axis are fairly small, the flow separation zones were approximately considered as the region with zero or negative V_z (velocity component in Z-axis). Figure 7.4 demonstrates the area where $V_z < 0.001$m s (in black) at the chosen planes. If the images are saved at each time step and played as an animation, the time-dependent flow separation zone can be clearly visualised. Here five images are presented at time steps 5, 8, 11 and 20 respectively. It is has been found that the black regions do not change very much from time step 20 onwards.

The following points are noted from further examination of the results:

- The flow separation is present throughout the cardiac cycle, and the volume of the flow separation zone changes during the cycle. It reaches the maximum in the flow deceleration phase (around time step 11). At this time, the region covers the vessel surface from 1.5 x CCA diameter inferior to the apex to 2.5 x ICA diameter superior to the apex.

- Because of the out-of-plane curvature in the bifurcation region, reverse flow regions are located at A-L side of the CCA and ICA and A-R of CCA and ECA.

- The percentage of cross-sectional area occupied by reverse flow can be as high as 40% at the entrance to the ICA where the strongest reverse flow was found. Further processing can be done to evaluate the change in volume of the separation zone during a cardiac cycle.
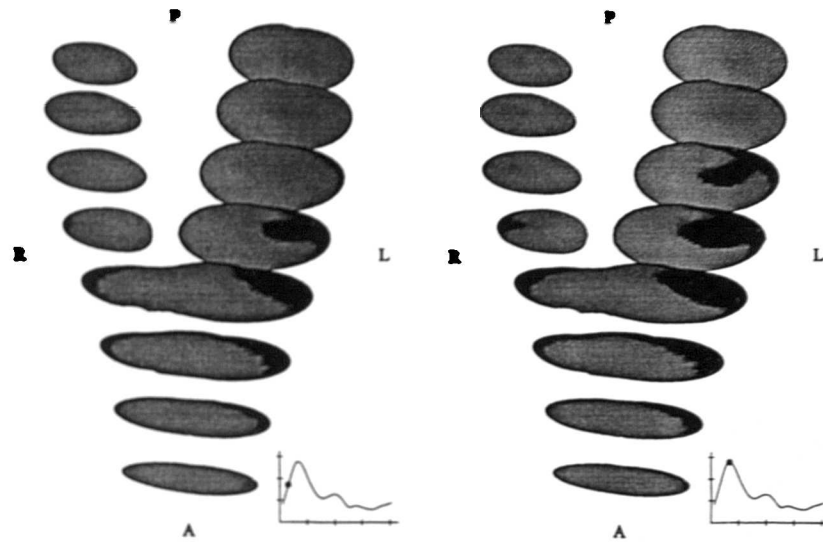
(a) at time step 5

(b) at time step 8
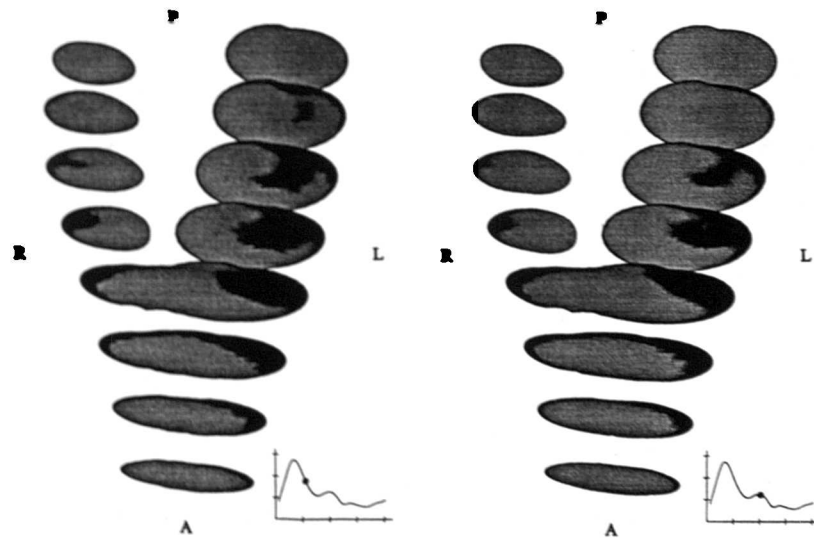
(c) at time step 11

(d) at time step 20

Figure 7.4: Flow separation zone in the bifurcation at different time points

To obtain a further understanding of flow behaviour in the CCA and ICA bulb region, more detailed flow patterns are presented by the velocity contours, secondary flow patterns and 3D vector drawing. Four planes are chosen in the model, these are planes 1 to 4 as indicated in Figure 7.5. Plane 1 is at the middle of common carotid which will give the entrance velocity profile to the bifurcation. Plane 2 is at the beginning of the internal carotid, planes 3 and 4 are one and two diameters down stream from plane 2 respectively. Velocity contours, vectors and secondary flows are shown throughout the cycle in Figures 7.6, 7.7 and 7.8.

Again, it is evident, from the 3D velocity vector plots along two orthogonal diagonal lines,
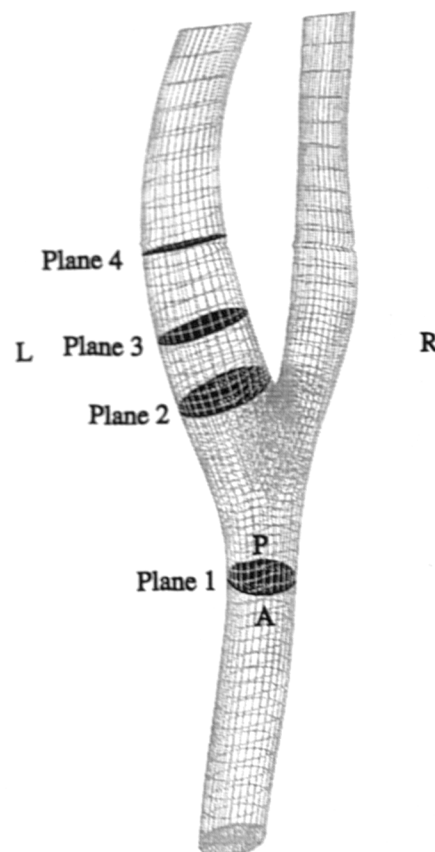

Figure 7.5: Locations of the chosen planes for the demonstration of velocity predictions
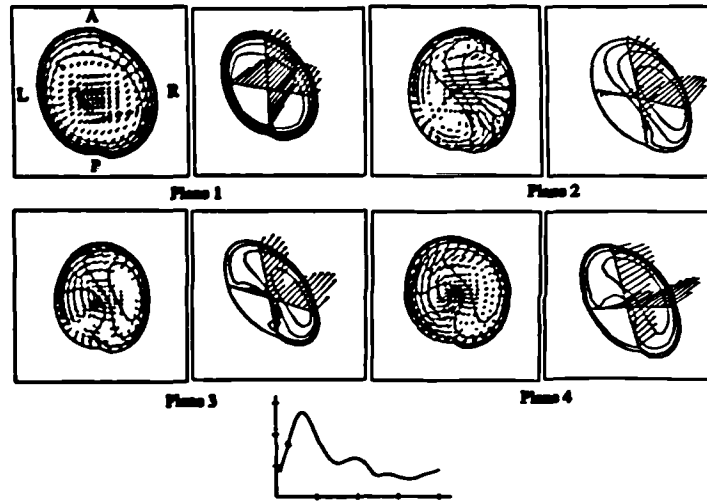
(a) at time step 5
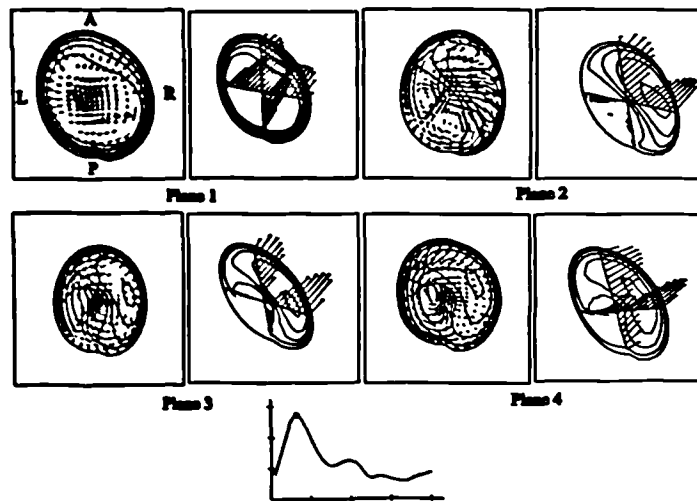
(b) at time step 8

Figure 7.6: Velocity distributions at four chosen planes during flow acceleration phases. For each plane, velocity contour and secondary flow are shown in the left, the same velocity contour and velocity profiles along two orthogonal diagonal lines are shown in the right. The same format is used in Fig 7.7 and Fig 7.8   185

(a) at time step 11
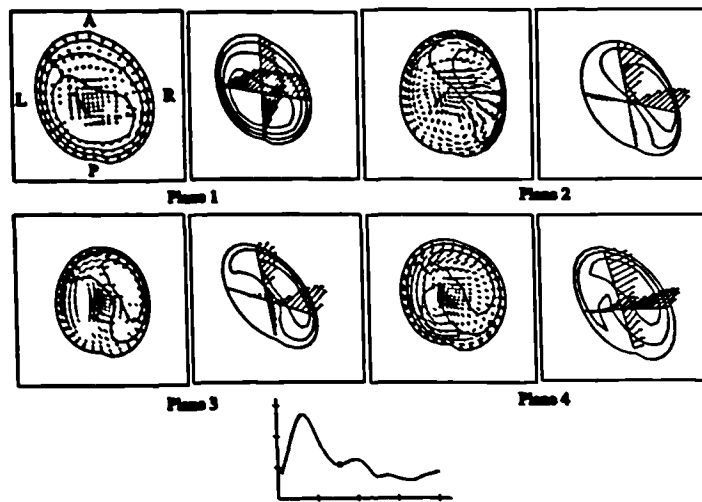
(b) at time step 16

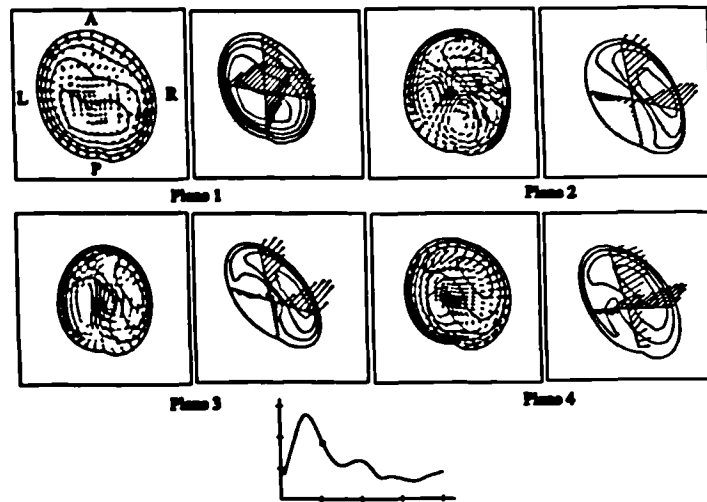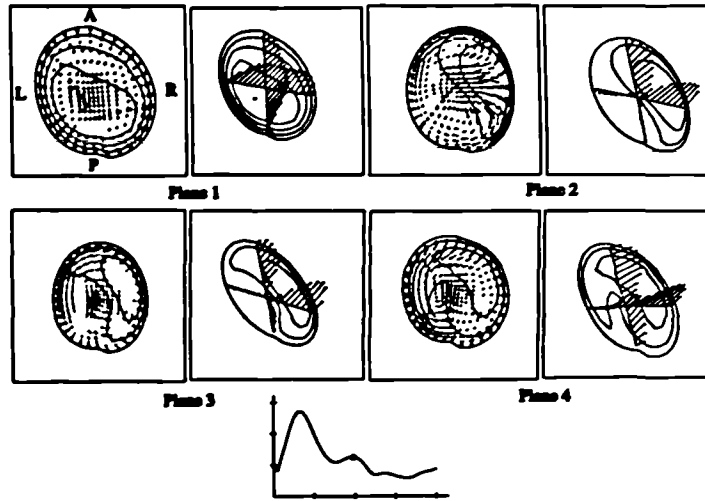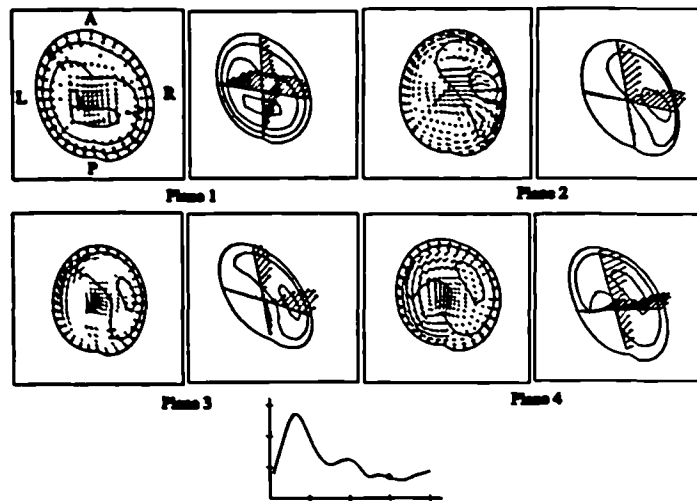Figure 7.7: Velocity distributions at four chosen planes during flow deceleration phases

186

a at time step 20

(b) at time step 30

Figure 7.8: Velocity distributions at four chosen planes during, and after the second peak flow.

that a large slow moving (or reverse flow) zone exists in the ICA bulb area (planes 2 and 3) throughout the cycle. Strong secondary flow can be found inside this zone. The in-plane velocity components are even larger than the axial component inside the slow moving zone (in plane 3) during most of the cycle.

In plane 2 (beginning of the ICA), If we name the vessel cross-sectional area occupied by reverse flow as the slow moving zone (or reverse flow), and the rest as the high velocity zone where fluid particles have high forward and overall momentum, the vortex separation line disappears in the high velocity region. An additional vortex appears at the anterior side in most of the cycle, because of the high forward momentum, this vortex may significantly influence the local flow pattern or particle tracks.

The posterior side vortex disappears in plane 3 after flow acceleration (time steps 8, 11 and 16 and reappears again after the deceleration phases (time steps 20 and 30). Secondary flow at plane 4 is dominated by a single vortex throughout the whole cycle. No reverse flow can be found in the plane so that from 3D point of view, a strongly forward spiral flow is developed here.

7.3.2 Wall Shear Stress distribution

Wall shear stress (WSS) is another very important feature of haemodynamics and still cannot be measured *in vivo* directly by current techniques. CFD simulation is able to provide 4D quantitative distributions of WSS in the study model. In this section WSS are shown by surface rendering contours (magnitude) at time steps 5, 8, 11, 20 from different view angles. The WSS magnitudes at four points in the CCA are also plotted vs time in Figure 7.9, where no directional information is given (no negative value) because the direction changes are very complicated here and cannot be simply described as positive or negative.

Figure 7.9 gives the WSS variations during the cycle at four points in plane 3 indicated in

Figure 7.5. As expected, the highest WSS value occurs at the right point (inner wall of the ICA). WSS at the anterior is higher than that at the posterior and left. The lowest WSS occurs at the posterior point where the most complicated waveform is found, indicating that WSS value oscillates rapidly with time at that part in the cycle. Another interesting point is that the peak WSS occurs at different time points for the four curves.

In Figure 7.10, the left-side figure is at the original orientation as in 7.1(b), and the right-side one gives a view from posterior direction (turning the left figure by 180). Comparing the left-side (or right-side) figure throughout the whole cycle, it can be found that there is no significant change in the WSS pattern during the cycle, only the value (contour number) change can be noticed. In the ICA, the low WSS value always occurs at posterior side in the bulb region. However, the high WSS value can be found at posterior side in CCA.
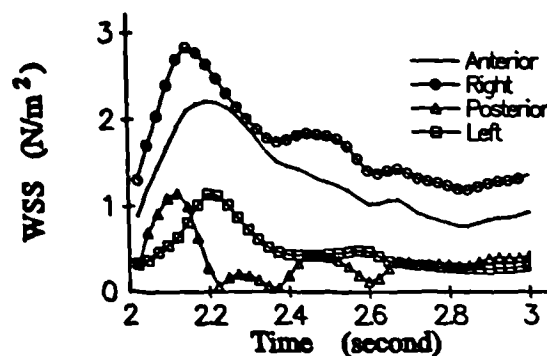
Figure 7.9: Wall Shear Stress (magnitude) during the cycle at four points in plane 3

189
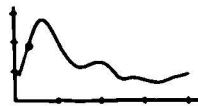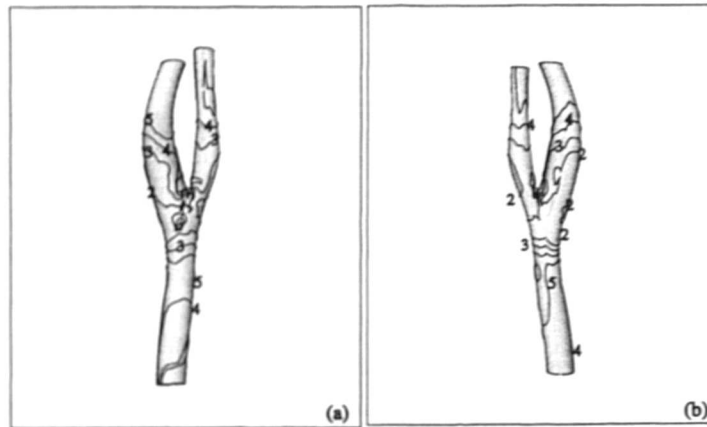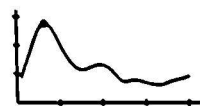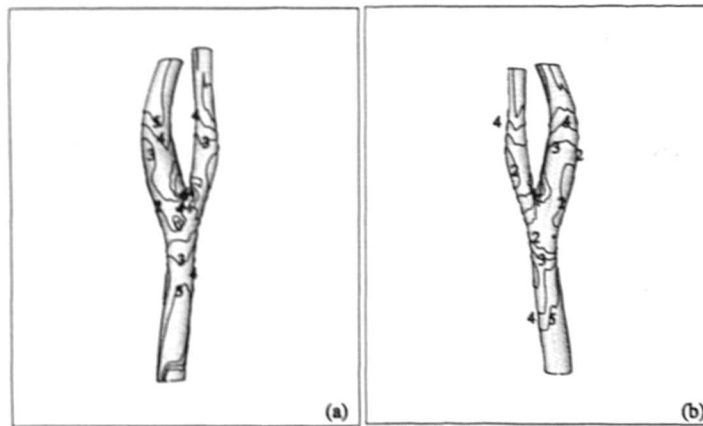
(a) at time step 5

5	5.097
4	3.823
3	2.547
2	1.274
1	0.000

Wall shear stress contour N/m^2

(b) at time step 8

Figure 7.10: Wall Shear Stress distributions in flow acceleration phases

(a) at time step 11

5 5.097
4 3.823
3 2.547
2 1.274
1 0.000   Wall shear stress contour N/m²
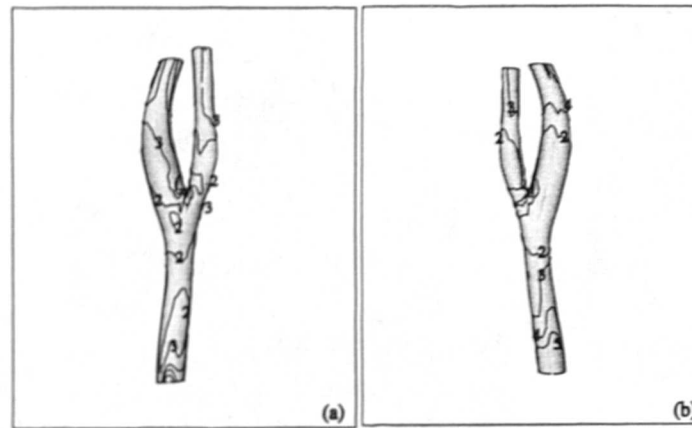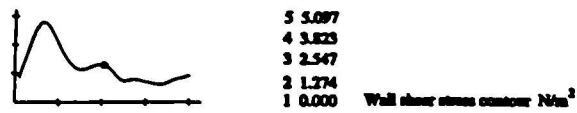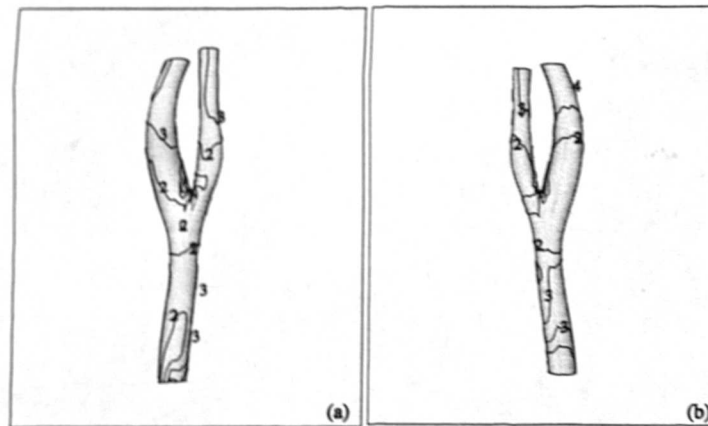
(b) at time step 20

Figure 7.11: Wall Shear Stress distributions in diastolic phases

7.4 Validations

The numerical simulation validations were taken by three steps for this study. In the first step, tests were designed to clarify the possible errors of numerical settings which included: (a) grid resolution and temporal resolution (different time steps in one cycle) and (b) boundary condition setting tests. In the second step, a CFD calculation was carried out by using the geometry model generated by different smooth parameters but with the same set of boundary conditions, to test the effects of the smoothing parameters specified in the geometrical model reconstruction on the final CFD predictions; In the third step, MR measured velocity profile on a common carotid plane (middle of the common carotid vessel in the model) was compared with CFD predictions at the same location. The velocity images were processed in the same way as in generating the velocity boundary conditions. To have a clear understanding of the effects of assumptions used in boundary conditions, a number of simulations were performed by using different combinations of boundary conditions.

7.4.1 Part one: numerical errors

7.4.1.1 Grid resolution and temporal resolution tests

To guarantee the CFD predictions are grid independent, the grid resolution test was designed to include four different grid densities. The grid parameters are varied firstly along the axial direction (K) and then in the circumferential direction (I).

Let K_{com}, K_{int} and K_{ext} represent the total number of cells in the axial direction in the common carotid, internal carotid and external carotid arteries respectively, I_{end} and J_{end} represent the total number of cells in the circumferential and radial directions respectively, the grid parameter combinations for four grid densities are:

- K_{com}=25, K_{int}=30, K_{ext}=30, I_{end}=32, J_{end}=6. It gives a total of 24320 cells and 34888 nodes in the whole flow domain, named Grid1.

- K_{com}=25, K_{int}=30, K_{ext}=30, I_{end}=24, J_{end}=6. It gives a total of 17100 cells and 26068 nodes in the whole flow domain, named Grid2.

- K_{com}−30, K_{int}=50, K_{ext}=50, I_{end}=24, J_{end}=6. It gives a total of 23400 cells and 35378 nodes in the whole flow domain named Grid3.

- K_{com}−25, K_{int}−30, K_{ext}=30, I_{end}=40, J_{end}=6. It gives a total of 32300 cells and 44492 nodes in the whole flow domain named Grid4.

Boundary conditions are identical for all four grid density models which have 40 time steps
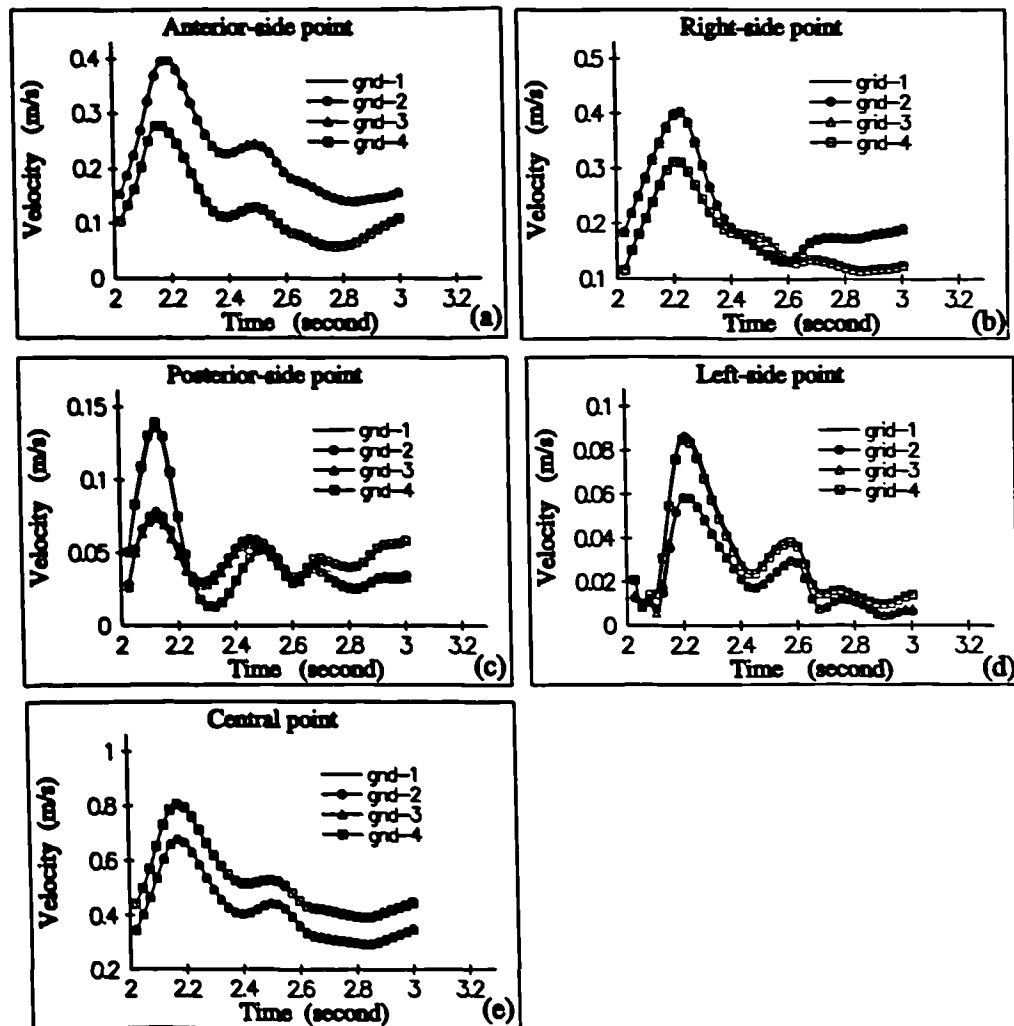
Figure 7.12: Comparison of the velocity magnitudes in four different grid-density models at five chosen points in a plane (one diameter inferior to apex) in the CCA
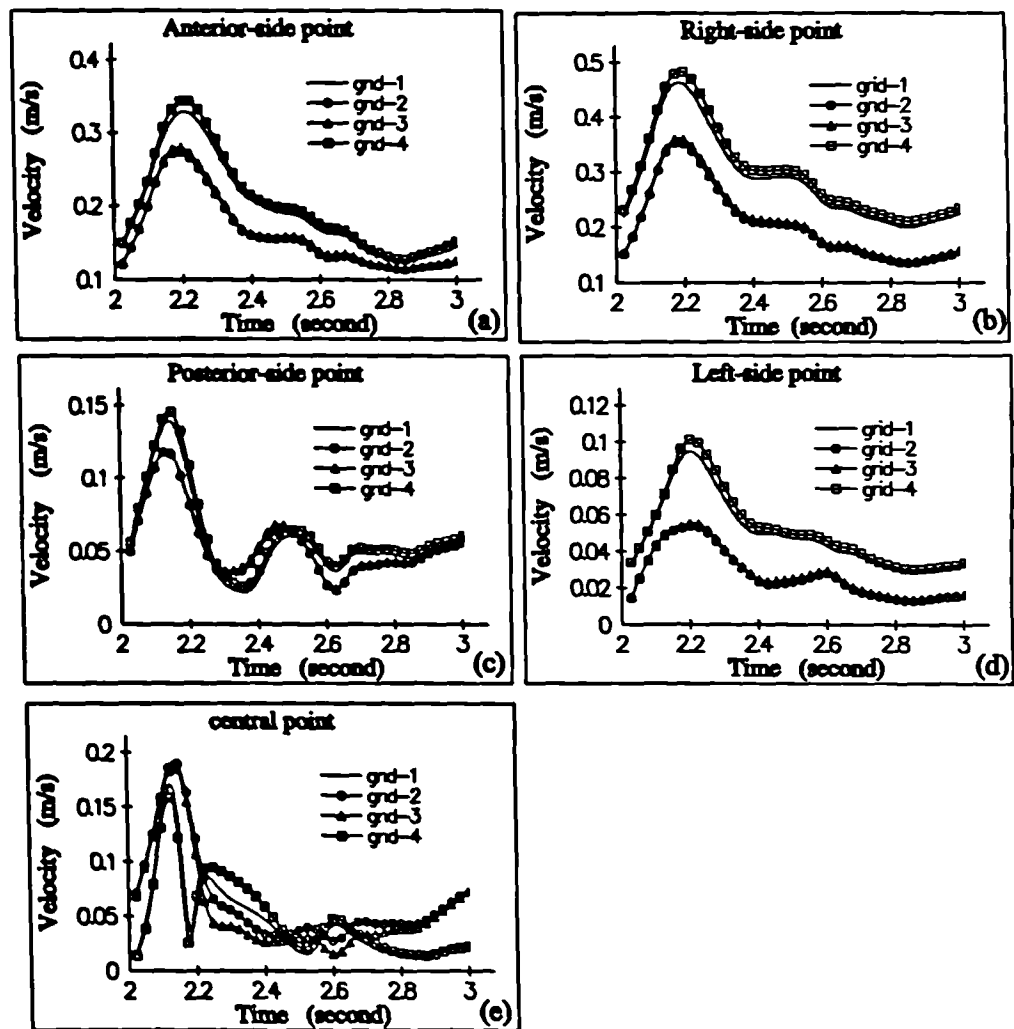
Figure 7.13: Comparison of the velocity magnitude in four different grid-density models at five chosen points in a plane (one diameter superior to apex) in the ICA
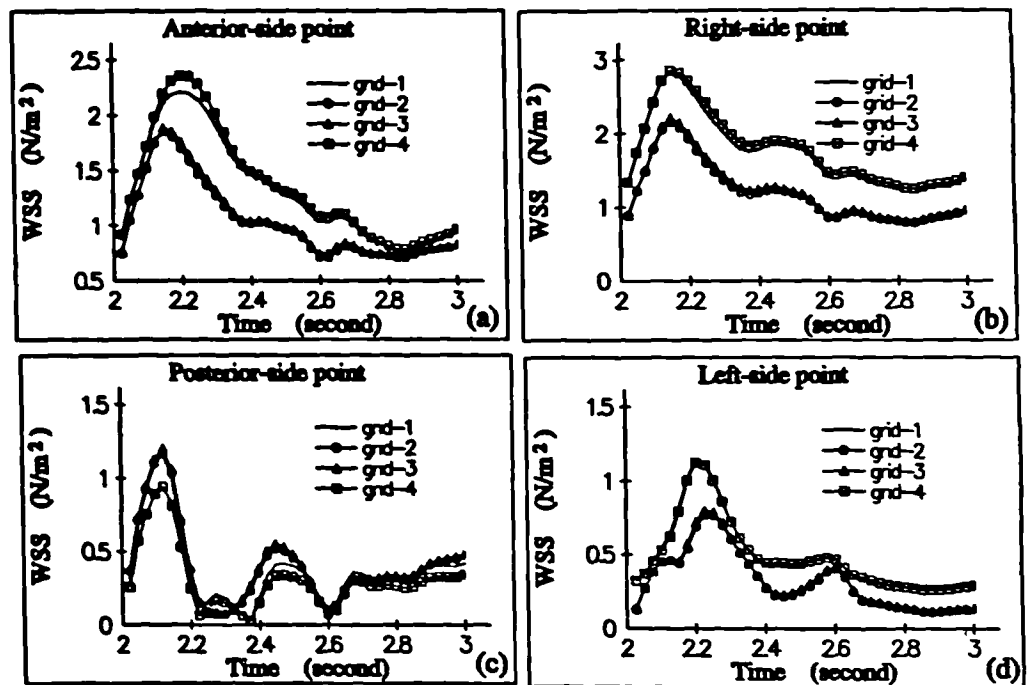
Figure 7.14: Comparison of the WSS magnitude in four different grid-density models at four wall points (anterior, right, posterior and left) in a plane (one diameter superior to apex) in the ICA

in the CFD calculation. The CFD predictions are processed by EnSight and the results are compared in Figure 7.12 and 7.13 for the velocity magnitude. In Figure 7.12, five monitor points are chosen to show the plot of velocity vs time for the four grid density models. Quantitative wall shear stress comparisons are shown in Figure 7.14 where four plots of WSS vs time are presented for four monitor points on the wall in the ICA.

The results show that the CFD calculations produce similar flow patterns between grid1 and grid4 models, between grid2 and grid3 models. The question then is which pattern is closer to the real solution. This will be addressed in the time resolution test to be discussed later.

Two sets of CFD simulations with different time steps have been carried out to test the effects of temporal resolution. Grid1 and grid2 models are used in the test. 40 time-step was
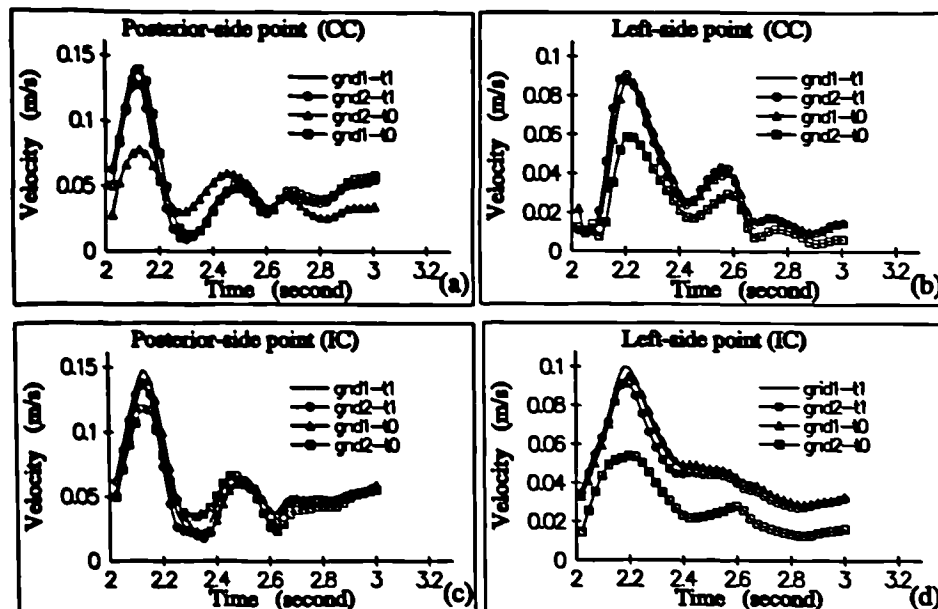
Figure 7.15: Comparison of the velocity magnitude in temporal resolution test at four near wall points (posterior, left in the CCA plane and posterior left points in the ICA plane)
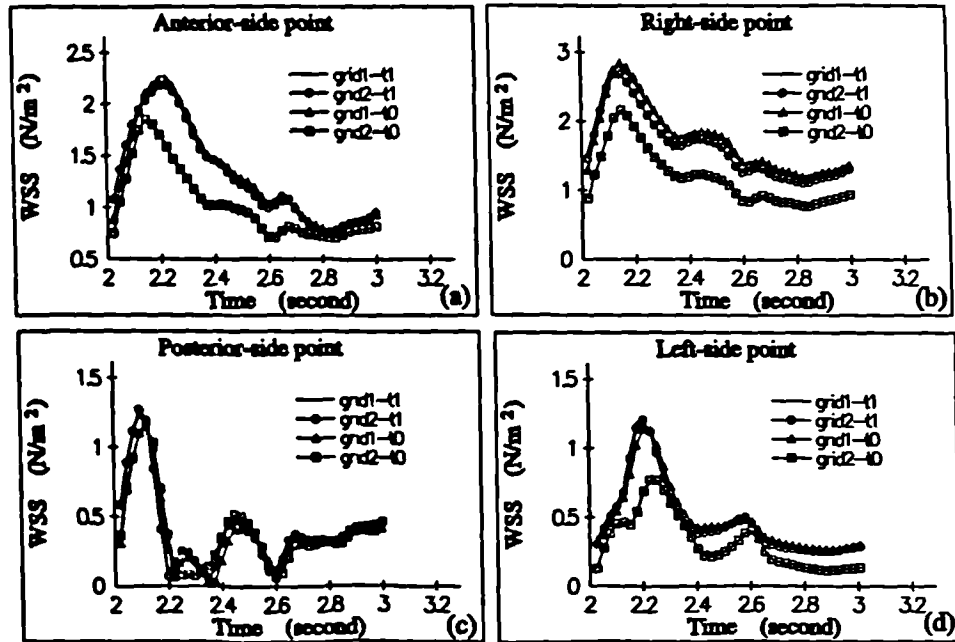
Figure 7.16: Comparison of WSS magnitude in the temporal resolution test at four wall points

chosen for one cycle (1 second) with 25ms for each time step in the first CFD calculation (t0 simulation) and 80 time-step was chosen for the second calculation with 12.5ms for each time step (t1 simulation). Therefore a total of four simulations were carried out in the combination grid1-t0, grid2-t0, grid1-t1 and grid2-t1. The comparison results at four monitor points for velocity vs time are shown in Figure 7.15 and four monitor points for WSS vs time are shown in Figure 7.16.

The results show that the simulations of grid1-t0, grid1-t1 and grid2-t1 give identical velocity and WSS values at the chosen points and significant difference can be found between the result of grid2-t0, which has larger grid and fewer time step, and the rest. Considering the grid density test results, it can be concluded that the prediction of grid1-t0 and grid1-t1 will give a more accurate prediction than grid2-t0. All CFD results presented in previous sections

are extracted from the simulation of grid1-t0.

7.4.1.2 Comparison between different boundary conditions

The choice of appropriate boundary conditions is often considered to be important in determining the flow field of interest. Unlike in case 1 (abdominal aortic bifurcation), the discussion of the influence of the boundary condition setting in this case will be concentrated on the setting of exit plane boundary conditions only. There are two ways to set the exit boundary conditions: (a) mass flow ratio between the two exit planes (two OUTLET patches) for ICA and ECA; (b) mass flow ratio among sixteen exit patches (eight patches for ICA and eight patches for the ECA exit planes) according to the measured velocity profile. For setting (a), a fully developed velocity profile assumption has to be made on the exit planes, while the second setting (or (b)) allow the velocity measurement data to be used. Furthermore, if the fully developed assumption is not correct for a short branch vessel, would it be possible to improve the result by extending the branch vessel from the velocity measurement plane to further downstream as shown in Figure 7.17. If the simulation with the outflow boundary conditions (a , (b) are called boundary-1 and boundary-2 respectively and the simulation with a longer branch vessels model is called boundary-3, the comparisons of velocity magnitude for the three simulations at two chosen points in planes 1, 2, 4 (as shown in Figure 7.5) are displayed in Figure 7.18. The WSS comparisons are shown in Figure 7.19 at four points in plane 2.

The results show that for boundary-1 and boundary-2, the velocity and WSS are identical at all times. The predictions for boundary-3 agree very well with boundary-1 in most of the points in a cycle, however, difference can be found at near posterior wall point in the CCA plane for velocity and near right wall point in the plane 1 for WSS. It can be concluded that for this case, the outflow boundary condition can be treated by using either 16 outflow patches or two outflow patches. The extended branch vessels model will only affect predictions in the high flow region.
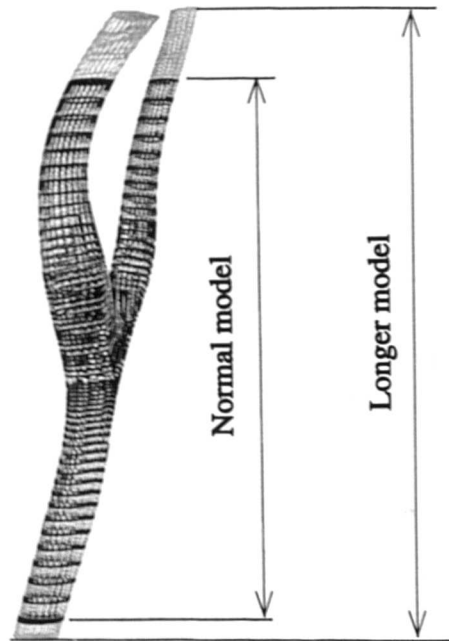
Figure 7.17: Geometrical comparison of the normal and extented model.
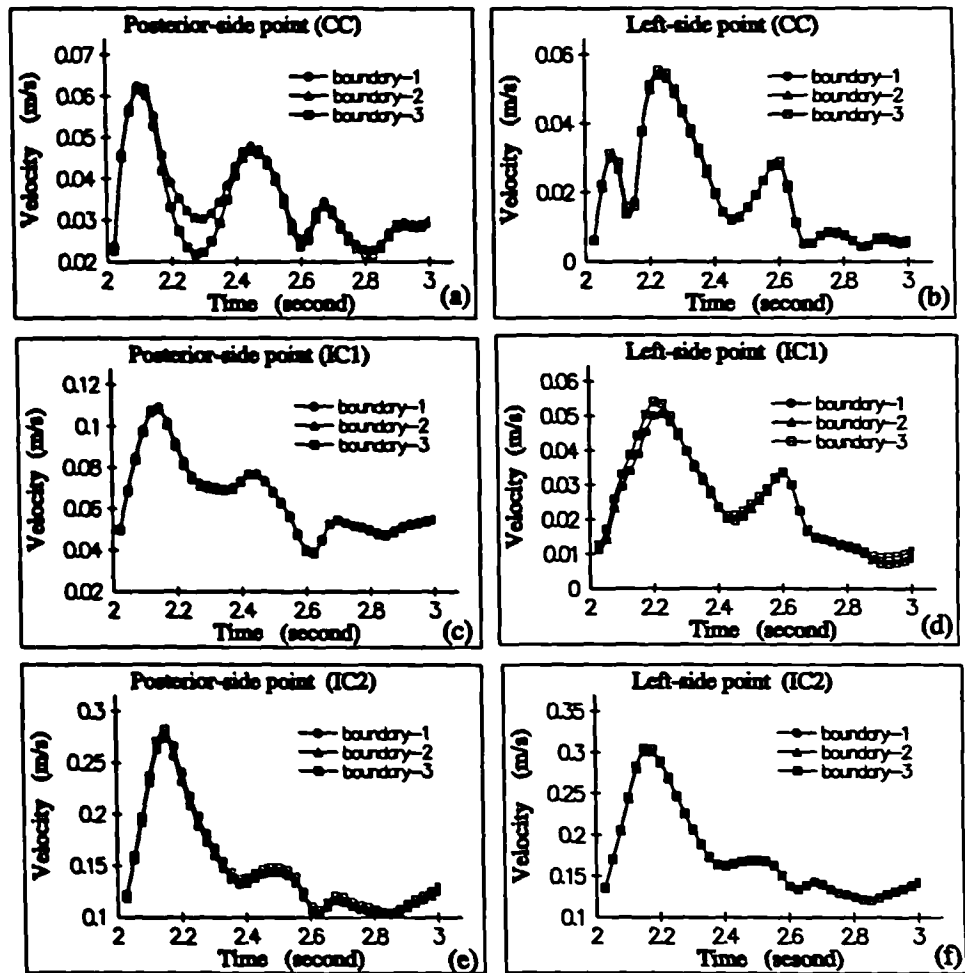
Figure 7.18: Comparison of the velocity magnitude for three different boundary settings at two chosen points in planes 1, 2, 4 as shown in Figure 7.5
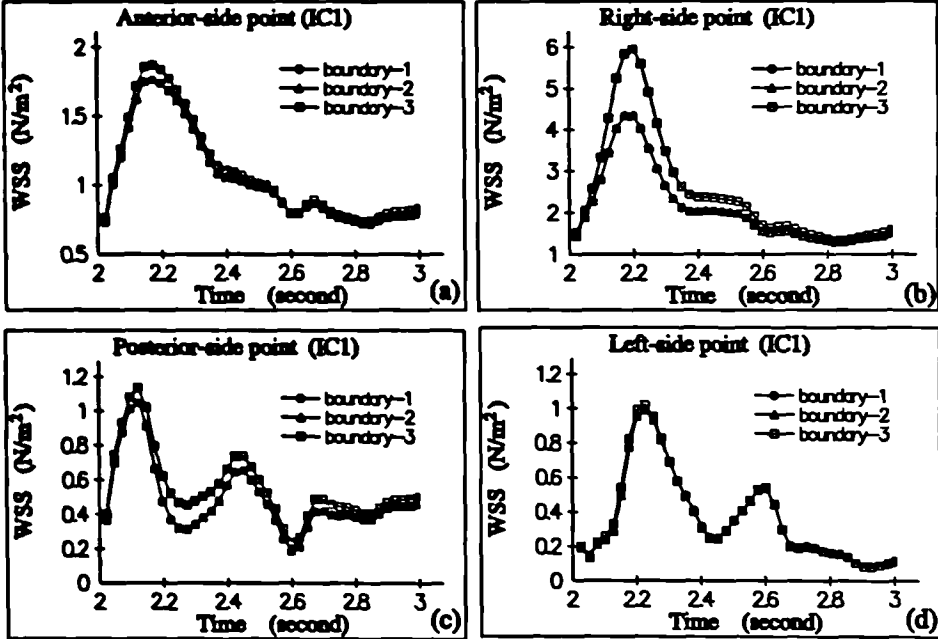
Figure 7.19: Comparison of WSS magnitude for three boundary condition settings at four points in plane 2

7.4.2 Part two: influence of smoothing parameters in geometry reconstruction on the CFD predictions

It is discussed in Chapter 3 that the choice of smoothing parameters in 3D geometrical model reconstruction will influence the final shape of the model. Although the effect is small and local, it is still likely to influence the final flow pattern predictions. The test in this section was designed to evaluate this effect.

The smooth parameters for the *normal* geometrical model (grid1) is s_{axial}=2.1 and $S_{surface}$=1.8 here called *grid A*. To test the influence of the parameters on the final CFD predictions, another geometrical model was generated by the smoothing parameters as s_{axial}=1.6 and $S_{surface}$ 1.7, called *grid B*. The differences between the two models are small on the whole but locally (ICA bulb region) they are detectable. Figure 7.20 shows the comparison of a cross-sectional area half diameter downstream from the apex in the ICA between the two models. The velocity testing points are also shown in the figure. Because of the shape difference between the two models, velocity testing points were chosen at some distance away from the wall. However, the WSS testing points were chosen at the corresponding wall points. They were logically the same points but at different physical locations.

Figure 7.21 show the velocity comparisons at five different points at the plane for the two models. As expected, the agreement at the central point and right point was perfect, the worst agreement occurred at the left side point. Because logically the central and right points were similar in both models. The distance from the left side point to the left wall of grid A was only half of the distance to the left wall of grid B.

The comparisons of WSS at four chosen points on the plane for the two models are shown in Figure 7.22. Because the points were chosen according to the logical relationship on each model, the agreement was better than the velocity comparison results.
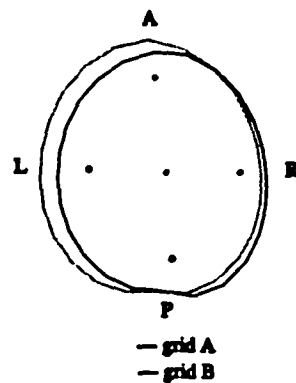
Figure 7.20: Comparison of the cross-sectional area between two geometrical models at a chosen plane in ICA, grid A is the properly smoothed model and grid B is an under smoothed model. Velocity comparison is made at the inside points.

In conclusion, the smoothing parameters do influence the geometrical model reconstruction, however, the influences were normally very small and local. These geometrical changes would not alter CFD predictions significantly.

7.4.3   Part three: comparison with MR measured velocity profiles in the common carotid artery

Validation of the overall CFD predictions is achieved by the comparison of CFD predictions with MR measured velocity at a CCA plane (plane 1 as defined in Figure 7.5). Comparison are made for velocity contours at different time steps which gives a semi-quantitative comparison, and for velocity variations at different chosen points to show the quantitative difference between the predictions and measurements.
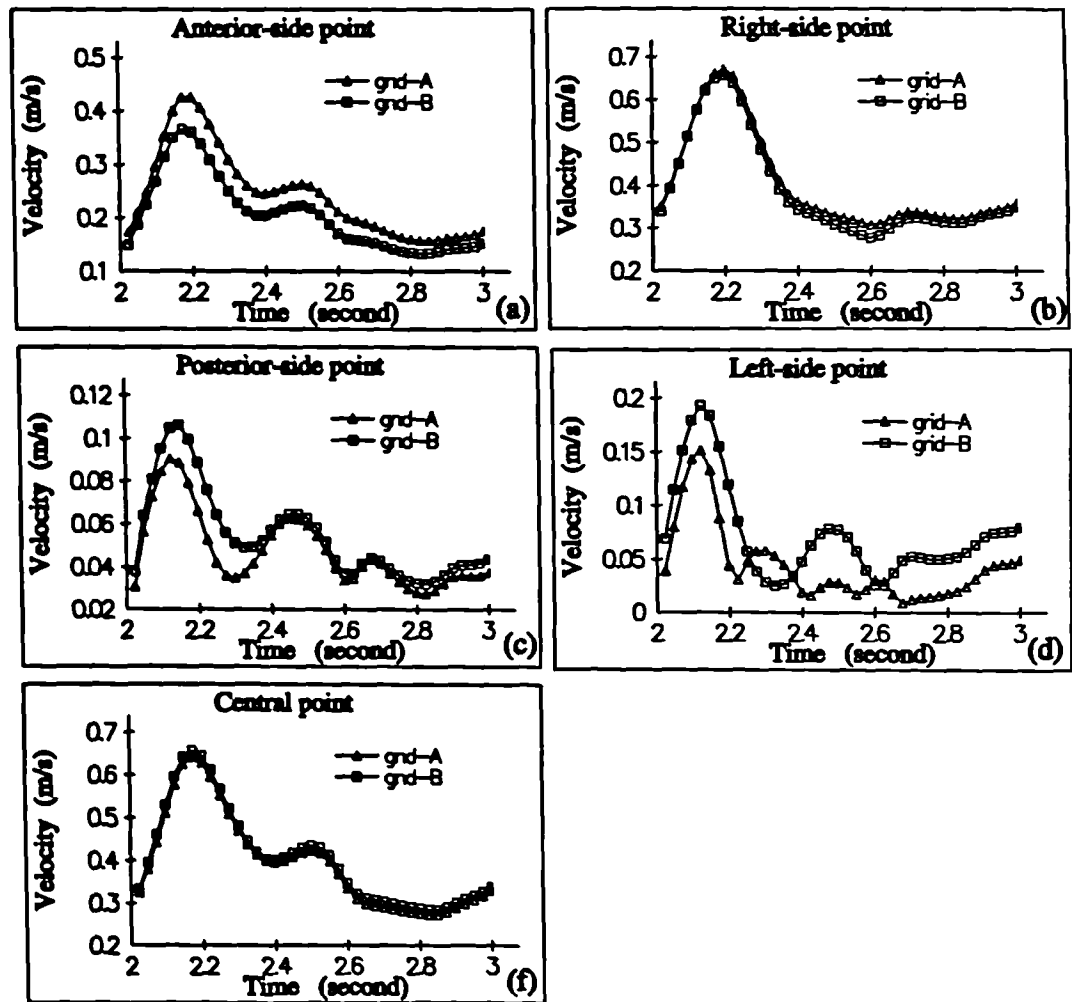
Figure 7.21: Comparison of velocity magnitude at five chosen points in the test plane for the two models.
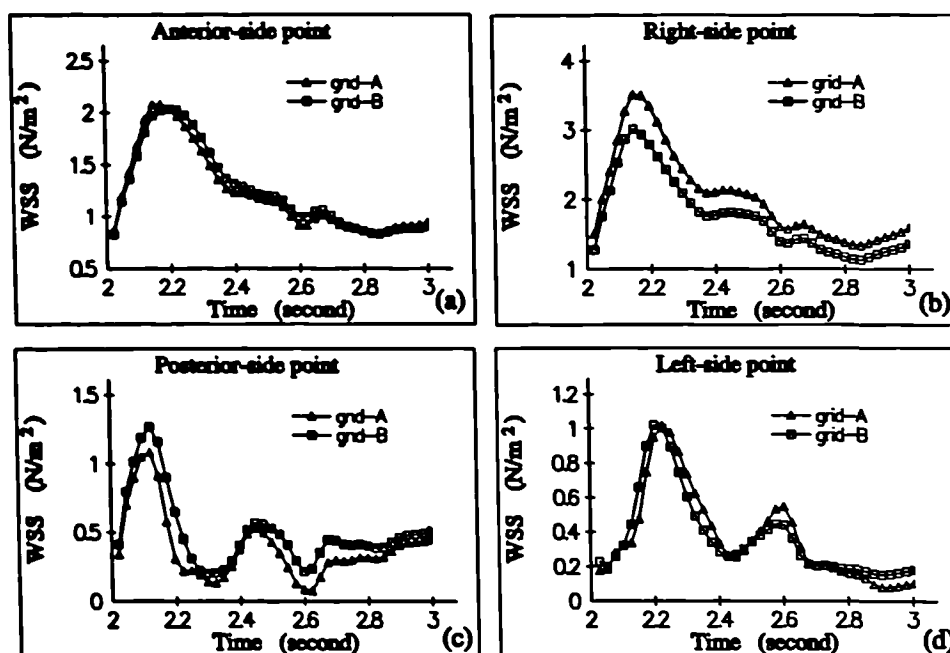
Figure 7.22: Comparison of WSS magnitude at four chosen points in the test plane for the two models.

a at time step 4   (b) at time step 7   (c) at time step 11

(d) at time step 15   (e) at time step 20   (f) at time step 30
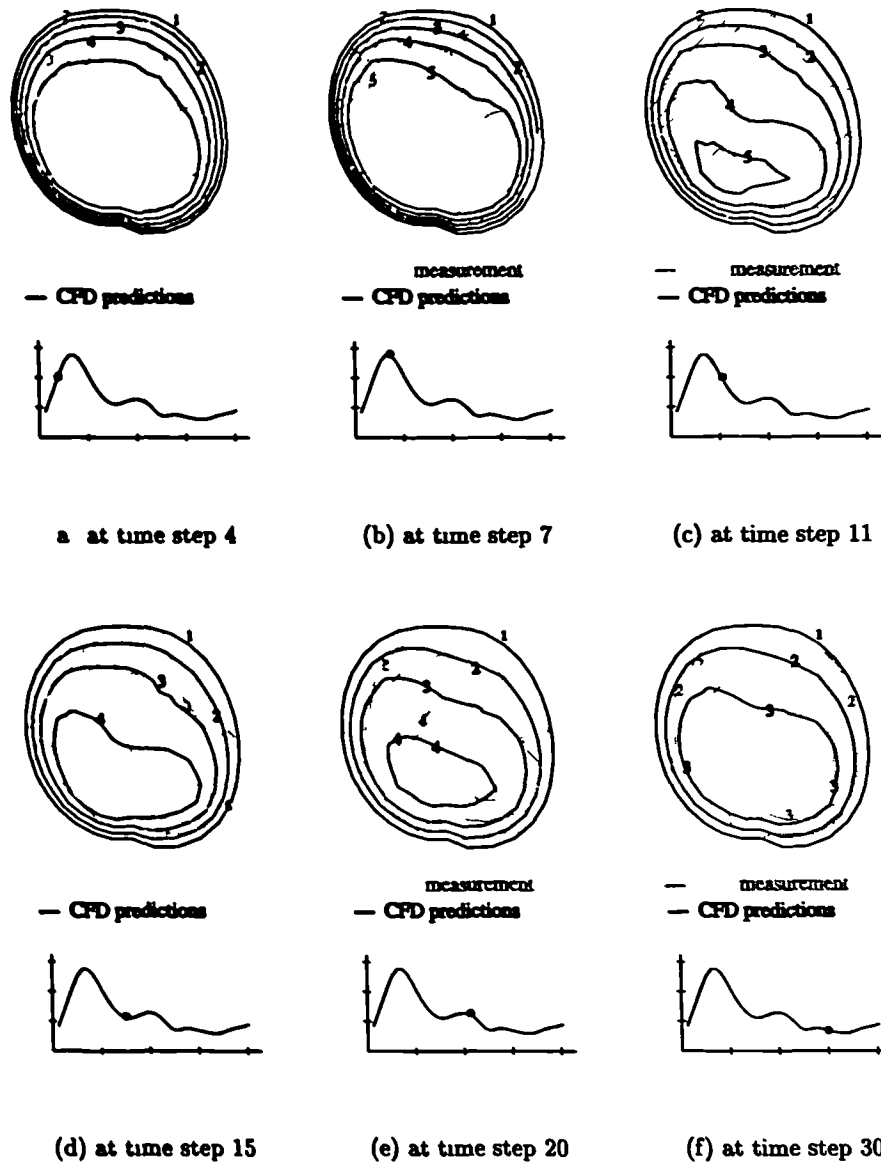
Figure 7.23: Comparisons of velocity contours of measured and predicted results at different time in a cycle.

The comparisons of the velocity contours at time steps 4, 7, 11, 15, 20 and 30 are given in Figure 7.23(a) to (f) respectively, the corresponding phases of the time steps in the cycle are shown under each contour. The orientation of the contour plot (A/P, L/R) is the same as plane 1 of Figure 7.6, the solid lines are CFD predictions and the shaded lines are the MR measurements. Compared with the predictions, the measurement lines are neither smooth nor continuous because of the low spatial resolution of measurement, and measurement errors. In most of the cases, there is no measured level-1 contour in the figure. However, the contour shape and the contour levels (values) are consistent in most of the area and time steps as shown in Figure 7.23(a), (b), (e) and (f). Differences can be found during flow deceleration phases as shown in Fig. 7.23(c) and (d). In these cases, the measured contours have a larger bending than the predictions, but are still in similar shapes to the predicted contours.

Quantitative comparisons of measured and predicted velocity magnitudes are shown in Figure 7.24. Five points in the measured plane are chosen to show the results. The location of the edge points are two grid cells (about 0.30mm) away from the wall. Measured velocities are higher than the predictions at anterior and right side and lower at posterior and left side and central points. The best agreement is seen at the central point in Fig. 7.24(e) where there is a 10% difference at the peak flow phase. The worst agreement appears at anterior-side point in Fig. 7.24(a) where the measurements are far higher than the predictions in most of the diastole. Large difference can also be observed from Figure 7.23(c), (d) and (e). However, the measured curve cannot be physically correct in Fig. 7.24(a) which may be caused by the misregistration in velocity image processing.

7.5 Conclusion

Another CFD calculation case was presented in this chapter. From the geometrical reconstruction point of view, the human carotid bifurcation is much more difficult to reconstruct than the abdominal-iliac bifurcation. This is because the large cross-sectional area variation
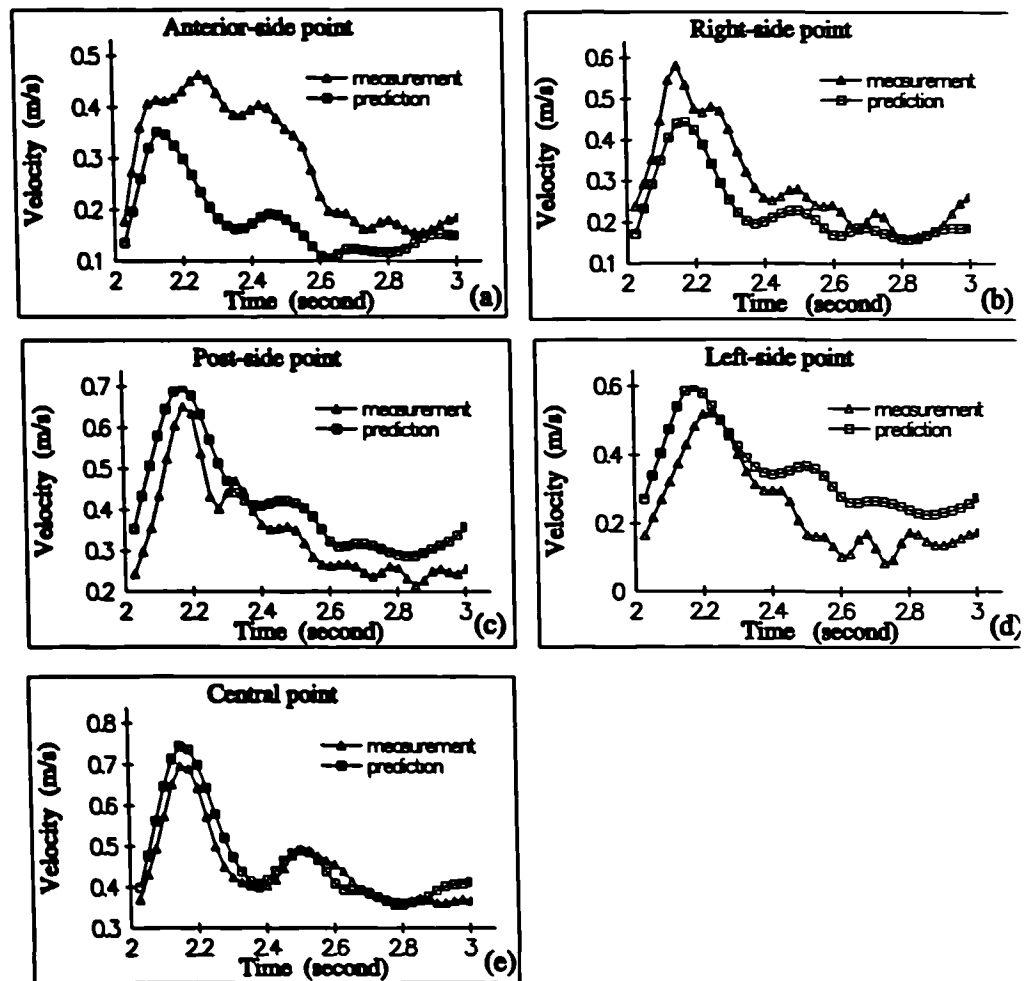
Figure 7.24: Comparisons of velocity magnitudes between the measured and predicted results at five chosen points in a cycle.

along the axial direction especially in the ICA bulb region. Associated with the geometrical complexity, flow patterns are also complicated in the ICA bulb region which normally cause MR signal loss in 2D TOF MR scans. The results show that the image processing and 3D reconstruction software is able to handle the geometry and generate reasonably smooth structured grid.

The CFD predictions for the model were shown for velocity which included velocity contours, velocity vectors, secondary velocities and reverse flow zones. Time-dependent wall shear stress contours were also presented for the model. Permanent reverse flow zones could be found in the ICA bulb region and the time-dependent volume change of the reverse flow zone was also demonstrated. Because of the out-of-plane bending in the ICA, secondary flow patterns were very complex and a spiral flow developed in the ICA in about three diameter superior to the apex. Although the WSS patterns were very complex, they did not change very much during the cardiac cycle.

The validations were carried out in three parts. They were: (a) numerical error assessment; (b) influence of geometrical model reconstruction uncertainties on CFD predictions; and (c) comparisons of CFD predictions with MR measurement.

In the first part, grid density and temporal resolution tests were carried out together with the discussion of outflow boundary condition settings. It was found that the CFD predictions would not change when outflow boundary condition settings changed from mass flow ratio between two patches to 16 patches. However, when the branch vessels were extended to gave a longer downstream distance to minimize the influence of the fully developed outflow assumption, the CFD predictions altered slightly.

The test in the second part showed that a small range variation of smoothing parameters used in the geometrical reconstruction did not have a significant effect on the CFD predictions. Again a very good agreement has been found between the CFD predictions and the

MR measured velocity profiles at a chosen plane in the common carotid.

Chapter 8

Conclusions

The present research includes studies in three main areas. They are: (a) MR scan sequences optimization and MR image acquisition (for carotid arterial angiogram scan only), (b) MR image processing and 3D geometry reconstruction, and (c) CFD simulation.

Two types of MR images are needed in the study. MR angiograms give the information required for the geometry reconstruction while MR velocity images provide velocity profiles for the purposes of boundary condition generation and validations. Because of the complex flow in the carotid sinus, signal loss is always the problem for obtaining high quality images. After a series of scans on several subjects with different scan parameters such as TE/TR, FA and FOV, an optimized scan sequence was selected for the rest of the study which is now being applied to a clinical trial.

One of the main achievements of the study is the development of the interface between MR images and a CFD solver which has been presented in chapters 3 and 4. To generate the anatomically realistic arterial bifurcation model from parallel angiograms, firstly, an automatic 2D image segmentation procedure based on a 'snake' model was developed to obtain arterial vessel contours. Secondly, 3D reconstruction and smoothing algorithms were developed to generate 3D bifurcation from the contours. Thirdly, a purpose-built grid generation software was written to create a structured grid in the bifurcation model. To guarantee the

reconstruction results are in good accuracy, uncertainty assessments were made in most of the processing steps.

MR velocity images processing software was also developed for the generation of the velocity boundary condition required by the CFD simulation. With the help of MR magnitude images, velocity images (phase image) can normally be segmented successfully. Because the velocity images were acquired at different sequences for each velocity component, registrations (a) among the velocity components and (b) from measured planes to the bifurcation model boundary planes are necessary and were proved to be time consuming and difficult tasks. Physical and logical registration procedures were employed in the research. Each of them has its own advantages and disadvantages.

With the developed tecnhiques, CFD simulations have been applied to a number of subjects. Two of them have been demonstrated in the thesis. The findings confirm that arterial bifurcations are generally non-planar with curvature. For the abdominal bifurcation case, the iliac arteries branch asymmetrically from the aorta. 3D velocity profiling suggests that secondary flows at this site are sensitive to branching asymmetry. In the carotid case, more complicated flow patterns were predicted because of the bifurcation non-planarity and the internal carotid bulb.

Flow patterns in 'real' bifurcations differ markedly from those predicted by conventional fluid dynamic models, emphasizing the need for experimental data to develop novel and modify existing models. Histologically, intimal thickening is maximal at points of flow separation, and endothelial cell mitosis rates are elevated at sites where the velocity field is fluctuating, suggesting active adaptation to local physical forces. Since atheroma localises to sites of low endothelial shear stress and/or disorganized flow such as the outer wall of bifurcations and the inner wall of curved arterial segments, combined MRI/CFD approaches may provide unique insights into these factors in individual subjects.

Much progress has been made in the past few decades in the haemodynamics research. However, the study of fluid flow in 'real' human arteries has been less successful because of the complexity of both the geometry and the flow. In this study, the problem has been overcome to some extent by the use of sophisticated MRI and numerical techniques. The interface built between MR measurement and CFD code has been applied to a number of cases and proved to be robust and reliable. The techniques presented in this study provide the tools necessary for entirely noninvasive, prospective, in vivo human studies of haemodynamics and the relationship of haemodynamics to vascular disease. The whole procedure is now being used in a clinical trial. Looking into the future, the following points should be addressed: (a) an overall validation of the 3D reconstruction procedure by comparing the reconstruction result with a known 3D object, (b) development of a more user friendly graphics interface and integration of the individual function program into a package to make the application and maintenance more efficient, (c) further CFD validation in branch vessels near the bifurcation by obtaining accurate in vivo measurements at the region.

Publication list during the project

1: Published journal paper

1. Long Q, Xu XY, Collins MW, Griffith TM and Bourne M (1998) The Combination of Magnetic Resonance Angiography and Computational Fluid Dynamics: a critical review. *Critical reviews in biomedical engineering*, 26(4):227-276

2. Long Q, Xu XY, Collins MW, Bourne M and Griffith TM (1998) Magnetic Resonance Image Processing and Structured Grid Generation of a Human Abdominal Bifurcation. *Computer Methods and Programs in Biomedicine*, 56:249-259

3. Long Q, Xu XY, Collins MW, Griffith TM and Bourne M (1997) Some fluid dynamics aspects of the aortic bifurcation using magnetic resonance imaging and computational fluid dynamics. *Internal Medicine*, 5(1):33-39

4. Xu XY, Long Q, Collins MW, Griffith TM and Bourne M (1999) 3D Reconstruction of the flow in human arteries. *Proc. of IMechE, J. of Eng. in Med. (in press)*.

5. Long Q, Xu XY, Collins MW, Griffith TM and Bourne M (1999) Simulation of flow in human arterial bifurcations using a combination of CFD and MRI techniques. *Haemodynamics of Arterial Organs - Comparison of Computational Predictions with in Vivo and in Vitro Data*, Eds: Collins MW and Xu XY, WIT Press (in press).

2: Published in referenced conferences:

1. Long Q, Xu XY and Collins MW (1998) 3D Visualization of blood flows in arterial organs: A novel development of computational methods using MR or Ultrasound data *Proc. 8th International Symposium on Flow Visualization, Sorrento Italy*.

2. Long Q, Xu XY, Collins MW, Stanton A, Thom SA and Hughes AD (1998) Reproducibility analysis of 3D geometrical reconstruction of a human arterial bifurcation *Proc. Medical Image Understanding and Analysis '98*, Leeds University, pp 21-24

3. Long Q, Xu XY, Collins MW, Griffith TM and Bourne M (1997) Generation of CFD Velocity Boundary Condition from Cine MR Phase-Contrast Images. *Proc. Medical Image Understanding and Analysis '97, Univ. of Oxford*, pp 117-120.

4. Collins MW and Long Q (1997) Three-dimensional numerical simulation of oscillatory flow in blood vessel branches. *Proc. Workshop'97, Biomechanical Modeling & Numerical Simulation, Prague, Sept. 25-26*, pp 7-19

5. Q. Long, X.Y. Xu, M.W. Collins (1996) Generation of Structure of the Aortic Bifurcation From Magnetic Resonance Angiogram. *Simulation Modelling in Bioengineering, Eds: M Cerrolaza et al, Comput. Mech. Pub.*, pp217-226

Bibliography

[1] Davies MJ and Woolf N (1990) Atheroma: Atherosclerosis in ischaemic heart disease, the mechanisms. *Bayer UK Limited. Science press*

[2] Fry DL (1968) Acute vascular endothelial changes associated with increased blood velocity gradients. *Circ. Res.* 22:165-197

[3] Asakura T and Karino T(1990) Flow patterns and spatial distribution of atherosclerotic lesions in human coronary arteries. *Circ. Res*, 66:1045-1066

[4] Caro CG, Fitz-gerald JM and Schroter RC (1971) Atheroma and arterial wall shear. Observation, correlation and proposal of a shear dependent mass transfer mechanism for atherogenesis. *Proc. Roy. Soc. Lond. B*, 177:109-159

[5] Friedman M.H. et al.(1981) Correlation between intimal thickness and fluid shear in human arteries. *Atherosclerosis* 39: 425-436

[6] Friedman M.H. et al.(1986) Shear dependent thickening of the human arterial intima. *Atherosclerosis* 60: 161-171

[7] Duncan LE and Buck K (1959) Passage of labelled cholesterol into the aortic wall of the normal dog. *Circ. Res.*, 7:765-770

[8] Davies PF, et al.(1972) Turbulent fluid shear stress induces vascular endothelial cell turnover in vitro. *Proc. Natl. Acad. Sci. USA* 83: 2114-2117

[9] Flaherty JT, Pierce JE, Ferrans VJ et al (1972) Endothelial nuclear patterns in the canine arterial tree with particular reference to hemodynamic events. *Circ REs.*, 30: 23-33.

[10] Fry DL (1969) Certain chemorheologic considerations regarding the blood vascular interface with particular reference to coronary artery disease. *Circulation* 40: IV-38-39

[11] Kim D.W. et al.(1989) Patterns of endothelial microfilament distribution in the rabbit aorta in situ. *Circ Res.* 64: 21-31, 1989

[12] Davies P.F. et al.(1984) Influence if haemodynamic forces on vascular endothelial function *J. Clin. Invest.* 73: 1121-1129

[13] Sprague E.A. et al.(1987) Influence of a laminar steady state fluid imposed wall shear stress on the binding, internalisation and degradation of low-density lipoproteins by cultured arterial endothelium. *Circulation* 76: 648-656

[14] Caro CG and Lever MJ (1983) Effect of vasoactive agents and applied stress on the albumin space of excised rabbit carotid arteries. *Atherosclerosis.* 46: 137-146

[15] Seed WA and Wood NB (1970) Development and evaluation of a hot-film velocity probe for cardiovascular studies. *Cardiovasc. Res.*, 4: 253-63

[16] Seed WA and Wood NB (1971) Velocity patterns in the aorta. *Cardiovasc. Res.*, 5: 319-30

[17] Yamaguchi T, Kikkawa S and Parker KH (1984) Application of Taylor's hypothesis to an unsteady convective field for the spectral analysis of turbulence in the aorta. *J. of Biomechanics* 17(12): 889-95

[18] Xu XY and Collins MW (1994) Studies of blood flow in arterial bifurcation using computational fluid dynamics. *Proc Instn Mech Engrs, Part H: J. Eng in Medicine*, 208:163-175.

[19] Berger SA, Talbot L, and Yao LS (1983) Flow in curved pipes. A. Rev. *Fluid Mech.* 15:461-512

[20] Furst G., Steinmetz H., Fischer H., et al (1993) Selective MR Angiography and intracranial collateral blood flow, *J of computer assisted tomography*, 17(2): pp178-183

[21] Edelman RR, Mattle HP, Kleefield J and Silver MS (1989) Quantification of blood-flow with dynamic MR imaging and presaturation bolus tracking, *Radiology* 171(2):551-556

[22] Edelman RR. (1992) Basic principles of magnetic resonance angiography, *Cardiovasc. Intervent. Radiol.*, 15: pp3-13

[23] Quinn SF., Demlow TA., Hallin RW. et al (1993) Femoral MR-angiography versus conventional angiography - preliminary results, *Radiology*, 189: pp181-184

[24] Finn JP., and Longmaid HE. (1992) Abdominal magnetic resonance venography, *Cardiovasc Intervent Radiol*, 15: pp51-59

[25] Cellerini M, Konze A, Sottili P, Pellicano G, DalPozzo G (1997) MRA techniques: state of the art *Rivista Di Neuroradiologia* 10:82-84

[26] Blatter DD, Parker DL and Robison RO (1991) Cerebral MR angiography with multiple overlapping thin slab acquisition, *Radiology*, 179: pp805-811

[27] Kauczor HU, Engenhart R, Layer G, et al (1993) 3D TOF MR angiography of cerebral arteriovenous malformations after radiosurgery *J. of computer assisted tomography*, 17(2): pp184-190

[28] Dumoulin CL. and Hart HR. (1986) Magnetic resonance angiography, *Radiology*, 161: pp717-720

[29] O'Donnell M (1985), Blood flow imaging using meltiecho phase contrast sequences. *Med Phys*, 12:59-64

[30] Edelman RR, Mattle HP, Atkinson DJ, Hoogewoud HM (1990) MR angiography *AJR* 154:937-946

[31] Anderson CM, Salonar D, Tsuruda JS, Shapeero LG and Lee RE (1990)Artifacts in maximum-intensity-projection display of MR angiograms. *AJR* 154:623-629

[32] Hennig J, Scheffler K, Laubenberger J and Strecker R (1997) Time-resolved projection angiography after bolus injection of contrast agent *Magnetic resonance in medicine*, 37:341-345

[33] Korosec FR, Frayne R, Grist TM and Mistretta CA (1996) Time-resolved contrast-enhanced 3D MR angiography *Magnetic resonance in medicine*, 36:345-351

[34] Conturo TE, Barker PB, Mathews VP, Monsein LH and Bryan RN (1992) MR imaging of cerebral perfusion by phase-angle reconstruction of bolus paramagnetic-induced frequency shifts *Magn. Reson. Med.* 27:375-390

[35] Akbudak E, Norberg RE and Conturo TE (1997) Contrast-agent phase effects: an experimental system for analysis of susceptibility, concentration, and bolus input function kinetics *Magnetic resonance in medicine*, 38:990-1002

[36] Bogdanov AA, Weissleder R and Frank HW et al (1993) A new macromolecule as a contrast agent for MR angiography: preparation, properties and animal studies. *Radiology* 187.701-706

[37] Marchal G, Bosmans H and Van Hecke P et al (1991) Experimental Gd-DTPA-polylysine enhanced MR angiography: sequence optimization. *J Comput Assist Tomogr.* 15:711-715

[38] Schuhmann GG, Schmitt WH, Frenzel T, Press WR and Weinmann H (1991) In vivo and in vitro evaluation of Gd-DTPA-polylysine as a macromolecular contrast agent for magnetic resonance imaging. *Invest Radiol.* 26:969-974

[39] Vogl TJ, Juergens M and Balzer JO (1995) Magnetic resonance angiography: plain and contrast enhanced techniques. *Advances in MRI contrast* 3:84-96.

[40] Nayler GL, Firmin DN and Longmore DB (1986), Blood flow imaging by cine magnetic resonance. *Journal of Computer Assist Tomogr,* 10:715-722

[41] Pelc NJ, Herfkens RJ Shimakawa A and Enzman DR (1991) Phase contrast cine magnetic resonance imaging. *Magn. Reson. Quarterly.* 7:229-254

[42] Spraggins TA (1990) Wireless retrospective gating - application to cine cardiac imaging *Magnetic resonance imaging* 8(6) pp 675-681.

[43] Frayne R and Rutt BK (1993) Frequency response of retrospectively gated phase-contrast MR imaging: effect of interpolation. *J. Magn. Reson. Imaging.* 3:907-917

[44] Wigstrom L, Sjoqvist L and Wranne B (1996) Temporally resolved 3D phase-contrast imaging. *Magn. Reson. Med* 36:800-803

[45] Axel L and Morton D (1989), Correction of phase wrapping in magnetic resonance imaging. *Med Phys*, 16:284-287

[46] Kadowaki C, Hara M, Numoto M, Takeuchi K and Saito I (1995) Cine Magnetic-Resonance-Imaging of aqueductal stenosis *Childs nervous system* 11(2):107-111.

[47] Mohiaddin RH, Gatehouse PD, Henien M and Firmin DN (1997) Cine MR Fourier velocimeter of blood flow through cardiac valves: Comparison with Doppler echocardiography *JMRI - J. of Magnetic Resonance Imaging* 7(4): 657-663.

[48] vanderGeest RJ, deRoos A, vanderWall EE and Reiber JHC Quantitative analysis of cardiovascular MR images *International J of Cardiac Imaging* 13(3): 247-258.

[49] Matsumura K, Nakase E, Haiyama T and Utsunomiya S (1995) Automatic left-ventricular volume measurements on contrast-enhanced ultrafast cine magnetic-resonance-imaging *European J of Radiology* 20(2): 126-132.

[50] Kvam G, Dahle H, Nordrehaug JE, Randa TI and Tillung T (1997) The shortening fraction of myocardial fibres and its layered distribution, as derived from cine-MR imaged left ventriculograms - An approach for evaluating global left ventricular function *ACTA Radiological* 38(3):391-399.

[51] Hartnell GG, Cohen MC, Meier RA and Finn JP (1996) Magnetic-resonance angiography demonstration of congenital heart-disease in adults *Clinical Radiology* 5112 851-857.

[52] Burkart DJ., Felmlee JP., Johnson CD. et al (1994) Cine phase-contrast MR flow measurements: improved precision using an automated method of vessel detection, *J. of computer assisted tomography*, 18(3): 469-475

[53] Feinberg DA., Crooks LE., Sheldon P. et al (1985) Magnetic-resonance imaging the velocity vector components of fluid flow, *Mag. Reson. Med.*, 2: pp.555-566

[54] Hennig J., Muri M., Brunner P. et al (1988) Quantitative flow measurement with the fast Fourier flow technique, *Radiology*, 166(1): pp.237-240

[55] Dumoulin CL., Souza SP., Hardy CJ. et al (1991) Quantitative measurement of blood-flow using cylindrically localized Fourier velocity encoding, *Mag. Reson. Med.*, 21: pp.242-250

[56] Dumoulin CL., Doorly DJ. and Caro CG. (1993) Quantitative measurement of velocity at multiple positions using comb excitation and Fourier velocity encoding, *Mag. Reson. Med.*, pp44-52

[57] Caro CG, Doorly DJ, Tarnawski M, et al (1996) Nonplanar curvature and branching of arteries and non-planar-type flow, *Proceedings of the Royal Society of London A*, 452(1944): pp.185-197

[58] Caro CG, Cybulski G and Darrow RD et al (1993) Femoral-artery distensibility in human athletes and nonathletes - Local arterial wavespeed determined by Comb-excitation Fourier Velocity-encoded Magnetic-Resonance-Imaging (MRI), *Journal of Physiology-London*, *Vol 467, p.P 68*

[59] Dumoulin CL., Darrow RD., Eisner DR. et al (1994) Simultaneous detection of multiple components of motion with MRI, *J. of computer assisted tomography*, 18(4):652-660

[60] Mohiaddin RH, Gatehouse PD and Firmin DN (1995) Exercise related changes in aortic flow measured with spiral echo-planar MR velocity mapping. *JMRI-J of Magnetic Reson. Imaging.* 5:159-163

[61] Nishimura DG, Irarrazabal P and Meyer CH (1995) A velocity K-space analysis of flow effects in echo-planar and spiral imaging. *Magn. Reson. in Med.* 33:549-556

[62] Debatin JF, Leung DA, Wildermuth S, et al (1995) Flow quantitation with echo-planar phase-contrast velocity mapping - in-vitro anti in-vivo evaluation. *JMRI - J. of Magn. Reson. Imaging.* 5:656-662

[63] Eichenberger AC, Schwitter J, Mckinnon GC, Debatin JF and Vonschulthess GK (1995) Phase-contrast echo-planar MR-imaging - Real-time quantification of flow and velocity patterns in the thoracic vessels induced by valsalvas maneuver. *JMRI - J. Magn. Reson. Imaging.* 5:648-655

[64] Gatenby JC and Gore JC (1996) Echo-planar-imaging studies of turbulent-flow. *J of Magn. Reson. series A.* 121:193-200

65] Laub GA. and Kaiser WA (1988) MR angiography with gradient motion rephasing. *J. of computer assisted tomography,* 12: pp377-382

[66] Saloner D. Hanson W., Tsuruda JS. et al (1990) Connected voxel algorithm for magnetic resonance angiography. *Proc. of 9th annual meeting of the Soc. for MAg. Res. Med. New York,* p488

[67] Murakami T., Kashiwagi T., Nakamura H (1993) Display of MR angiograms: maximum intensity projection versus three-dimensional rendering. *Euro. J. of Radiol.* 17: pp95-100

[68] Saloner D and Anderson CM. (1992) Instrumentation for magnetic resonance angiography. *Cardiovasc. Intervent. Radiol.,* 15: pp14-22

[69] Zonneveld FW. (1993) A decade of clinical three-dimensional imaging: a review. *Investigative Radiology,* 29: pp716-725

[70] Mohiaddin RH. Yang GZ., Burger P. et al (1992) Automatic enhancement, animation, and segmentation flow in peripheral arteries from MR phase-shift velocity mapping. *J. of computer tomography* 16(2): pp176-181

[71] Mohiaddin RH. Yang GZ. and Kilner PJ. (1994) Visualization of flow by vector analysis of multidirectional cine MR velocity mapping. *J. of computer assisted tomography*, 18: pp383-392

[72] Cline HE., Lorensen WE. and Schroeder WJ. (1993) 3D phase contrast MRI of cerebral blood flow and surface anatomy. *J. of computer assisted tomography*, 17(2): pp173-177

[73] Lee JN. (1993) Arterial edge artifacts in gated, phase re-ordered phase contrast angiography of the extremities, *Mag. Res. Imaging*, 11: pp335-339

[74] Rogers Jr WJ. and Shapiro EP. (1993) Effect of RR interval variation on image quality in gated, two-dimensional, Fourier MR imaging, *Radiology*, 186: pp883-887

[75] Isoda H., Masui T., Hasegawa S. et al (1994) Pulmonary MR angiography: a comparison of 2D and 3D time-of-flight, *J. of computer assisted tomography*, 18(3): pp402-407

[76] Doyle M., Mulligan SA., Matsuda T. and Pohost GM. (1992) Outflow refreshment angiography: a bright blood, bright static tissue technique, *Magnetic resonance imaging*, 10: pp887-892

[77] Kilner PJ., Firmin DN., Rees RSO et al (1991) Valve and great vessel stenoses: assessment with MR jet velocity mapping, *Radiology*, 178: pp229-235

[78] Furst G., Hofer M., Sitzer M. et al (1995) Factors influencing flow-induced signal loss in MR angiography: an in vitro study, *J. of computer assisted tomography*, 19(5): pp692-699

[79] Dumoulin CL. Souza SP., Walker MF., and Wagle W. (1989) Three-dimensional phase contrast MR angiography, *Mag. Reson. Med.* 9: p139-149

[80] Stauber JR (1986) Programmable gradient pre-emphasis for eddy current correction, *Proc. of 5th annual meeting of the Soc. for Mag. Res. Med.*, Montreal p1430

[81] Chien D., Saloner D., Laub G. and Anderson CM. (1994) High resolution cine MRI of vessel distension, *J. of computer assisted tomography*, 18(4): pp576-580

[82] Tarnawski M, Porter DA, Graves MJ, Taylor MG and Smith MA (1989) Flow determi-
nation in small diameter vessels by magnetic resonance imaging. *Proc Soc Magn Reson
Med,* 1989:896

[83] Parker DL. GUllberg GT. and Frederick PR. (1987) Gibbs artifact removal in magnetic
resonance imaging, *Med. Phys.* 14(4): 640-645

[84] Peli T and Lim JS. (1982) Adaptive filtering for image enhancement, *Optical Eng.*, 21(1):
pp.108-112

[85] Sezan MI. Takalp AM. and Schaetzing R. (1989) Automatic anatomical selective image
enhancement in digital chest radiography, *IEEE Trans. on Med. Imag.* 8: pp.154-162

[86] Ji TL., Sundareshan MK. and Roehrig H. (1994) Adaptive image contrast enhancement
based on human visual properties, *IEEE Trans. on Med. Img.* 13(4): pp.573-586

[87] Ketcham DJ. Lower RW. and Weber JW. (1976) Real-time image enhancement tech-
niques, *in seminar on image processing* pp.1-6

[88] Pizer SM. Zimmerman JB. and Staab EV. (1984) Adaptive grey level assignment in CT
scan display, *J. of computer assisted tomography,* 8(2): pp.300-305

[89] Pizer SM. Amburn EP. Austin JD. et al (1987) Adaptive histogram equalization and its
variations, *comput. Vision. Graphics and image processing,* 39: pp.355-368

[90] Lee JS (1980) Digital image enhancement and noise filtering by use of local statistics,
IEEE Trans. Patt. Anal Machine Intell. PAMI-2(2): pp.165-168

[91] Wang DCC. Vagucci AH. and Li CC. (1981) Gradient inverse weighted (GIW) scheme
and the evaluation of its performance, *Comput. Graph. Image Processing* 15: pp.167-181

[92] Wang X. (1992) On the gradient inverse weighted filter, *IEEE Trans. Signal processing*
40(2) pp.482-484

[93] Clarke LP. Velthuizen RP. Camacho MA. et al (1995) MRI segmentation: methods and
applications. *Mag. Reson. Imaging,* 13(3): pp.343-368

[94] Sahoo PK, Soltani S, Wong AKC, et al (1988) Survey of thresholding techniques. *computer vision, graphics, and image processing*, 41(2): pp.233-260

[95] Sonka M, Hlavac V, and Boyle R, (1993) Image processing, analysis and machine vision. *Chapman and Hall Computing, (London, Glasgow, Weinheim, New York, Tokyo, Melbourne, Madras)*

[96] Garcia JA. Fdez-Valdivia J and Garrido A. (1995) A scale- vector approach for edge detection. *Pattern recognition letters* 16:pp.637-646

[97] Yang J and Li XB. (1995) Boundary detection using mathematical morphology. *Pattern recognition letters*, 16: pp1277-1286

[98] Basu A. Jain MK. and Li XB. (1995) Improving boundary detection using variable resolution masks. *Pattern recognition letters*, 16: pp.1205-1211

[99] Kass M. Witkin A. and Terzopoulos D. (1987) Snakes: active contour models, *Proceeding of first international conference on computer vision, 8-11 June 1987, London. (IEEE computer Soc. Press* PP.259-268

[100] Yezzi A, Kichenassamy S, Kumar A, Olver P and Tannenbaum A (1997) A geometric snake model for segmentation of medical imagery *IEEE Transactions on Medical Imaging* 16(2):199-209

[101] Gunn SR and Nixon MS (1997) Robust snake implementation; A dual active contour *IEEE Transactions on Pattern Analysis and Machine Intelligence* 19(1): 63-68.

[102] Caselles V and Coll B (1996) Snakes in movement *SIAM J on Numerical analysis* 336: 2445-2456.

[103] Williams DJ. and Shah M (1992) A fast algorithm for active contours and curvature estimation. *CVGIP: image understanding* 55: pp14-26

[104] Amini A, Tehrani S, and Weymouth T, (1988) Using dynamic programming for minimizing the energy of active contours in the presence of hard constraints. *Proc., 2'nd*

international conference on computer vision, tampa, FL pp.95-99, IEEE piscataway, NJ, 1988

[105] Chen CH. and Lee AS. (1995) 3D image reconstruction of bladder by nonlinear interpolation. *Mathl. Comput. Modelling* 22(8): pp.61-72

[106] Ranganath S. (1995) Contour extraction from cardiac MRI studies using Snakes. *IEEE Trans. on medical imaging* 14(2): pp.328-338

[107] Berger MO, and Mohr R, (1990) Towards autonomy in active contour models. *Proc. 10th international conference onpattern recognition, Atlantic City, NJ,* pp.847-851

[108] Cohen LD. (1991) On active contour models and balloons, *Comput. Vision. Graphics, and image processing: image understanding* 53(2): pp211-218

[109] Cohen LD. and Cohen I. (1993) Finite-element methods for active contour models and balloons for 2D and 3D images, *IEEE Trans. on pattern analysis and Machine Intelligence,* 15(11): pp.1131-1147

[110] Miller JV., Breen DE. Lorensen WE. (1995) Geometrically deformed models: a method to extract closed geometric model from volume data. *Comput. Graphics,* 25(4): pp.217-226

[111] Lobregt S and Viergever MA. (1995) A discrete dynamic contour model. *IEEE Trans. on Medical Imaging* 14(1): pp.12-24

[112] Rueckert D and Burger P. (1995) Contour fitting using an adaptive spline model. *British Machine Vision Conference,* 1995

[113] Chang YL. and Li X. (1995) Fast image region growing. *Imag. and Vision Computing* 13(7): pp.559-571

[114] Chang YL. and Li X. (1994) Adaptive image region-growing. *IEEE Trans. on Imag. Proce.* 3(6): pp.868-872

[115] Willebeek-LeMair M and Reeves AP. (1990) Solving nonuniform problems on SIMD computers: case study on region growing. *J. of Parallel and Dist. Computing* 8: pp.135-149

[116] Cline HE, Lorensen WE, Ludke S et al (1988) 2 algorithms for the 3-dimensional reconstruction of tomograms. *Medical Physics*, 15(3): pp.320-327

[117] Cline HE, Dumoulin CL, Lorensen WE, et al (1991) Volume rendering and connectivity algorithms for MR angiography. *Mag. Reson. Med.* 18(2): pp.382-394

[118] Cline HE, Lorensen WE, Souza SP, et al (1991) 3D surface rendered MR images of the brain and its vasculature. *J. of computer assisted tomography*, 15(2): pp.344-351

[119] Lorensen WE and Cline HE (1987) Maching cubes: A high resolution 3D surface construction algorithm. *Comput Graphics*, 21: pp.163-169

[120] Kandarpa K, Sandor T, Tieman J et al (1993) Rapid 3-dimensional surface reconstruction of magnetic-resonance images of large arteries and veins - a preliminary evaluation of clinical utility. *Cardiovascular and interventional radiology*, 16(1): 25-29

[121] Porrill J. and Ivins J. (1994) A semiautomatic tool for 3D medical image analysis using active contour models. *Med. Inform.* 19(1): pp.81-90

[122] Farin G (1988) Curves and surfaces for computer aided geometric design: practical guide *(London Academic Press)*

[123] Dubois SR. and Glang SJ. (1986) An autoregressive model approach to two-dimensional shape classification, *IEEE Trans. on PAMI* PAMI-8(1): pp.55-66

[124] Cook LT. Dwyer SJ. Batnitsky S. et al (1983) A three-dimensional display system for diagnostic imaging applications, *Comput. Graphics Appl.* 3(5): pp.13-19

[125] Long Q, Xu XY, Collins MW, Bourne M and Griffith TM (1998) Magnetic Resonance Image Processing and Structured Grid Generation of a Human Abdominal Bifurcation *Computer Methods and Programs in Biomedicine.* 56:249-259

[126] Monga O, Deriche R and Rocchisani JM, (1991) 3D edge-detection using recursive filtering - application to scanner images, *CVGIP-Image Understanding*, 53(1):76-87

[127] Monga O, Ayache N and Sander P (1991), Using uncertainty to link 3D-edge detection and local surface modelling, *Lecture notes in computer science*, 511:273-284

[128] Monga O, Ayache N and Sander PT (1992), From voxel to intrinsic surface-features, *Image and vision computing* 10(6):403-417

[129] Monga O and Benayoun S (1995), Using partial derivatives of 3D images to extract typical surface-features, *Computer vision and image understanding* 61(2):171-189

[130] McInerney T and Terzopoulos D (1995) A dynamic finite-element surface model for segmentation and tracking in multidimensional medical images with application to cardiac 4D image-analysis *Computerized medical imaging and graphics* 19(1):69-83.

[131] Goshtasby A and Turner DA. (1995) Segmentation of cardiac cine MR images for extraction of right and left ventricular chambers, *IEEE Trans. on Med. Img.* 14(1): pp.56-63

[132] Hohne KH and Hanson WA (1992), Interactive 3D segmentation of MRI and CT volumes using morphological operations, *Journal of Computer Assisted Tomography*, 16(2):285-294

[133] Alvarez L, Lions PL and Morel JM (1992), Image selective smoothing and edge-detection by nonlinear diffusion .2., *SIAM Journal on Numerical Analysis*, 29(3):845-866

[134] Kacur J and Mikula K (1995) Solution of nonlinear diffusion appearing in image smoothing and edge-detection, *Applied Numerical Mathematics*, 17(1):47-59

[135] Schmidt J, Gatlin B, Eason J, et al (1992) Skeletal muscle grids for assessing current distributions from defibrillation shocks *Critical Reviews in Biomed. Eng.* 20(1,2):121-139

[136] Thompson JF, Warsi ZUA and Mastin CW, (1982) Boundary-fitted coordinate systems for numerical solution of partial differential equations — A review, *J. of Computat. Phys.* 47(1):

[137] Thompson JF, Warsi ZUA and Mastin CW, (1985) Numerical grid generation: Foundations and applications, *North-Holland, Amsterdam*

[138] Thompson JF (1986) A survey of composite grid generation for general three-dimensional regions, *Numerical Methods for Engine-Airframe Interpolation, Murthy, S.N.B. and Paynter GC Eds., AIAA., New York*

[139] Thompson JF (1988a) Grid generation, *Handbook of Numerical Heat Transfer,* Minkowycz WJ, Sparrow EM, Schneider GE, et al Eds., Wiley, New york, Ch.21

[140] Thompson JF, and Steger JL, Eds (1988b) Three dimensional grid generation for complex configurations Recent progress, *AGARD-AG NO. 309, AGARD, NATO,* 1988

[141] Yu TY, and Soni BK, (1995) Application of NURBS in numerical grid generation, *Computer-aided design,* 27(2):147-157

[142] Khamayseh A, and Mastin CW, (1994) Surface grid generation based on elliptic PDE models, *Applied Mathe. and Computation,* 65(1-3):253-264

[143] Chan WM, and Buning PG, (1995) Surface grid generation methods for overset grids, *Computers and Fluids,* 24(5):509-522

[144] Knupp PM (1993) Surface grid generation in the tangent plane, *Applied mathematics and computation* 59(1):41-62

[145] Thompson JF, and Weatherill NP, (1992) Structured and unstructured grid generation, *Critical Reviews in Biomedical Eng.* 20(1,2):73-120

[146] Lo SH, (1985) A new mesh generation scheme for arbitrary planer domains, *Int. J. Numer Methods Eng.,* 21:1403-1426, 1985

[147] Lohner R and Parikh P (1988) Three-dimensional grid generation by the advancing-front method, *Int. J. Numer. Methods Fluids*, 8:1135-1149

[148] Yerry MA and Shephard MS (1984) Automatic 3Dimensional mesh generation by the modified-octree technique *International J for numerical methods in engineering* 20(11): 1965-1990.

[149] Baker TJ, (1989) Developments and trends in three-dimensional mesh generation, *Appl. Numer. Methods*, 5:275-309

[150] George PL, (1991) Automatic Mesh Generation, *Wiley, New York*

[151] Thacker WC, (1980) A brief review of techniques for generating irregular computational grids, *Int. J. Numer. Method Eng.*, 15:1335-1341

[152] Smith CD (1985) *Numerical solution of partial differential equations: finite difference methods*, 3rd edn, Oxford University Press, Oxford

[153] Reddy JN (1984) *An introduction to the finite element method*, McGraw-Hill, New York

[154] Patankar SV (1980) *Numerical heat transfer and fluid flow*, Hemisphere (McGraw-Hill), New York

[155] Gosman AD (1997) Developments in industrial computational fluid dynamics *Proc. of 5th UK National Heat Transfer Conference, London, Sept 17-18, 1997*

[156] CFDS - CFX4 User manual. AEA Industrial Technology, Harwell Laboratory, UK.

[157] Darmofal DL and Haimes R, 1992, AIAA pap92-0074, Reno NY, Jan. 1992

[158] Darmofal DL and Haimes R (1996) An Analysis of 3D particle path integration algorithms *J of computational physics* 123(1): 182-195

[159] Kenweight DN and Lane DA (1996) Interactive time-dependent particle tracing using tetrahedral decomposition *IEEE Transactions on visualization and computer graphics* 2(2):120-129.

[160] Vantyen R, Saloner D, Jou LD and Berger S (1994) MR imaging of flow through tortuous vessels - A numerical simulation *Magnetic resonance in medicine.* 31(2):184-195

[161] Jou LD, Vantyen R Berger A and Saloner D (1996) Calculation of the magnetization distribution for fluid-flow in curved vessels *Magnetic resonance in medicine.* 35(4):577-584

[162] Siegel JM, Oshinski JN, Pettigrew RI and Ku DN (1995) Comparison of phantom and computer-simulated MR-images of flow in a convergent geometry - implications for improved 2-dimensional MR-angiography *JMRI - J. of Magnetic resonance imaging,* 5 6):677-683

163] Siegel JM, Oshinski JN, Pettigrew RI and Ku DN (1997) Computational simulation of turbulent signal loss in 2D time-of-flight magnetic resonance angiograms *Magnetic resonance in medicine.* 37(4):609-614.

[164] Ciofalo M, Collins MW and Stasiek J (1996) Investigation of flow and heat transfer in corrugated passages. Two: Numerical simulation *Int. J. Ht Mass Tran., 39(1):165-192, 1996*

[165] Steinman DA, Frayne R, Zhang XD, Rutt BK and Ethier CR (1996) MR measurement and numerical-simulation of steady flow in an end-to-side anastomosis model. *J. of Biomechanics.* 29(4):537-542

[166] Steinman DA, Ethier CR and Rutt BK (1997) Combined analysis of spatial and velocity displacement artifacts in phase contrast measurements of complex flows *JMRI - J. of Magnetic resonance imaging,* 7(2):339-346

[167] Steinman DA and Rutt BK (1998) On the nature and reduction of plaque-mimicking flow artifacts in black blood MRI of the carotid bifurcation. *Magnetic resonance in medicine.* 39:635-641.

[168] Foutrakis GN, Burgreen G, Yonas H and Sclabassi RJ (1996) Construction of 3D arterial volume meshes from magnetic-resonance angiography *Neurological research,* 18(4):354-360.

[169] Xu XY, Collins MW and Jones CJH (1992) Flow studies in canine artery bifurcation using a numerical simulation method. *ASME J. Biomech. Eng.* 114(4): 504-511.

[170] Xu XY and Collins MW (1997) A problem-oriented approach to the numerical modelling of haemodynamic problems. *Advances in Engineering Software*, 28:365-377.

[171] Q. Long, XY. Xu and MW. Collins (1996) Generation of structure of the aortic bifurcation from magnetic resonance angiogram *Proc. of 1st Inter. Conference on Simulation Modelling in Bioengineering*, BIOSIM'96, Eds Cerrolaza M, Jugo D and Brebbia CA, pp217-226.

[172] Long Q, Xu XY, Collins MW, Stanton A, Thom SA and Hughes AD (1998) Reproducibility analysis of 3D geometrical reconstruction of a human arterial bifurcation *Proc. Medical Image Understanding and Analysis '98*, Leeds University, pp 21-24.

[173] Long Q, Xu XY, Collins MW, Griffith TM and Bourne M (1997) Generation of CFD velocity boundary condition from cine MR phase-contrast images *Proc. Medical Image Understanding and Analysis '97*, Oxford University, pp 117-120.

[174] Long Q, Xu XY, Collins MW, Griffith TM and Bourne M (1997) Some fluid dynamics aspects of the aortic bifurcation using magnetic resonance imaging and computational fluid dynamics *Internal Medicine Clinical and Laboratory* 5(1):33-39.

[175] Boisspnnat JD (1988) Shape reconstruction from planar cross sections, *Computer Vision, Graphics, and image processing*, 44:1-29.

[176] NAG Fortran Library Mark 16 Volume 3 E02BEF, E02BBF

[177] Kerlick GD and Klopfer GH: Assessing the quality of curvilinear coordinate meshes by decomposing the Jacobian matrix, *Applied mathematics and computation*, (1982), 10:787-807.

[178] Gatlin B, Thompson JF, Yeon YF, Luong P, Ganapathiraju D and Wolverton MK: Extensions to the EAGLE grid code for quality control and efficiency, *AIAA paper 90-0148*, Jan. 1991.

[179] Luong PV, Thompson JF and Gatlin B: Solution-adaptive and quality-enhancing grid generation, *AIAA J. of Aircraft*, 30(2) (1993) 227-234.

[180] Environment User Guide. *AEA technology, Comput. Fluid Dynamics Service.* 1994.

[181] NAG Fortran Library Mark 16 Volume 3 E01SAF

[182] Rhie CM (1981) A numerical study of the flow past an isolated airfoil with separation, *Ph.D. thesis, Dept. of Mech. and Industrial Eng., University of Illinois at Urbana-Champaign.*

[183] Rhie CM and Chow WL (1983) Numerical study of the turbulent flow past an airfoil with trailing edge separation *AIAA Jl, 21* pp1527-1532

[184] CFX4.0 User Guide (1997), *AEA technology, Comput. Fluid Dynamics Service.*

[185] Zhao SZ, Xu XY and Collins MW (1997) A novel numerical method for analysis of fluid and solid coupling. *Numerical Method in Laminar and Turbulent Flows*, Eds: Taylor C and Cross J, Vol 10, Swansea, Pineridge Press, pp525-534

[186] Shah P.M. et al.(1976) Prediction of occlusive disease for the left iliac artery. *J. Card. Surg.* 17: 420-425

[187] Parsonnet V., Alpert J and Brief BD.(1970) Femoro-femoral and axillo-femoral grafts: compromise of preference. *Surgery* 67: 26-32

[188] Inahara T.(1972) Enderterectomy for occlusive disease of the aortoiliac and common femoral arteries. *AM. J. Surg.* 124: 235-241

[189] Moore J.E. et al.(1992) Pulsatile flow visualization in the abdominal aorta under differing physiologic conditions: implications for increased susceptibility to atherosclerosis. *J. of Biomech. Eng. ASME.* 114: 391-397

[190] Pedersen E.M. et al.(1994) Influence of abdominal aortic curvature and resting versus exercise conditions on velocity fields in the normal abdominal aortic bifurcation. *J. Biomech. Eng. ASME.* 116: 347-353

[191] Xu XY, Long Q, Collins MW, Griffith TM and Bourne M (1999) 3D Reconstruction of the flow in human arteries. *Proc. of IMechE, J. of Eng. in Med. (in press)*.

[192] Long Q, Xu XY, Collins MW, Griffith TM and Bourne M (1998) The combination of magnetic resonance angiography and computational fluid dynamics: a critical review. *Critical reviews in biomedical engineering*, 26(4):227-276

[193] Palmen DEM, Vandecosse FN, Janssen JD and Vandongen MEH (1994) Analysis of the flow in stenosed carotid-artery bifurcation models - hydrogen-bubble visualization. *Journal of Biomechanics*, 27(5):581-590

[194] Anayiotos AS, Jones SA, Giddens DP Glagov S and Zarins CK (1994) Shear-stress at a compliant model of the human carotid bifurcation. *J. of Biomech, Engineering-transactions of the ASME*, 116:98-106

[195] Perktold K and Rappitsch G (1995) Computer-simulation of local blood-flow and vessel mechanics in a compliant carotid-artery bifurcation model. *J. of Biomechanics*, 28(7):845-856

[196] Perktold K, Thurner E and Kenner T (1994) Flow and stress characteristics in rigid walled and compliant carotid-artery bifurcation models. *Medical & Biological Engineering & Computing* 32(1):19-26

[197] Lee D and Chiu JJ (1996) Intimal thickening under shear in a carotid bifurcation - a numerical study. *J of Biomechanics* 29(1):1-11

[198] Zhao SZ, Xu XY et al (1998) The influence of the superior thyroid artery on flow within carotid bifurcation. *Internal report. Dept. of Chem. Eng. and Chem. Tech., Imperial College*